Analysis and Modelling of Full-Range Post-Dryout Heat Transfer in Vertical Tubes

Zur Erlangung des akademischen Grades
Doktor der Ingenieurwissenschaften
von der KIT-Fakultät für Maschinenbau des
Karlsruher Instituts für Technologie (KIT)

genehmigte
DISSERTATION
von

M. Sc. Dali Yu

Tag der mündlichen Prüfung: 03. September 2019

Hauptreferent: Prof. Dr.-Ing. Xu Cheng

Korreferent: Prof. Dr.-Ing. Thomas Schulenberg

I declare that I have developed and written the enclosed thesis completely by myself, and have not used sources or means without declaration in the text.

Karlsruhe, 27. May 2019

. . . .

(**Dali Yu**)

Acknowledgements

I would like to express my gratitude to all those who helped me during the period of my Ph.D. study. First, my most appreciation would be conveyed to Professor Xu Cheng for his constant encouragement and guidance. In the past several years, he has spent much time teaching me doing research and providing me with inspiring advice. Without his patient instruction, insightful criticism, and expert vision in this research, the present work and dissertation would not have been possible to be completed.

Second, I would like to thank Professor Thomas Schulenberg. He was so caring about my graduation while I invited him as my second adviser. I was very impressed by the width and depth of his knowledge in the post-dryout heat transfer area. Without his comments and suggestions, I can't improve the dissertation into the current version.

I would also like to thank Dr. Aurelian Florin Badea and Dr. Dae-Hyun Hwang. Both of them have given me a lot of help in my research and during my looking for jobs. Besides, I would like to say thanks to the whole MOPOW team members, including Ludwig Köckert, Denis Klingel, Meiqi Song, and already graduated Dr. Florian Feuerstein and Dr. Martin Sonntag. Without your help and contribution to the project, I would not have the convenience to conduct my theoretical studies. Besides, I would like to thank Fangnian Wang, Moritz Schenk, and Dr. Xi Wang. They have helped me a lot in both life and work. For colleagues those who are not mentioned here, this doesn't mean there is no gratitude to you. In fact, I enjoyed the atmosphere of working in the same institute with you and value the happy memories of drinking beers together.

Moreover, I would like to thank some friends I have made in Karlsruhe, especially, Isabella with her family and Min Bao. Without your help and taking care, my first liveaboard couldn't have been so smooth.

Last but not least, I would like to thank my family, including my parents and my sister, for supporting me spiritually throughout the whole Ph.D. period and my life in general.

Dali Yu
Karlsruhe, 27. May 2019

Abstract

The research of post-dryout heat transfer has generated great interest in both the academic and industrial fields because of its importance in determining the maximum surface temperature, which is one of the key factors for steam generator design, safety analysis of nuclear reactor loss-of-coolant accidents, and performance evaluation of some advanced nuclear fuels. A post-dryout heat transfer region can be encountered once the contact between liquid film and the heated surface cannot be maintained due to the continuous liquid film depletion, and the liquid phase is only in the form of dispersed droplets. In spite of extensive studies in the past decades, reliable prediction methods for post-dryout heat transfer are still missing due to the complexity of processes involved, especially due to the difficulties in the prediction of thermal non-equilibrium. Therefore, a general theoretical model, as well as scaling methods for full-range post-dryout heat transfer in vertical tubes, is developed and assessed in the current work.

The whole post-dryout heat transfer region consists of a developing region and a fully developed region. Both the definition of terms *developing post-dryout region* and *fully developed post-dryout region* and the determination equation for the length of the developing post-dryout region are proposed in the current work to distinguish and quantify these two regions. As for the theoretical modelling, the proposed model considers three-path heat transfer that involves heat transfer from the heated wall to vapor, from vapor to droplets and from direct contact between wall and droplets. All kinds of thermal radiative heat transfer are neglected. Forslund correlation (Forslund and Rohsenow, 1966) is modified for calculating the convective Heat Transfer Coefficient (HTC) between wall and vapor. Kendall model (Kendall and Rohsenow, 1978) is used for calculating the wall-droplets contact heat transfer effectiveness. The cross-section of flow is divided into a *film region* and a *core region*, which makes it possible to account for the impact of droplets' concentration distribution over the cross-section on interfacial heat transfer between vapor and droplets. Interfacial HTC is predicted by Hughmark correlation (Hughmark, 1967) with a combination of a shielding factor.

The proposed theoretical model is assessed under a wide range of flow conditions in multiple types of fluid. Mainly four widely used post-dryout heat transfer models including GRO (Groeneveld and Delorme, 1976), CSO (Chen et al., 1979), LCS (Varone and Rohsenow, 1986), and the post-dryout model in the ATHLET code (Austregesilo et al., 2012) as well as three experiments including two uniform axial heat flux Becker (Becker et al., 1983) and KIT (Köckert et al., 2018) experiments, and one non-uniform axial heat flux experiment BeckerII (Becker et al., 1992), are used to assess the proposed model. Results show that the proposed model generally underestimates Becker experimental HTC by 13.82% with a Root-Mean-Square (RMS) error of 20.05%, overestimates the KIT experimental HTC by 6.86% with an RMS error of 10.32%, and underestimates BeckerII experimental HTC by 6.74% with an RMS error of 17.65%, in the fully developed post-dryout region.

Fluid-to-fluid modelling of post-dryout heat transfer between R-134a and water is studied. The scaling methods are developed based on the dimensional analyses by using Buckingham Pi-theorem. The work starts from deriving dimensionless numbers and then selecting dimensionless numbers by their significance to post-dryout heat transfer. 5 different forms of the scaling methods are obtained and evaluated through an optimization procedure, for which a new interpolation method is developed. The optimized scaling methods are eventually assessed by some experimental tests.

Zusammenfassung

Die Forschung zur Wärmeübertragung nach dem Dryout hat sowohl im akademischen, als auch im industriellen Bereich großes Interesse hervorgerufen, da sie für die Bestimmung der maximalen Oberflächentemperatur von Bedeutung ist, die einer der Schlüsselfaktoren für die Auslegung von Dampferzeugern, die Sicherheitsanalyse von Kühlmittelverlustunfällen in nuklearen Reaktoren und die Leistungsevaluierung einiger fortschrittlicher Kernbrennstoffe ist. Der Bereich der Wärmeübertragung nach dem Dryout (Post-Dryout genannt) liegt vor, wenn der Kontakt zwischen dem Flüssigkeitsfilm und der erhitzten Oberfläche nicht aufrechterhalten werden kann und die flüssige Phase nur in Form dispergierter Tröpfchen vorliegt. Trotz umfangreicher Studien in den letzten Jahrzehnten fehlen zuverlässige Vorhersagemethoden für die Wärmeübertragung nach dem Dryout aufgrund der Komplexität der auftretenden Prozesse, insbesondere aufgrund der Schwierigkeiten bei der Vorhersage des thermischen Ungleichgewichts. Daher werden in der vorliegenden Arbeit ein allgemeines, theoretisches Modell, sowie Skalierungsmethoden für die vollständige Wärmeübertragung nach dem Austrocknen in vertikalen Rohren entwickelt und bewertet.

Der gesamte Bereich der Wärmeübertragung im Post-Dryout besteht aus einem *„Entwicklungsbereich“* und einem *„vollständig entwickelten Bereich“*. Sowohl die Definition dieser Begriffe, als auch die Bestimmungsgleichung für die Länge des Entwicklungsbereichs werden in der vorliegenden Arbeit zur Unterscheidung und Quantifizierung dieser beiden Regionen vorgeschlagen. Für die theoretische Modellierung berücksichtigt das vorgeschlagene Modell drei Möglichkeiten der Wärmeübertragung, i) Wärmeübertragung von der erhitzten Wand zum Dampf, ii) vom Dampf zu den Tröpfchen und iii) Wärmeübertragung durch direkten Kontakt zwischen Wand und Tröpfchen. Alle Arten der Wärmeübertragung durch Wärmestrahlung werden vernachlässigt. Die Forslund-Korrelation (Forslund and Rohsenow, 1966) wird für die Berechnung des konvektiven Wärmeübergangskoeffizienten (HTC) zwischen Wand und Dampf modifiziert, wohingegen zur Berechnung der Wirksamkeit der Wand-Tröpfchen-Wärmeübertragung das Kendall-Modell (Kendall and Rohsenow, 1978) verwendet wird. Der Strömungsquerschnitt wird in einen Film- und einen Kernbereich unterteilt, wodurch die Auswirkung der Konzentrationsverteilung der Tröpfchen über den Querschnitt auf den Wärmeübergang im Bereich der Grenzflächen zwischen Dampf und Tröpfchen berücksichtigt werden kann. Der Grenzflächen-Wärmeübergangskoeffizient wird unter Verwendung der Hughmark-Korrelation (Hughmark, 1967) in Kombination mit einem Abschirmfaktor berechnet. Das vorgeschlagene theoretische Modell wird unter einer Vielzahl von Strömungsbedingungen in mehreren Arten von Flüssigkeiten bewertet.

Im Wesentlichen werden vier weit verbreitete Modelle der Post-Dryout Wärmeübertragung, darunter GRO (Groeneveld and Delorme, 1976), CSO (Chen et al., 1979), LCS (Varone and Rohsenow, 1986) und das Modell im ATHLET-Code (Austregesilo et al., 2012) sowie drei Experimente, darunter zwei Versuchsreihen mit gleichmäßigem axialem Wärmestrom nach Becker (Becker et al., 1983) und KIT (Köckert et al., 2018) sowie ein Experiment mit ungleichmäßigem axialem Wärmestrom nach BeckerII (Becker et al., 1992)

zur Bewertung des Modells verwendet. Die Ergebnisse zeigen, dass das vorgeschlagene Modell den experimentellen Wärmeübergangskoeffizienten in den Becker-Versuchsreihen im Allgemeinen um 13,82% unterschätzt, wobei der Root-Mean-Square-Fehler (RMS) bei 20,05% liegt. Der experimentelle HTC nach KIT wird durch das vorgeschlagene Modell, bei einem RMS-Fehler von 10,32%, durchschnittlich um 6,86% überschätzt, während der experimentelle HTC in den BeckerII-Versuchsreihen durchschnittlich um 6,74% unterschätzt wird. Der RMS-Fehler liegt hierbei bei 17,65%. Die voranstehenden Abweichungen beziehen sich auf den vollständig entwickelten Post-Dryout Bereich.

Die Fluid-zu-Fluid-Modellierung des Post-Dryout Wärmeübergangs zwischen R-134a und Wasser wird in der vorliegenden Arbeit ebenfalls untersucht. Die Skalierungsmethoden werden basierend auf Dimensionsanalysen unter Verwendung des Buckingham-Pi-Theorems entwickelt. Die Skalierungsarbeit beginnt mit der Ableitung dimensionsloser Kennzahlen. Im Anschluss erfolgt eine Auswahl von dimensionslosen Kennzahlen, basierend auf ihrer Bedeutung für die Post-Dryout Wärmeübertragung. Fünf verschiedene Varianten von Skalierungsmethoden können unterschieden und durch einen Optimierungsprozess bewertet werden, wofür eine neue Interpolationsmethode entwickelt und angewendet wird. Die optimierten Skalierungsmethoden werden abschließend anhand experimenteller Versuche überprüft.

Contents

List of Figures

List of Tables

Nomenclature

General

Symbol	*Dimensions*	*Description*
Bo	$[-]$	Boiling number
C	$[-]$	coefficient
C_D	$[-]$	droplet drag coefficient
C_p	$[Jkg^{-1} {}^{\circ}\mathrm{C}^{-1}]$	specific heat capacity at constant pressure
d	$[-]$	differential operator
d	$[m]$	droplet diameter
$\bar{d}$	$[m]$	mean droplet diameter
d^*	$[m]$	most probable droplet diameter in Eq. (3.16)
D_T	$[m]$	tube diameter
e	$[-]$	error
$\exp$	$[-]$	exponential function
f	$[-]$	friction factor
f_F	$[-]$	Fanning friction factor
f_s	$[-]$	mass transfer shielding factor, in Eq. (3.40)
g	$[m\,s^{-2}]$	gravitational acceleration
G	$[kgm^{-2}s^{-1}]$	mass flux
Gz	$[-]$	Graetz number
h	$[Wm^{-2} {}^{\circ}\mathrm{C}^{-1}]$	heat transfer coefficient
i	$[J\,kg^{-1}]$	specific enthalpy
i_{v-d}	$[J\,kg^{-1}]$	latent heat of vaporization
Δi	$[J\,kg^{-1}]$	inlet subcooling ($= i_{d,s} - i_{in}$)
I_1	$[-]$	constant 0.225
I_2	$[-]$	constant 1.5
k	$[Wm^{-1} {}^{\circ}\mathrm{C}^{-1}]$	thermal conductivity
K	$[-]$	coefficient in Eq. (2.14)
K_n	$[-]$	nondimensional parameter in Eq. (2.18)
K_1	$[-]$	weighting factor in Eq. (3.12a)
K_2	$[-]$	weighting factor in Eq. (3.41)
L	$[m]$	length
L_{dev}	$[-]$	length of developing post-dryout region, defined as equilibrium quality difference between the regions transition place and dryout
n	$[-]$	number of points
Nu	$[-]$	Nusselt number
P	$[-]$	probability distribution function
P	$[Pa]$	pressure
Pr	$[-]$	Prandtl number
q''	$[W\,m^{-2}]$	heat flux
$\overline{q''}$	$[W\,m^{-2}]$	average heat flux

Re	$[-]$	Reynolds number
R_{max}	$[m]$	maximum droplet extension radius
R_S	$[-]$	scaling ratio
$\bar{R}$	$[m]$	average droplet extension radius
S	$[-]$	velocity slip ratio
T	$[^{\circ}\mathrm{C}]$	temperature
$\widetilde{T}$	$[-]$	dimensionless temperature difference
U	$[m\,s^{-1}]$	axial velocity
u^*	$[m\,s^{-1}]$	shear velocity
V_d	$[m\,s^{-1}]$	droplets deposition velocity
V^+	$[-]$	dimensionless droplets deposition velocity
We	$[-]$	Weber number
We_c	$[-]$	critical Weber number
We_p	$[-]$	Weber number based on droplet deposition velocity
x	$[-]$	quality
x_A	$[-]$	quality at onset of annular flow
y^+	$[-]$	dimensionless distance from wall
Z	$[m]$	distance from dryout in the axial direction

Greek

ϕ_e	$[-]$	thermal entry length correction factor
ϕ_h	$[-]$	overall two-phase–single-phase Nusselt number ratio
ϕ_p	$[-]$	factor for suppression of heat transfer due to the droplets behaving as particles
ϕ_t	$[-]$	droplet evaporation correction factor
φ	$[-]$	gray-body factor
σ	$[N\,m^{-1}]$	surface tension
σ_B	$[Wm^{-2}K^{-4}]$	Stefan-Boltzmann constant
Γ_v	$[kgm^{-3}s^{-1}]$	mass rate of vapor generation per unit volume
α	$[-]$	void fraction
μ	$[kgm^{-1}s^{-1}]$	dynamic viscosity
ρ	$[kg\,m^{-3}]$	volumetric mass density
ρ_v^*	$[kg\,m^{-3}]$	vapor density in property correlation factor
$\Psi(G)$	$[-]$	dimensionless number involving mass flux
ε	$[-]$	effectiveness in Eq. (3.24)
ε_s	$[-]$	effectiveness of vapor-droplet heat transfer in Eq. (2.25)
β_1	$[-]$	parameter in calculating effectiveness
β_2	$[-]$	parameter in calculating effectiveness
δ	$[m]$	wall-droplet separation distance
δ_c	$[m]$	critical wall-droplet separation distance
$\delta_{c,lf}$	$[m]$	critical value for liquid film thickness
π	$[-]$	constant 3.1415...

Subscripts & Superscripts

Symbol	*Description*
$-$	between
0	base
a	actual
c	critical
d	droplet
dev	developing post-dryout region
do	dryout
e	equilibrium
$fdev$	fully developed post-dryout region
hom	homogeneous
in	inlet
i, j	index of data point
lf	liquid film
m, n	constant exponent
NB	nucleate boiling
oc	optimal correlation
poi	point of interest
r	radiation
rt	transition place of developing and fully developed post-dryout regions
s	saturation
T	tube
TP	two-phase mixture
v	vapor
va	actual vapor
vb	vapor at the bulk temperature
vc	vapor in the core region
ve	equilibrium vapor
vf	vapor in the film region
vs	vapor at the saturation temperature
vw	vapor at the wall temperature
w	wall
y	transverse direction

Abbreviations

Abbreviation	*Full Form*
ATHLET	Analysis of THermal-hydraulics of LEaks and Transients
BWR	Boiling Water Reactor
CFD	Computational Fluid Dynamics
CHF	Critical Heat Flux
CSO	CSO model (Chen et al., 1979)
DFFB	Dispersed Flow Film Boiling
GRO	Groeneveld model (Groeneveld and Delorme, 1976)
HTC	Heat Transfer Coefficient
KIMOF	KIT Model Fluid Facility
KIT	Karlsruhe Institute of Technology
KTH	Royal Institute of Technology
LCS	Local Conditions Solution (Varone and Rohsenow, 1986)
PDF	Probability Distribution Function
PWR	Pressurized Water Reactor
RMS	Root-Mean-Square

1. Introduction

1.1. Post-dryout heat transfer

A post-dryout heat transfer region can be encountered once the contact between liquid film and the heated surface cannot be maintained due to the continuous liquid film depletion, and the liquid phase is only in the form of dispersed droplets. In some occasions, the term post-dryout is used to denote the general heat transfer deterioration in flow boiling process, where liquid could be in the form of a dispersed spray of droplets, continuous liquid core, or transition between the former two cases (Groeneveld, 1973). Herein, refers to the term *post-dryout* as the heat transfer deterioration in the condition while the liquid is only in the form of dispersed droplets, usually encountered at a void fraction more than 80%. Conventionally, the post-dryout region is divided into a developing region (unstable film boiling) and a fully developed region (stable film boiling) as shown in Figure 1.1. The developing region is defined as an unstable region with occurring wet contact heat transfer between wall and droplets. Heat transfer coefficient in this region reduces significantly, with an accompanying steep temperature rise on the wall surface. While wet contact is not apparent, the near-wall vapor temperature rises sharply. As a result, droplets near the wall are quickly evaporated, and the direct wall-droplets contact becomes less frequent. In this region, vapor temperature and velocity structures and droplets distribution over the cross-section of the tube are well rearranged, finally develop into a relatively stable state, which is called fully developed post-dryout region, characterized by a stable mist flow pattern and no wall-droplets wet contact.

Heat transfer in post-dryout regime involves various heat exchange paths among the vapor phase, droplets, and the heated wall, which is illustrated as below:

- convective heat transfer from the wall to the vapor
- interfacial heat transfer from vapor to the droplets
- contact heat transfer between wall and droplets
- radiative heat transfer from wall to droplets
- radiative heat transfer from vapor to droplets
- radiative heat transfer from wall to vapor

Due to the fact that heat is not transferred instantaneously from the heated wall to the liquid droplets, instead, most of the heat is first transferred to the near-wall vapor, and then

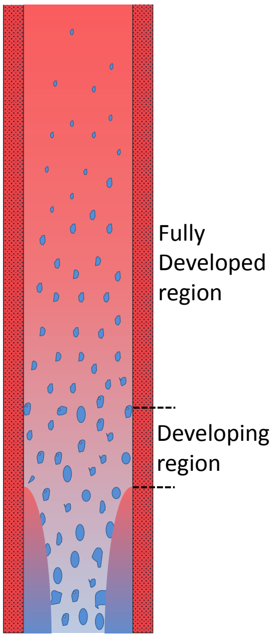

Figure 1.1.: Typical flow patterns in the post-dryout region.

partially transferred from the vapor to the liquid droplets, the droplets and vapor usually have the different temperatures, this difference is called the thermal non-equilibrium. A very significant thermal non-equilibrium of several hundred degrees can be generated in the post-dryout region, confirmed by some experiments with water at low to moderate pressures in a tube (Nijhawan et al., 1980; Evans et al., 1983; Gottula et al., 1985).

Generally, the primary mode of heat transfer at the wall is forced convection of the vapor phase, especially in the fully developed post-dryout region, liquid droplets do not wet the heated wall surface, heat transfer through wall-droplets contact is relatively small. As a result, the wall-droplets heat transfer accounts only for a little percentage of the total heat input in the fully developed region. The superheated vapor primarily evaporates the droplets, and the actual vapor quality is always less than the thermal equilibrium quality. In the developing region, there are indications that direct wall-droplets contact heat transfer might be significant at short distances downstream of the dryout location, which were shown by experiments (Unal et al., 1988; Cokmez-Tuzla et al., 1993).

Heat transfer prediction in post-dryout region is challenging mainly due to the impact of the concentration and spectrum of droplets on two aspects: one is the alteration on the convective heat transfer coefficient by the modification of vapor temperature profile and the modifications of vapor velocity and thermal boundary layers. Another is the alteration on the interfacial heat transfer by the modification of vapor superheat and interfacial area. The concentration and spectrum of droplets are strongly dependent on their previous life and their generation mechanisms, thus heat transfer in post-dryout region better to be regarded as history-dependent. As for the contribution due to all kinds of thermal radiation, this part of heat transfer is often considered negligible (Chen, 1983; Hicken, 1985) since the wall temperature usually is not so high in the post-dryout conditions, compared to the conditions that critical heat flux (CHF) occurs at low vapor quality.

Since the presence of droplets is crucial to the post-dryout heat transfer, many experimental and theoretical studies on the characteristic droplet diameter and droplets size distribution in post-dryout flow have been carried out. However, the dryout droplets diameter calculation for post-dryout flow is complicated, because droplets are formed at all places before dryout, whihc results in difficulties for calculating the average droplet diameter at dryout. Figure 1.2 illustrates the formation of droplets size in post-dryout flow, a process which begins immediately upon the formation of annular flow. Varone (1990) summarized four processes that affect the average droplet diameter at dryout, including: (a) large chunks of liquid throw by boiling in the liquid film, (b) droplets erupted from the film into the vapor core by roll waves, named Helmholtz instabilities, (c) break-up effect after droplets being entrained in the vapor core, and (d) droplets deposition onto the liquid film. For the break-up effects, two types of break-up processes were observed, including capillary break-up and aerodynamic break-up. The aerodynamic break-up mechanism was by far considered as the most essential fragmentation process, and many models assume that aerodynamic break-up mechanism based on a Weber number determines the initial value of the characteristic droplet diameter.

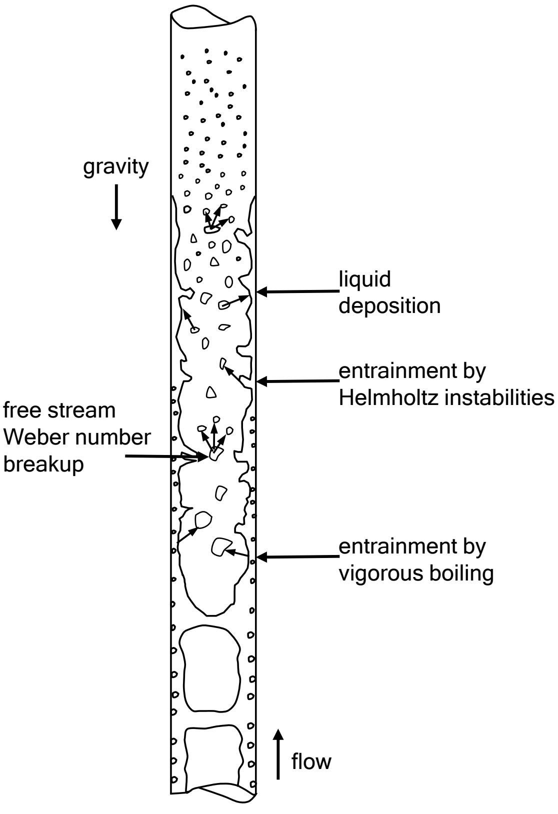

Figure 1.2.: Droplets formation in post-dryout flow [source: (Varone, 1990)].

1.2. Research background

Experimental studies on post-dryout heat transfer and its predicting method development have been conducted for over sixty years, range from wall temperature data in various fluids and various flow conditions to subtopics such as droplets hydrodynamics' influences on both the convective heat transfer between wall and vapor and the interfacial heat transfer between vapor and droplets.

Research in the area of Dispersed Flow Film Boiling (DFFB) began in the 1960s. The leading research group was the Heat and Mass Transfer Laboratory at the Massachusetts Institute of Technology under the direction of Peter Griffith and Warren Rohsenow. Early experimental investigations (Laverty and Rohsenow, 1964; Bennett et al., 1968) measured wall temperatures, mass flow, system pressure, inlet equilibrium quality, and wall heat flux, but without measurement of superheated vapor temperature or actual quality. In concert with such early experimental investigations, initial modelling works were conducted by the representatives, Dougall (1963) and Groeneveld and Moeck (1969). Those works assume the vapor is in an equilibrium state, namely, the vapor is considered having no superheat. According to the public records, Forslund and Rohsenow (1966) is probably the first measured and confirmed the non-equilibrium effect in a nitrogen-based experiment. A helium gas tracer technique was used and found that the thermal non-equilibrium is a strong function of the total mass flux. Generally, the non-equilibrium decreases with increasing mass flux, and this tendency was confirmed by other researchers, e.g. Groeneveld and Delorme (1976).

With more findings confirmed the existence of thermal non-equilibrium in the post-dryout regime (Mueller, 1967; Nijhawan et al., 1980; Gottula et al., 1983), a vast number of theoretical models were developed to include the non-equilibrium effect. Some of the works directly correlate the relationship between the actual and equilibrium qualities, examples of models that have included such a relationship are Groeneveld model (GRO) (Groeneveld and Delorme, 1976), and CSO model that developed by Chen et al. (1979). Usually, these correlations are derived from a limited amount of data without revealing the mechanisms inside and are not appropriate for the use outside their databank. Meanwhile, most of the analytical works attempt to predict the wall temperature by considering three-path heat transfer that involves heat transfer from heated wall to vapor, from vapor to droplets and from wall to droplets including direct contact and thermal radiation. Such models adopt assumptions concerning the local values of certain variables, typically are the velocity slip ratio and droplet diameter. Some of the models require the quality at the dryout point; a variable depends on its flow regime upstream and has significant influence on the model's accuracy. In general, many early-stage investigations (Saha, 1980; Yoder, 1980; Moose and Ganić, 1982; Hill and Rohsenow, 1982; Varone and Rohsenow, 1986; Jeong and No, 1996; Guo and Mishima, 2002) are based on one-dimensional separated flow model and differs only by the selection of empirical correlations for heat transfer, or by the selection of models for calculating droplet size. Among these models, one named "Local Conditions Solution (LCS)" (Yoder and Rohsenow, 1983; Varone and Rohsenow, 1986) is found to have good predictions of the wall temperature magnitude in water conditions, but have poor predictions of the wall temperature profile in both water and R-134a conditions.

Recently, some works attempt to simulate the basic mass, momentum, and energy exchange mechanisms in the post-dryout region. These kinds of mechanistic models have improved the description of the thermal-hydraulic phenomena, and have accounted for both the droplets distribution and the concentration (Andreani and Yadigaroglu, 1997; Keizo et al., 2006; Torfeh and Kouhikamali, 2015; Li and Anglart, 2015, 2016; Shi et al., 2016). Some interesting features of the post-dryout heat and mass transfer (e.g. vapor temperature and velocity profile variation caused by droplets' trajectories and evaporations) could be revealed through the computational fluid dynamics (CFD) approach. However, CFD is computationally expensive and the models applied in CFD still need quite extensive knowledge of the physical phenomena to improve the prediction. For example, the lift force model for droplets dispersion flow is still not well established, and different results could be obtained with different models (McLaughlin, 1993; Sugioka and Komori, 2007). In the current system codes for nuclear engineering industry, such as ATHLET (Austregesilo et al., 2012), still adopts three alternative equilibrium correlations for post-dryout heat transfer, named modified Dougall-Rohsenow (Liesch et al., 1975), Groeneveld (Groeneveld and Moeck, 1969), and Condie-Bengston IV (Vojtek, 1978), respectively. Apparently, it is neither reliable nor suitable to include the models by using CFD approach in the current system codes.

Besides the theoretical modelling for post-dryout heat transfer, a totally empirical approach through creating "look-up" table is proposed by Leung et al. (1996, 1997) and referred to as PDO-LW-96. The table was based on $14,687$ data, and it predicted the surface temperature with an average error of 1.2% and an RMS error of 6.73%. Groeneveld et al. (2003) significantly improved the table by expanding the database and replacing the wall heat flux to surface temperature as an independent parameter. In total, about $20,785$ data points in 36 data sets were used in the error assessment, and for nearly all the data sets, the temperature-based film boiling look-up table predicts better than the previous heat flux controlled look-up table.

In the experiment side, Bennett et al. (1968) performed steady-state post-dryout and rewetting experiments in different uniformly heated tubes with water. They found that the wall temperature distribution along the flow direction in the post-dryout region highly depends on flow mass flux. The wall temperatures are increasing at low mass fluxes, increasing moderately or keeping constant at intermediate mass fluxes, and decreasing at high mass fluxes after reaching a maximum local value. While the heat flux is increasing, the local maximum wall temperature is rising, and the onset of dryout is shifting towards upstream. Another comprehensive experimental study of the post-dryout heat transfer in water should be mentioned herein is conducted by Becker et al. (1983) with uniformly heated round tubes in three different inner diameters and under a broad range of flow conditions. The experimental data show similar influences of flow parameters on the wall temperature distribution with that found by Bennett (Bennett et al., 1968). Besides round tube type experiments, most experiments were performed for bundle geometries, Full Length Emergency Core Heat Transfer-System Effects and Separate Effects Tests (FLECHT-SEASET) (Loftus et al., 1981) is one of these bundle type tests and were performed by Westinghouse for a typical Pressurized Water Reactor (PWR) 17 × 17 bundle. Recently, some researchers also attempted to investigate post-dryout heat transfer in annular channels experimentally (Tian et al., 2006) with consideration of the effects due to flow obstacles (Anghel et al., 2012).

Experimental research on post-dryout heat transfer is often performed with other coolants instead of water since similar phenomena can be observed at lower temperatures, pressures, and heat inputs. Nishikawa et al. (1983) conducted post-dryout heat transfer experiments with the refrigerant R-22 in a uniformly heated tube at high subcritical pressures. Forslund and Rohsenow (1966) conducted an experiment in a vertical, uniformly heated tube with nitrogen as the working fluid. Unique to their experimental setup is an attempt to measure the vapor superheat using a helium gas tracer technique to quantify the thermal non-equilibrium present in post-dryout flow. Lee and Chang (2008) conducted post-dryout heat transfer experiments in both smooth and rifled tubes with R-134a. Their results pointed out that for higher mass fluxes, the wall temperature in the post-dryout region reaches a local maximum and decreases with increasing vapor quality. What's more, for lower mass fluxes, the local maximum wall temperature decreases with increasing pressure. The author claimed that the rifled tubes could significantly lower the strong thermal non-equilibrium occurred in the post-dryout region. Köckert et al. (2018) also conducted an R-134a based post-dryout heat transfer experiment in a tube of 10 mm in diameter and 3.1 m in length with a broad range of flow conditions. Around 2000 data points were obtained in the post-dryout region, which are intensively used in the comparisons and analysis of current work. Regarding the influences of flow parameters (e.g. Pressure, Mass Flux, and Heat Flux) on the wall temperature distribution, which are found by the authors to be similar with the tendencies found in experiments by Bennett et al. (1968) and Becker et al. (1983).

In order to reduce the cost and technical difficulties of the water based post-dryout experiments, Freon family fluids have been frequently used as the model fluid because of their lower latent heat of vaporization and lower critical pressure, while compared to water. Fluid-to-fluid modelling is an economical solution to simulate the post-dryout phenomenon under water conditions. Among the fluid-to-fluid modelling methods for dryout, that of Ahmad (1973) is most widely accepted. The method is based on the dimensional analyses by using Buckingham Pi-theorem (Buckingham, 1914) with a compensated distortion technique to obtain the appropriate modelling parameter. This method is extended in the fluid-to-fluid modelling for post-dryout heat transfer. Unfortunately, research in this field is quite a few. Hammouda et al. (1996) has studied post-dryout heat transfer in three different Freons, and Groeneveld et al. (1997) summed up a group of dimensionless numbers from these results for scaling. Nemitallah and Meamer (2013) concluded that the fluid-to-fluid modelling using the scaling of the energy equation is applicable at any operating conditions. Meamer (2011) proposed a fluid-to-fluid model aims to scale the heat transfer coefficient in high-to-moderate pressure and mass flux conditions. However, the scaling method did not fully utilize dimensionless numbers.

1.3. Objectives of research

Motivated by its significance in practical applications, especially in the nuclear engineering field, post-dryout heat transfer is an important process which determines the maximum temperature of the fuel cladding during the loss of coolant accident (LOCA) in Pressurized Water Reactor (PWR) or Boiling Water Reactor (BWR). Despite extensive studies in the past decades, reliable prediction methods are still missing due to the complexity of the processes involved. The goal of this research was to analyze the physical mechanisms of post-dryout heat transfer and to develop a theoretical model to improve the prediction, as well as to propose a scaling method for fluid-to-fluid modelling between R-134a and water. An outline of the original works can be expressed as follows,

- *Determination of the flow regions:* Definitions of the terms developing post-dryout region and fully developed post-dryout region were proposed. Furthermore, a correlation was developed to predict the length of the developing region, which was regarded as a transient, entrance-region problem with axial distance from the dryout place. The correlation was verified by experiments with conditions of both uniform and non-uniform axial heat fluxes.

- *Modelling of post-dryout heat transfer:* Based on a modification of existing correlation, heat transfer coefficient for convection between wall and vapor was predicted in multiple fluids and a wide range of flow conditions. What's more, the cross-section of flow was divided into a film region and a core region to account for the impact of droplets' volumetric concentration on the interfacial heat transfer between vapor and droplets.

- *Assessment of the theoretical model:* The developed model was assessed mainly by comparing with four widely used post-dryout heat transfer models including GRO, CSO, LCS, and the post-dryout model in ATHLET code, and three experiments including two uniform axial heat flux Becker and KIT experiments, and one non-uniform axial heat flux BeckerII experiment. The role of direct contact heat transfer in post-dryout flow was analyzed under different flow conditions as well.

- *Fluid-to-fluid modelling of post-dryout heat transfer:* A group of dimensionless numbers were derived from the independent variables and selected by their significance to post-dryout heat transfer. Then 5 different forms of the scaling methods were obtained and evaluated through an optimization procedure, for which a new interpolation method was developed. The optimized scaling methods were eventually assessed by some experimental tests.

2. Previous theoretical models

Numerous types of models and correlations for post-dryout heat transfer have been developed and achieved a varying degree of success. Works in this topic can be classified as correlative works and analytical works. Most of the correlative works usually originate with a single-phase wall-vapor convective heat transfer correlation. The coefficients in the correlation are modified to include the impact of the presence of dispersed droplets on the convection. Most of the analytical works on the other hand attempt to predict the wall temperature by considering three-path heat transfer that involves heat transfer from the heated wall to vapor, from vapor to droplets and from wall to droplets including direct contact and thermal radiation. In general, many early-stage investigations are based on a one-dimensional separated flow model and differ only by the selection of empirical correlations for convective and interfacial heat transfer or by the selection of models for calculating the droplet size. Moreover, some interesting features of post-dryout heat and mass transfer (e.g. vapor temperature and velocity profile variation caused by droplets' trajectories and evaporation) could be revealed through the CFD approach. However, this kind of approach is computationally expensive, and the models applied in CFD still need quite extensive knowledge of the physical phenomena to improve the prediction.

Some empirical equilibrium correlations can predict the wall temperature well under some particular conditions, e.g. condition of high pressure, high mass flux, and high quality flow. In such conditions, the thermal non-equilibrium degree is quite low, and the impacts of liquid droplets on post-dryout heat transfer is small. However, the existence of thermal non-equilibrium in the post-dryout regime is experimentally confirmed. Those equilibrium correlations have very limited predicting range, thus, a comprehensive review of non-equilibrium correlations and models for post-dryout heat transfer in the past is shown in Appendix A, and those models are listed in the order of publication year.

In general, correlations and models in the past can be classified as equilibrium correlations and non-equilibrium models. Such equilibrium correlations usually are empirically derived from experimental data with considering equilibrium state of vapor. In contrast, non-equilibrium models tend to estimate the actual vapor superheat in the post-dryout region. Among these non-equilibrium models, some of them use a bunch of empirical correlations to predict the interested variables while the others phenomenologically model the flow and heat transfer processes that involved in the flow regime, including simple one-dimensional models and complex multidimensional ones.

2.1. Equilibrium correlations

ATHLET code (Austregesilo et al., 2012) is one of the most frequently applied system codes for nuclear engineering industry. However, ATHLET still adopts three alternative thermal equilibrium correlations for post-dryout heat transfer, including the modified Dougall-Rohsenow (Liesch et al., 1975), Groeneveld (Groeneveld and Moeck, 1969), and Condie-Bengston IV (Vojtek, 1978). Details of the correlations are summarized as below,

Modified Dougall-Rohsenow correlation

$$h_{w-v} = 0.023 \frac{k_v}{D_T} \left(\frac{G D_T}{\mu_v} \right)^{0.8} Pr_v^{0.4} \left(\frac{T_v}{T_w} \right)^{0.5} \tag{2.1}$$

Groeneveld correlation

$$h_{w-v} = 0.00327 \frac{k_v}{D_T} \left(\frac{G D_T}{\mu_v} \right)^{0.901} \left(Pr_{vw} \right)^{1.32} Y^{-1.5} \tag{2.2}$$

$$Y = 1 - 0.1 \left(\frac{\rho_d}{\rho_v} - 1 \right)^{0.4} (1 - x_e)^{0.4} \tag{2.3}$$

Condie-Bengston IV correlation

$$h_{w-v} = 0.05345 \frac{k_v^{a1} (Pr_{vw})^{a2} \left(\frac{G D_T}{\mu_v} \right)^{a3}}{D_T^{a4} (x_e + 1)^{a5}} \tag{2.4}$$

With $a1 = 0.4593$, $a2 = 2.2598$, $a3 = 0.6249 + 0.2043 \ln (x_e + 1)$, $a4 = 0.8095$, and $a5 = 2.0514$. The vapor properties in all above equations are evaluated at the bulk vapor temperature, and Pr_{vw} is the Prandtl number with properties of vapor evaluated at the wall temperature. Temperatures T_v and T_w are in the unit of K. h_{w-v} is the heat transfer coefficient between wall and vapor. G is the inlet mass flux, D_T is the tube inner diameter, k_v, μ_v and ρ_v are the vapor thermal conductivity, vapor dynamic viscosity, and vapor density, respectively. ρ_d is the droplet density, and x_e is the equilibrium vapor quality.

The modified Dougall-Rohsenow correlation is chosen to represent the ATHLET code in the assessments of the proposed model. All three correlations are found in current work to give similar and manifest overestimations in the prediction of heat transfer coefficients.

2.2. Non-equilibrium models

2.2.1. Empirical models

Groeneveld and Delorme (1976) (GRO)

Groeneveld and Delorme (1976) focused on calculating the non-equilibrium in vapor. A methodology was developed to determine the actual flowing quality and the vapor temperature from experimental post-dryout data. Main assumptions were made as following,

1) the liquid phase does not directly participate in the cooling of the heated surface,

2) radiative heat transfer to the droplets is negligible,

3) and flow is homogeneous with zero slip.

The actual quality x_a is calculated by correlations as below,

$$\frac{i_{va} - i_{ve}}{i_{v-d}} = \exp[-\tan\Psi]\exp[-(3\alpha_{hom})^{-4}] \tag{2.5}$$

where, i_{va} is the specific enthalpy of actual vapor, i_{ve} is the specific enthalpy of equilibrium vapor, i_{v-d} is the latent heat of vaporization, α_{hom} is the homogeneous void fraction, and Ψ is bounded in a range of [0, $\pi/2$],

$$\begin{aligned}\Psi = 0.13864Pr^{0.2031}(Re_{hom})^{0.20006}&\left(\frac{q_w^{''}D_T C_{p,ve}}{k_{ve}i_{v-d}}\right)^{-0.09232}\\ &\bullet(1.3072 - 1.0833x_e + 0.8455x_e^2)\end{aligned} \tag{2.6}$$

$$Re_{hom} = \frac{GD_T x_a}{\mu_{ve}\alpha_{hom}};\ \ \alpha_{hom} = \frac{x_a}{x_a + \frac{\rho_v}{\rho_d}(1 - x_a)} \tag{2.7}$$

where, μ_{ve}, k_{ve} and $C_{p,ve}$ are the thermal equilibrium state vapor viscosity, thermal conductivity, and specific heat capacity at constant pressure, respectively. $q_w^{''}$ is the wall heat flux, α_{hom} is the homogeneous void fraction, Pr is Prandtl number, and x_a is the actual vapor quality.

This non-equilibrium correlation estimates in conjunction with Hadaller's superheated steam correlation (Hadaller and Banerjee, 1969), which is modified with zero slip assumption for two-phase flow convective heat transfer coefficient h_{w-v}, as shown below,

$$h_{w-v} = 0.008348\frac{k_{vf}}{D_T}\left(\frac{Gx_a D_T}{\mu_{vf}\alpha_{hom}}\right)^{0.8774}(Pr_{vf})^{0.6112} \tag{2.8}$$

where, k_{vf} is the thermal conductivity of vapor film, μ_{vf} is the dynamic viscosity of vapor film, and Pr_{vf} is the vapor Prandtl number with properties evaluated at film vapor temperature. Comparing their correlation with additional data, the authors found that the overall root mean square error is 6.9%. Their empirical correlation is only valid in the fully developed post-dryout region. This model should not be applied to the situations where droplet contact could be significant since no heat transfer between the heated surface and the droplets is considered.

Chen et al. (1979) (CSO)

The model developed by Chen et al. (1979), which is known as the CSO model, considers that the thermal non-equilibrium x_a/x_e depends mostly on the imbalance between the heat input to the vapor from the wall, and the interfacial heat transfer. The authors expressed thermal non-equilibrium as a function of three non-dimensional parameters as follows,

$$\frac{T_v - T_s}{T_w - T_v} = \text{dimensionless temperature difference parameter} \tag{2.9a}$$

$$\frac{1 + 0.276Re_d^{0.5}Pr_v^{0.3}}{f_F Re_v Pr_v^{0.33}} = \text{dimensionless heat-transfer coefficient parameter} \tag{2.9b}$$

$$\frac{6(1-\alpha)D_T^2}{d^2} = \text{dimensionless area parameter} \tag{2.9c}$$

where, T_v, T_s and T_w are the temperatures of vapor, saturation state, and the wall surface, respectively. d is the droplet diameter, and f_F is the Fanning friction factor that calculated from the explicit approximation of Beattie's implicit formula:

$$f_F = 0.037(Re)^{-0.17}\ \text{with}\ Re = \frac{GD_T}{\mu_v}\left(x_a + (1 - x_a)\frac{\rho_v}{\rho_d}\right) \tag{2.10}$$

Experimental investigations conducted by the authors indicated that the only one important parameter was the dimensionless temperature difference $\widetilde{T}$. A linear dependence of the thermal non-equilibrium on the dimensionless temperature difference $\widetilde{T}$ could be established for each pressure. Gives,

$$\frac{x_a}{x_e} = 1 - \mathrm{F}(P)\widetilde{T} \tag{2.11}$$

where, P is the system pressure and the function $\mathrm{F}(P)$ was obtained by regression analysis, expressed as follows,

$$\mathrm{F}(P) = \frac{0.26}{1.15 - (P/P_c)^{0.65}} \text{ with } P < 19.51\,MPa \tag{2.12}$$

Herein, P_c is the critical pressure. The model is completed by a convective heat transfer correlation, which is based on the Colburn modification of Reynolds analogy,

$$h_{w-v} = Gx_aC_{p,vf}Pr_{vf}^{-2/3}\frac{f_F}{2} \tag{2.13}$$

The properties are evaluated at the film vapor temperature, which is the average of the wall temperature and the bulk vapor temperature.

Many research has assessed the model. Annunziato et al. (1983) compared the model with experimental vapor and wall temperature data under very low mass flux conditions. He found that the standard deviation of wall temperature was around 33%. Both the calculated heat fluxes using the heat transfer coefficient from Eq. (2.13) and the vapor temperatures were below than the data obtained by Gottula et al. (1985) in a wide range of pressures, under low mass flux conditions.

Varone and Rohsenow (1986) (LCS)

The Local Condition Solution (LCS) is first comprehensively introduced by Yoder and Rohsenow (1983) and has been later improved by Varone and Rohsenow (1986). LCS is originally a step-wise computer solution which predicts wall temperature of the tube as a function of axial position beyond dryout. It is a physical model based on the continuity, momentum, and energy equations, and it uses empirical correlations where is necessary. The main assumptions of this model are:

1) thermal radiations in all form are neglected,
2) no droplets break-up occurs in the whole region,
3) droplets size radial distribution can be characterized by one average droplet size,
4) and thermal equilibrium exists at dryout, and the liquid temperature remains at the saturation temperature always.

With ignoring the variation of fluid properties and using the observation that the product of the slip ratio and the void fraction is roughly equal to 1.0 for the conditions investigated, a first-order differential relation is theoretically derived as below,

$$K\frac{x_a^{3/4}x_e}{(1-x_a)^{7/12}}\frac{\mathrm{d}x_a}{\mathrm{d}x_e} = x_e - x_a \tag{2.14}$$

where, K, a non-equilibrium constant, contains a group of fluid parameters that controls departure from equilibrium. If no break-up occurs, K might be calculated by using only dryout conditions, and it can be simplified as below,

$$K = 0.58 \left(\frac{d_{do}}{D_T}\right)^{1.25} \frac{1}{(1-x_{do})^{5/12}} \left(\frac{\rho_d}{\rho_v}\frac{q''_w}{Gi_{v-d}}\right)^{0.75} \left(\frac{GD_T}{\mu_v}\right)^{0.5} \left(\frac{C_{p,v}\mu_v}{k_v}\right)^{2/3} \cdot \left[\frac{\rho_v}{\rho_d}\frac{1-x_{do}}{x_{do}} + \frac{1}{1+3.65\sqrt{\frac{\rho_d}{\rho_v}\frac{q''_w}{Gi_{v-d}}\frac{d_{do}}{D_T}\frac{1}{x_{do}}}}\right]^{0.5} \tag{2.15}$$

Herein, d_{do} is the droplet diameter at dryout and x_{do} is the vapor quality at dryout.

Varone found that the application of a single phase vapor convection correlation is a weakness since the impacts of droplets presence on the convective heat transfer are not included. He calculated a multiplier R_{Nu}, which is needed in each case to make the predicted wall temperature equals the experimentally measured wall temperature. The empirical correction factor R_{Nu} is adopted and multiplied with the Hadaller correlation (Hadaller and Banerjee, 1969), then the correlation for convective heat transfer coefficient h_{w-v} between wall and vapor is rewritten as below,

$$h_{w-v} = 0.008348\frac{k_{vf}}{D_T}R_{Nu}\left(\frac{Gx_aD_T}{\mu_{vf}\alpha}\right)^{0.8774}(Pr_{vf})^{0.6112} \tag{2.16}$$

where, the vapor properties are evaluated at the film vapor temperature, which is defined as the average value of the wall temperature and the bulk vapor temperature.

Varone and Rohsenow (1986) investigated the value of R_{Nu} against some dimensionless numbers, including vapor viscosity ratio μ_{vb}/μ_{vw}, actual quality x_a, density ratio ρ_d/ρ_v, diameter ratio d/D_T, and vapor Reynolds number Re_{vb}. Finally, relations between R_{Nu} and the actual quality x_a for each different vapor viscosity ratio are graphically represented and suggested, as shown in Figure 2.1. The authors explain the relations that while the wall temperatures are close to the bulk vapor temperatures, droplets can reach the near-wall region and increase the turbulence near the wall. This results in more fluid mixing and heat transfer increase, which leads to $R_{Nu} > 1$. On the contrary, with the wall temperature increasing, the viscosity of the vapor near the wall is increasing, then μ_{vb}/μ_{vw} decreases. This results in less generation of turbulence near the wall, and reducing the turbulence in the core. Therefore, heat transfer is decreasing and the R_{Nu} is decreasing too.

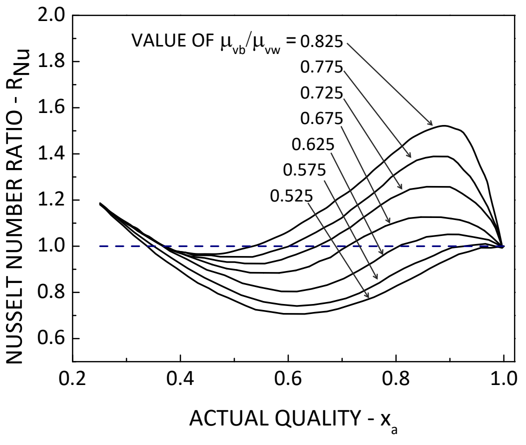

Figure 2.1.: Family of curves of Nusselt number ratio R_{Nu} vs. actual quality x_a for constant viscosity ratios [source: (Varone and Rohsenow, 1986)].

After applying the multiplier R_{Nu} to the single phase heat transfer coefficient to compensate for the effects of the dispersed droplets, the authors found a much better agreement between the model predictions and experimental data. The LCS approach has been assessed against experimental data at moderate pressure for both tubes (Yoder and Rohsenow, 1983) and rod bundles (Kumamaru et al., 1987), and relatively good results have been obtained. However it should be noted that the empirically derived multiplier R_{Nu} did not reveal the mechanisms regarding the influences of the presence of droplets on the convective heat transfer between wall and vapor, it could be invalid outside the range of the utilized data.

Nishikawa et al. (1986)

Nishikawa et al. (1986) conducted studies of post-dryout heat transfer based on experimental data in Freon 22 (R-22) at high sub-critical pressures. Heat transfer by two paths, including convective heat transfer from wall to bulk vapor and interfacial heat transfer from bulk vapor to liquid droplets entrained in the vapor, are considered. All kinds of radiative heat transfer and wall-droplets heat transfer are neglected. The model was developed and verified within the pressure range of $3.4-4.6MPa$ in $13mm$ diameter tube. To predict the convective heat transfer between wall and vapor in R-22, the author developed a correlation as below,

$$h_{w-v} = 0.0048\frac{k_v}{D_T}\left[\frac{GD_T}{\mu_v}\left(x_a + (1-x_a)\frac{\rho_v}{\rho_d}\right)\right]^{0.92} Pr_v^{0.4}\left[1+\frac{2}{(Z/D_T)^{1.1}}\right] \tag{2.17}$$

The actual quality was calculated by an analytic relation from energy balance with empirically derived parameters K_n, as shown below,

$$\frac{\mathrm{d}x_a}{\mathrm{d}x_e} = \frac{1}{BoK_n}\left(\frac{x_e}{x_a}-1\right) \tag{2.18}$$

where, two dimensionless parameters Bo and K_n were found to have a great influence on the relationship of the actual quality and equilibrium quality. Bo is the so-called boiling number, representing the change of the vapor mass fraction per unit tube length at thermodynamic equilibrium. Hence, the higher value of the boiling number means the stronger acceleration of the two-phase flow in the post-dryout region. The dimensionless parameter K_n represents the ratio of the heat capacitance of the vapor flow to the thermal conductance from the vapor to the liquid droplets. Therefore, the parameter K_n is considered as a characteristic parameter, which governs the thermodynamic non-equilibrium degree of the dispersed two-phase flow. As K_n increases, the two-phase fluid departs farther from the thermodynamic equilibrium state. Through theoretical analysis on the relevant dimensionless numbers, the author finally gives the estimation equation of K_n as below,

$$K_n = 4260\left(\frac{GD_T}{\mu_v}\right)^{0.52}\left(\frac{G^2D_T}{\sigma\rho_v}\right)^{-0.73}\left(Pr_v\frac{\rho_v}{\rho_d}\right)^{0.3} x_a^n\,(1-x_a)^{-0.2}\left(\frac{x_e}{x_a}-1\right)^{0.83} \tag{2.19}$$

where, the empirical efficient n can be calculated as below,

$$n = 2.0\exp\left[-1.3\left(\frac{G\mu_v}{\sigma\rho_v}\right)\left(\frac{\rho_d}{\rho_v}-1\right)^{1.7}\right]-1 \tag{2.20}$$

The model by the use of these correlations successfully predicts the wall temperature for post-dryout heat transfer in Freon at high sub-critical pressures. Though the model was developed by data at high sub-critical pressures, it was found by the author that the model also has good predictions at low pressure conditions, while compared with the experiments in Freon 12 (R-12).

Shah and Siddiqui (2000)

Shah and Siddiqui (2000) developed a general model for heat transfer during a dispersed flow film boiling in tubes. Analysis of the possibly non-equilibrium related dimensionless numbers with physical significance was implemented. The author indicated that several experimental studies show that non-equilibrium is affected by heat flux. Thus, the Boiling number shall influence the non-equilibrium. Froude number was also suggested to be considered by the author since experiments showed the behavior of liquid droplet suspensions during film boiling, the gravitational force could have a great influence on the non-equilibrium degree. Then a relation between x_a, x_e, Boiling number Bo, and Froude number Fr was empirically determined. x_a can be graphically plotted as in Figure 2.2 while $Bo \geq 0.0005$. At $Bo = 0$, there considers has no non-equilibrium. Values in the other conditions would be calculated by linear interpolation.

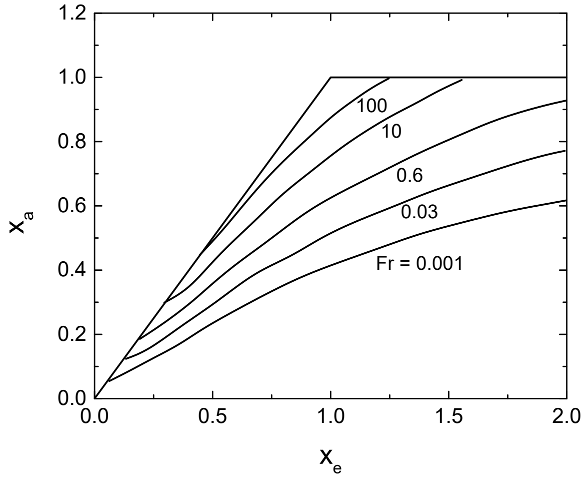

Figure 2.2.: Family of curves of actual quality x_a vs. equilibrium quality x_e for constant Froude number Fr, while $Bo \geq 0.0005$ [source: (Shah and Siddiqui, 2000)].

A single-phase convective heat transfer correlation was used. The author found that for water, film temperature properties gave better agreement, especially at higher pressures. For fluid other than water, bulk temperature properties generally gave better agreement. The author suggested to use the Dittus-Boelter equation for $Re < 10^4$; to use Hadaller and Banerjee (1969) correlation for $Re > 10^4$. All the properties are evaluated at the film vapor temperature for water and the bulk vapor temperature for all other fluids.

2.2.2. One-dimensional phenomenological models

Forslund and Rohsenow (1968)

Forslund and Rohsenow (1968) experimentally investigated dispersed flow film boiling in a vertical and uniformly heated tube with nitrogen as the working fluid. Unique to their experimental setup was an attempt to measure the vapor superheat by using a helium gas tracer technique to quantify the thermal non-equilibrium. Addition to the most frequently considered two steps heat transfer paths, which are from wall to superheated vapor and from vapor to droplets, the authors considered the heat that transferred from the tube wall directly to the liquid droplets as a kind of Leidenfrost effect. For heat transfer from the wall to the vapor, Dittus-Boelter equation was modified and used as below,

$$h_{w-v} = 0.019 \frac{k_v}{D_T} \left(\frac{G x_a D_T}{\mu_v \alpha} \right)^{0.8} (Pr_v)^{0.4} \tag{2.21}$$

To calculate the heat transfer resulting from the proposed Leidenfrost effect, Forslund and Rohsenow used a heat transfer coefficient developed by Baumeister et al. (1965) for a single water droplet on a horizontal plate. The interfacial heat transfer between vapor and droplets is evaluated by a correlation as below,

$$\frac{h_{v-d}d}{k_{vf}} = 2 + 0.55\left[\frac{\rho_{vf}\left(U_v - U_d\right)d}{\mu_{vf}}\right]^{0.5} Pr_{vf}^{1/3} \tag{2.22}$$

where, h_{w-d} is the heat transfer coefficient between vapor and droplets, k_{vf} is the thermal conductivity of vapor film, ρ_{vf} is the density of vapor film, U_v and U_d are the axial velocities of vapor and droplets, respectively, μ_{vf} is the vapor film dynamic viscosity, and Pr_{vf} is the vapor film Prandtl number. Vapor properties are calculated at the film vapor temperature.

The observations of photographs in this experiment suggested that droplet size is primarily a function of the heat flux. Since the acceleration of the vapor is a function of the heat flux and relatively independent of the mass flux, the authors suggested that the rate of vapor acceleration determines droplet sizes. At a higher heat flux or vapor acceleration, the slip velocity is greater, and under these conditions, the droplet size is smaller. Therefore, a critical Weber number We_c at which the droplets break up was proposed as below,

$$We_c = \frac{\rho_v(U_v - U_d)^2 d}{\sigma} \tag{2.23}$$

where, U_v and U_d are the axial velocities of vapor and droplets, respectively. σ is the surface tension.

The authors studied this critical Weber number We_c for the maximum droplet size that ranges between 6.7 and 9.6. Finally, a value of 7.5 was suggested for droplet break-up in the dispersed flow. The massive departure from thermal equilibrium in dispersed flow film boiling has been confirmed in this study, and the thermal non-equilibrium degree was showed to be mainly dependent on the mass flux.

Saha (1980)

Saha (1980) developed a model for post-dryout heat transfer, and mainly focused on the prediction of thermal non-equilibrium degree. The analysis of thermal non-equilibrium resulted in two correlations for the volumetric mass rate of vapor generation. The first correlation is for the calculating of the effectiveness of vapor-to-droplet heat transfer, and the second is for the average droplet size estimation. Saha thinks that for either high wall superheat or high vapor quality, only a few droplets can touch or come near the heated wall. Therefore, in the developed model, the effect of direct wall-to-droplet heat transfer was neglected. The contribution due to the radiative heat transfer has also been found by the author to be negligible within the range of his study. Droplets are evaporated only by the interfacial heat transfer between vapor and droplets.

The author adopted Heineman correlation (Heineman, 1960) for superheated steam to calculate the effective heat transfer coefficient h_{w-v} between the heated wall and the vapor shown as below,

For $6 < \frac{Z}{D_T} < 60$,

$$h_{w-v} = 0.0157\frac{k_{vf}}{D_T}Re_{vf}^{0.84}Pr_{vf}^{0.33}\left(\frac{Z}{D_T}\right)^{-0.04} \tag{2.24a}$$

and $60 \leq \frac{Z}{D_T}$,

$$h_{w-v} = 0.0133 \frac{k_{vf}}{D_T} Re_{vf}^{0.84} Pr_{vf}^{0.33} \tag{2.24b}$$

Herein, Re_{vf} is the vapor Reynolds number with vapor properties evaluated at the film vapor temperature, Z is the distance from dryout along the tube. In addition, the mass rate of vapor generation per unit volume Γ_v is expressed as below,

$$\Gamma_v = \varepsilon_s \frac{k_v (1-\alpha)(T_{vb} - T_s)}{D_T^2 i_{v-d}} \tag{2.25}$$

where, T_{vb} and T_s are bulk vapor and saturation temperatures. ε_s is the effectiveness of vapor-droplet heat transfer and correlated as below,

$$\varepsilon_s = 6300 \left(1 - \frac{P}{P_c}\right)^2 \left[\left(\frac{G x_a}{\alpha}\right)^2 \frac{D_T}{\rho_v \sigma}\right]^{0.5} \tag{2.26}$$

With vapor generation rate calculated by the above equations. Heat balance calculations can be combined to obtain the wall and vapor temperatures, as well as the actual quality.

Moose and Ganić (1982)

Moose and Ganić (1982) developed a non-equilibrium post-dryout heat transfer model based upon the three-path heat transfer that involves heat transfer from wall to vapor, from wall to droplets in contact with the wall, and from vapor to liquid droplets in the vapor core. A procedure was introduced by the author to determine the average droplet diameter, which is based on a size distribution, and the size distribution was suggested by Cumo et al. (1974) as below,

$$\mathrm{P}(d) = \frac{d}{(d^*)^2} \exp\left(\frac{-d}{d^*}\right) \tag{2.27}$$

with normalization into total probability equals to 1,

$$\int_0^\infty \mathrm{P}(d) \mathrm{d}d = 1 \tag{2.28}$$

Herein, P represents the probability distribution function, d^* is the most probable droplet diameter, exp is the exponential function. The maximum droplet size was allowed goes into infinity. For heat transfer between wall and vapor, correlation by McAdams (1954) was used in this model as below,

$$h_{w-v} = \frac{k_{vb}}{D_T} \left(0.023 Re_{vb}^{0.8} Pr_{vb}^{0.33}\right) \left(\frac{\mu_{vb}}{\mu_{vw}}\right)^{0.14} \tag{2.29}$$

where, μ_{vb} and μ_{vw} are the vapor dynamic viscosity, evaluated separately at bulk temperature and wall surface temperature. Moreover, while compared to water, nitrogen, and freon data, the author found the direct wall-to-droplets heat transfer can be neglected, and this effect can be compensated by decreasing the size of the droplets which are evaporating in the free stream.

Varone (1990)

Varone and Rohsenow (1986) developed a mechanistic model of post-dryout heat transfer. It includes the momentum and energy equations for both vapor and droplets, averages the droplet diameter at the dryout location, and uses heat transfer correlations for vapor-to-droplets, wall-to-droplet, and wall-to-vapor. Based on simplifications that Yoder and Rohsenow (1983) had applied, Varone and Rohsenow (1986) well improved the Local Condition Solution (LCS) and makes it is possible that the heat transfer prediction at any position of the tube can be without the step-wise solution. To improve the predictions, it was found necessary to multiply the wall-to-vapor heat transfer coefficient by a factor, which is in the range from around 0.7 to about 2. The factor was found to be a function of the bulk-to-wall viscosity ratio and quality. The factor could also be related to the droplets and vapor densities, the tube and droplets diameters, and Reynolds number. The detailed explanation was indicated by the author that appears to be due to the turbulence suppression and enhancement, which are resulting from the droplet motion.

In the later study, Varone (1990) developed a correlation for convective heat transfer between wall and vapor to account for the effects of the droplet evaporation, the large fluid property variations over the tube cross-section, and the entrance length. Besides the effort in convective heat transfer, the author revealed that the liquid droplets might be larger at the dryout point than that calculated by its original model, which uses a critical Weber number value of 6.5. This model uses a larger critical Weber number of 17.5 to obtain a bigger initial droplet diameter, as well as includes the following gradual droplet break-up effect occurring downstream.

For the wall-vapor convective heat transfer correlation, the author includes the effects such as the thermal entry length, suppression of turbulence due to the physical presence of the droplets, enhancement of heat transfer due to the droplet evaporation, and the effect of various fluid properties. The base Nusselt number without these above effects was calculated by Sozer correlation (Sozer et al., 1984) as below,

$$Nu_{w-v,0} = 0.0168 Re_{vw}^{0.841} Pr_{vw}^{0.4} \tag{2.30}$$

where, the vapor properties are evaluated at wall temperature, and the actual Nusselt number Nu_{w-v} is related to the base Nusselt number $Nu_{w-v,0}$ by the relation below,

$$Nu_{w-v} = \phi_h Nu_{w-v,0} \tag{2.31a}$$

$$\phi_h = \phi_p \phi_t \phi_e \left(\frac{\rho_v^*}{\rho_{vb}} \right)^m \tag{2.31b}$$

where, ρ_v^* is a weighted vapor density, which is used for property correction factor. ρ_{vb} is the bulk vapor density. ϕ_h represents the overall Nusselt number correction factor, ϕ_p is a factor for suppression of heat transfer due to the droplets behaving as particles, ϕ_t is a droplet evaporation correction factor, and ϕ_e is a thermal entry length correction factor. These factors were eventually empirically determined.

Jeong and No (1996)

Jeong and No (1996) mainly focused on developing a correlation for describing the initial droplet size just after the dryout place at low mass flux conditions. For such conditions in the post-dryout region, it was recommended by the author to use the wall-vapor heat transfer correlation from Webb and Chen, which is derived from the data of low flow. The initial droplet diameter model was determined through fitting by comparisons of the wall and vapor temperatures.

Guo and Mishima (2002)

Guo and Mishima (2002) developed a non-equilibrium model that accounted for 6 possible heat transfer processes involved in a dispersed flow, including the forced convection of vapor phase to the wall, the direct contact heat transfer of droplets to the wall, the interfacial heat transfer between vapor and droplets, and the thermal radiation among the wall, the droplets and the vapor. Assumptions of the model are made as below,

1) at any given cross-section of the flow channel, all droplets are spherical and have the same diameter, d. The droplet diameter is a function of axial position or vapor quality,
2) and all phases have a uniform distribution of velocities and temperatures across a given cross-section, and the droplets are at the saturation temperature.

The convective heat transfer is attributed to the turbulent convection, resulting in heat or momentum transfer. The well-known analogy between heat transfer and momentum transfer was used, as suggested by Chen et al. (1979). Wall-droplet contact heat transfer was considered, because the author thinks it does contribute to the total heat transfer, particularly at low pressure and low mass flux conditions. The droplet diameter d was evaluated by the Kataoka et al. (1983) model, expressed as below,

$$d = 0.00796 \frac{\sigma}{\rho_v \left(\alpha U_v\right)^2} Re_v^{2/3} \left(\frac{\rho_v}{\rho_d}\right)^{-1/3} \left(\frac{\mu_v}{\mu_d}\right)^{2/3} \tag{2.32}$$

where, μ_d is the dynamic viscosity of droplet. Another important part of this model is the consideration of thermal radiation among the wall, the vapor, and the droplets. The radiation heat flux among the nodes can be expressed as

$$q''_{r,w-v} = \varphi_{w-v}\sigma_B \left(T_w^4 - T_v^4\right) \tag{2.33a}$$

$$q''_{r,w-d} = \varphi_{w-d}\sigma_B \left(T_w^4 - T_d^4\right) \tag{2.33b}$$

$$q''_{r,v-d} = \varphi_{v-d}\sigma_B \left(T_v^4 - T_d^4\right) \tag{2.33c}$$

where, $q''_{r,w-v}$, $q''_{r,w-d}$, and $q''_{r,v-d}$ are the thermal radiative heat fluxes between wall and vapor, wall and droplets, and vapor and droplets, respectively. φ is the gray-body factor, σ_B is the Stefan-Boltzmann constant. T_w, T_v, and T_d are temperatures of wall, vapor, and droplets, respectively. All temperatures are in the unit of K.

Cheng et al. (2018)

Cheng et al. (2018) developed a mechanistic model to predict the post-dryout heat transfer with consideration of convective heat transfer between wall and vapor, interfacial heat transfer between vapor and droplets, and direct contact heat transfer between wall and droplets. An effective two-phase mixture temperature T_{TP} was used to evaluate the mixture properties, and T_{TP} is shown as below,

$$T_{TP} = \alpha T_v + (1-\alpha) T_d \tag{2.34}$$

where, T_v and T_d are temperatures of vapor and droplet. The Dittus-Boelter correlation was applied to calculate the heat transfer coefficient of convective heat transfer between wall and vapor, shown as below,

$$h_{w-v} = 0.023 Re_{TP}^{0.8} Pr_{TP}^{1/3} \frac{k_{TP}}{D_T} \tag{2.35}$$

With properties evaluated at the effective two-phase mixture temperature T_{TP}. Besides, the interfacial heat transfer coefficient between vapor and droplets was calculated with the correlation of Jones and Zuber (1977). The most important part of this work that differs from the work in the past comes from the modelling of direct contact heat transfer between wall and droplets. The possibility for a droplet reaching the wall was analyzed with the following assumptions,

1) uniform droplets distribution at one axial elevation, but changing with elevation,
2) the turbulent velocity fluctuation of both phases obeys the Gaussian profile,
3) to reach the wall, the turbulent kinetic energy of the droplet should overcome the work done by the so-called evaporation force.

Furthermore, it was assumed that not all droplets arriving the wall would deposit on the wall and evaporate. It depends on the wall temperature. If the wall temperature is significantly higher than the Leidenfrost temperature, the droplet reaching the wall hardly deposits on the wall and evaporates. If the wall surface temperature is much lower than the Leidenfrost temperature, it will deposit on the wall and evaporate completely. The author used a wall superheating of 100 °C as the Leidenfrost temperature, according to Jones (1981). The model well predicted the sudden increase in wall temperature. Moreover, a slow increase in wall temperature before the sudden increase was predicted by the author. Based on the treatment of direct contact heat transfer between the wall and droplets, the hysteresis phenomenon of the flow boiling curve was obtained and explained by the Leidenfrost effect.

2.2.3. Multi-dimensional phenomenological models

Webb and Chen (1982)

Webb and Chen (1982) developed an analytic model for the prediction of two-phase turbulent, non-equilibrium, and dispersed flow heat transfer in post-dryout flow. The thermodynamic non-equilibrium was treated through a vapor generation source function in the vapor conservation equations to represent the heat sink and mass source effect of the droplet evaporation. The general set of six conservation equations for two-phase flow were simplified by considering radial geometry in a round tube with upward vertical flow. Some of the most important assumptions are 1) negligible direct wall to liquid heat transfer, 2) radially uniform droplet distribution, and 3) uniform heating of vapor due to radiation heat transfer. The key of the work was to solve the vapor conservation equations and to include the liquid vaporization effects through the vapor source function. The number of droplets was assumed constant so that the droplet size is a function of axial location. The model was compared with sixteen data points by varying the value of a coefficient for each run until the vapor temperature was matched at the measurement location. However, the correlation for the coefficient used in the vapor generation source function was not proposed in this research.

Chung and Olafsson (1984)

Chung and Olafsson (1984) adopted numerical solutions to study the convective and radiative heat transfer to a turbulent two-phase droplet flow in a tube. All kinds of thermal radiative heat transfer were included. The major assumptions in this numerical simulation are listed as below,

1) the existence of droplets does not affect the vapor velocity profile and the eddy diffusivity due to relatively high starting quality and small droplets,
2) The droplet distributes uniformly at any cross-section due to turbulent mixing, and the droplet diameter is uniform at each cross-section due to the radial mixing and uniform evaporation,

3) and the heat transfer between the droplets and the wall by direct contact is negligible when the temperature of the wall is above the Leidenfrost temperature.

The author also investigated the enhancement of heat transfer due to the dispersed droplets. The results indicated that smaller droplets and a higher saturation temperature represent a more efficient sink in the system. The enhancement decreases along the flow direction due to the evaporation of droplets. Finally, the author concluded from the results of the study that the contribution of radiative heat transfer could not be neglected in two-phase systems with moderate to high saturation temperatures and high wall heat fluxes. The radiation heat transfer becomes increasingly important for larger droplets. The heat sink capacity of the droplets is more efficient for smaller droplets.

Andreani and Yadigaroglu (1997)

Andreani and Yadigaroglu (1997) developed a hybrid Eulerian-Lagrangian model to analyze the dispersed flow film boiling in a vertical straight tube under typical reflooding conditions. The effect of the liquid phase on the vapor field, which was established in a two-dimensional grid, was calculated by tracking the three-dimensional trajectories of a large number of sample droplets. Two main limitations were indicated by the author that affect the predictions of models: the assumption of uniform droplet concentration over the cross-section or the use of a profile resulting from turbulent diffusion, and lack of an adequate modelling of the break-up processes.

The author employed a Lagrangian description of the liquid phase and a Eulerian treatment of the vapor field with several assumptions as below,

1) the situation at some distance downstream from the dryout changes relatively slowly, so that the steady-state conservation equations are used,
2) constant pressure for the high void fraction mixture flowing at low velocity is adopted,
3) one-way coupling exists between the velocity fields of the two-phases: the influence of the vapor velocity on the droplet velocities is considered, but the action of the dispersed phase on the turbulent vapor-phase characteristics is neglected,
4) the mechanism of collisions between droplets is not explicitly modelled, and
5) radiation heat fluxes are calculated using an effective droplet diameter.

For the simulation of droplet hydrodynamics, four transverse forces including transverse drag force, thrust force, lift force, and turbulent dispersion force were included. It was concluded that the thrust and lift forces are equally effective in preventing droplets from depositing on the wall. As observed by Ganić and Rohsenow (1979), the thrust force is associated with the drop motion in dispersed flow film boiling. Because of the temperature gradient in the thermal boundary layer, the side of the droplet closer to the wall evaporates at a higher rate, and vapor is produced at a higher velocity than that on the cold side. This model considers the droplet break-up mechanisms as aerodynamic break-up, wall-impact break-up, and capillary break-up. Thermal radiative flux was considered to be transferred to each group in proportion to its volumetric flow rate. The droplet was assumed to exchange heat directly with the wall when the distance of its center from the wall is smaller than its radius. The effectiveness of the contact was used to represent the ratio of the heat exchanged to that needed to evaporate the droplet completely.

Keizo et al. (2005)

Keizo et al. (2005) carried out post-dryout heat transfer analysis by using the Lagrangian simulation method to simulate the droplet behavior and incorporating a post-dryout heat transfer model to deal with the many heat transfer paths and non-equilibrium status. The equation of droplet momentum was developed by considering the forces acting on droplets, including drag force, gravity (including buoyant force), and lift force. Numerical integration was conducted using the Runge-Kutta method to solve the behavior of each droplet. Droplet turbulence diffusion was modelled according to the Discrete Droplet Model. Six heat transfer mechanisms, including the wall-vapor convection, vapor-droplet interfacial heat transfer, wall-droplet direct contact heat transfer, and three thermal radiation paths among the wall, vapor, and droplets, were modelled. The analysis results indicated that most of the heat transfer from the wall surface is wall-vapor convective heat transfer, and the heat transfer rate due to droplet contact is 0.1% of the total or less. Moreover, the author indicated that the effects of the turbulence modification on both the flow field and the temperature field are not negligible, even though wall-droplet direct contact heat transfer itself is negligible.

Meholic (2011)

Meholic (2011) developed a first-principles approach to quantify the heat transfer attributed to direct contact. Lagrangian droplet trajectory calculations incorporating realistic radial vapor velocity and temperature profiles were performed to determine if droplets could contact the heated wall based upon the local conditions. A two-dimensional force balance was utilized to determine the trajectory of a given droplet in the vicinity of the heated wall. The droplet force balance was performed in the momentum boundary layer. Assumed incompressible flow, the forces acting upon the droplets are the drag force, body force, lift force, and differential evaporation force.

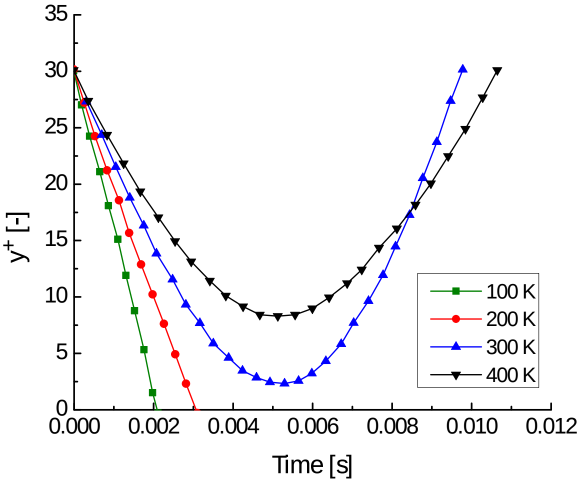

Figure 2.3.: Droplet trajectories for various wall superheats [source: (Meholic, 2011)].

Near the wall in the boundary layer, a considerable temperature gradient was present. Thus, the side of the droplet closer to the wall experiences a higher vapor temperature, resulting in more evaporation than the opposite side of the droplet. The evaporating vapor velocity difference results in a pressure gradient, which acts to repel the droplet away from the wall and prevent deposition. The evaporation force is significant in the near-wall region. Both convective and thermal radiative heat transfer can contribute to the evaporation of the droplet. The convective heat transfer results from the relative velocity between the droplet and continuous vapor. The radiative heat transfer from the wall becomes increasingly crucial as the temperatures increase. These calculations were performed over a droplet size spectrum accounting for various droplet diameter effects. When contact was achieved, the heat transfer was quantified by coupling the mass flux of droplets contacting the wall with a direct contact heat transfer coefficient. The droplet trajectory was found to be sensitive to the droplet diameter, wall superheat, vapor superheat, and mass flux. An example of the effect of wall superheat is shown in Figure 2.3. While the wall superheat is high, the droplets are likely to be repelled away by the wall. While wall superheat is lower than some certain value, the droplet can contact the wall.

The developed model included both the thermal radiative and the interfacial heat transfer between vapor and droplets. Three components were accounted for thermal radiative heat transfer, which is developed by Sun et al. (1976). Gnielinski (1976) correlation was used for convective heat transfer between wall and vapor, shown as below,

$$Nu_{w-v} = \frac{\frac{f_v}{8}\left(Re - 1000\right) Pr}{1 + 12.7\sqrt{\frac{f_v}{8}}\left(Pr^{2/3} - 1\right)} \tag{2.36}$$

where, f_v is friction factor of vapor. The interfacial heat transfer provided by the dispersed droplets was predicted by adapting the Lee and Ryley (1968) model to account for the varying droplet velocity and interfacial area across the droplet size spectrum in addition to the vapor temperature distribution, as shown in below,

$$Nu_{v-d} = 2 + 0.74 Re_d^{0.5} Pr_v^{0.33} \tag{2.37}$$

where, Nu_{v-d} is the Nusselt number of the interfacial heat transfer between vapor and droplets, Re_d is the droplet Reynolds number. The Lagrangian trajectory calculations captured the convective enhancement due to the dispersed droplets intermittently altering the vapor temperature distribution. Dispersed droplets in the boundary layer decrease the local temperature, effectively increasing the temperature gradient at the wall and convective heat transfer. Thus, the enhancement was found as a ratio of vapor temperature gradients at the wall, shown as below,

$$\frac{q''_{w,droplets}}{q''_{w,no-droplets}} = \frac{\left.\frac{\mathrm{d}T_v}{\mathrm{d}y}\right|_{w,droplets}}{\left.\frac{\mathrm{d}T_v}{\mathrm{d}y}\right|_{w,no-droplets}} \tag{2.38}$$

The contribution of each heat transfer component was investigated. In general, the wall to vapor convection and the vapor to liquid heat transfer components are found to be the dominant heat transfer paths. However, the direct contact heat transfer can contribute up to 6.0% of the total heat transfer. This indicates the direct contact heat transfer between wall and droplets must be included in the model. The thermal radiation components are less important than the previous components. The wall to vapor radiation is the largest of the three thermal radiation components followed by the vapor to liquid and wall to liquid contributions, respectively.

Torfeh and Kouhikamali (2015)

Torfeh and Kouhikamali (2015) simulated the mist flow regime in a vertical tube by using a discrete phase model. The discrete phase was simulated in a Lagrangian approach, and the coupling between phases was modelled through interaction terms in the transport equations. The transverse forces, including virtual mass, lift force, and the thermophoretic force, were considered by the author. Ranz et al. (1952) correlation was used to calculate the interfacial heat transfer between vapor and droplets. The author did not consider the direct wall-droplets contact heat transfer and thermal radiation.

Li and Anglart (2016)

Li and Anglart (2016) developed an integrated CFD model for high quality two-phase flow, including trans-dryout regions from annular-mist regime to mist regime. The model was based on a three-field description of droplets, gas, and liquid film for annular-mist flow, which incorporates both the pre and post dryout regions, with local models for determination of the dryout occurrence.

The thin liquid film model was coupled to the gas core flow model, which is described by using the Eulerian-Eulerian approach. The dryout occurrence was predicted by using a critical film thickness model from system code MARS, which is based on the combination of the RELAP5 and the COBRA-TF codes (Chun et al., 2003), the critical liquid film thickness $\delta_{c,lf}$ is shown as below,

$$\delta_{c,lf} = \frac{\left(\frac{1}{\rho_v} - \frac{1}{\rho_{lf}}\right) \mu_{lf}^2}{\sigma} \times 10^{8.8\left(\frac{\mu_v}{\mu_{lf}}\right)^{0.617}} \left(\frac{q_w^{''}}{i_{v-d} G_{lf}}\right)^{0.35} \tag{2.39}$$

where, G_{lf} is the liquid film mass flux, ρ_{lf} is density of liquid film, μ_{lf} is the dynamic viscosity of liquid film, and $q_w^{''}$ is the wall heat flux.

The gas core flow contains two phases, the gas, and the droplet. Both the phases are described by using the Eulerian conservation equations based on the two-fluid model. Modelling was based on experience from particle flow, and the drag force was the primary driver to accelerate the droplets in the gas, which is calculated by using the Schiller-Naumann model. The virtual mass force was neglected. The Favre Averaged Drag model was used for simulating the turbulent dispersion force. Due to the fact that the lift force in droplet dispersed flow is not well established for a two-fluid model, the lift force was not taken into account in the model. This work did not discuss the evaporation force.

For the post-dryout heat transfer, mechanisms in convective heat transfer between wall and vapor, interfacial heat transfer between vapor and droplets, and direct contact heat transfer between wall and droplets, were considered. The convective heat transfer was calculated in the wall function, for which the Jayatilleke model was used. The Ranz-Marshall model was used for interfacial heat transfer, and the influence of mass transfer between phases was considered. For the wall-droplets direct contact heat transfer, Guo and Mishima (2002) model was used. Finally, four tests from Becker experiment were used to compare with the model. The comparison results were satisfied. Nevertheless, the CFD model always gives a decreasing wall superheat profile in the simulation. This could be due to no transverse force that prevents droplets contact the wall was considered. Thus, droplets are very quickly getting evaporated, and the wall cooling was overestimated.

2.3. Conclusion of difficulties in the modelling of post-dryout heat transfer

To sum up the review of previous models, most these modelling works consider the three-path heat transfer that involves heat transfer from i) the heated wall to vapor, ii) from vapor to droplets, and iii) from wall to droplets including direct contact and thermal radiation. The most crucial unknown in post-dryout flow is the thermal non-equilibrium, which is strongly associated with the presence of droplets. Difficulties in predicting post-dryout heat transfer are mainly due to the impacts of the concentration and spectrum of the droplets on two aspects: one is the alteration on the convective heat transfer coefficient by the modification of the vapor temperature profile and the modifications of the vapor velocity and thermal boundary layers. Another is the alteration on the interfacial heat transfer by the modification of vapor superheat and interfacial area. Most of the models adopt the characteristic droplet size instead of the spectrum of the droplets. The summarized works differ at how the droplet related hydrodynamics are considered, e.g. droplets' deposition on the wall, droplets size variation in the axial direction, droplets' distribution in the radial direction, and whether the modification of the vapor temperature profile and the modifications of the vapor velocity and thermal boundary layers are considered. Generally, the existing models for post-dryout heat transfer range from very simple equilibrium correlations to complex multidimensional mechanistic models. Each kind of approach presents merits and limitations in consideration of the most concerned difficulties in post-dryout heat transfer modelling.

The correlations based on the assumption of thermal equilibrium are easy to use and might give sufficiently accurate results for conditions of high pressures with moderate-to-high mass fluxes. For such conditions, the post-dryout flow has a small non-equilibrium degree typically. Thus, the actual quality is always considered as equilibrium quality. The flow can be considered as thermal equilibrium mixture flow, for which models based on the modification of the Dittus-Boelter equation are sufficient enough to be applied. However, this kind of correlations predicts obviously wrong results for conditions of low pressures and mass fluxes, where substantial non-equilibrium can develop.

For the prediction of thermal non-equilibrium, difficulties remain in the considerations of the concentration and spectrum of the droplets, especially under the conditions of low pressures and mass fluxes, where substantial non-equilibrium can develop. Both one-dimensional separated flow model and multidimensional CFD approach can phenomenologically describe the thermal non-equilibrium degree. However, it is hard for one-dimensional separated flow models to consider the droplets concentration distribution over the cross-section. The commonly adopted assumption of uniform distribution of droplets in such models can result in wrong estimations of the vapor-droplets interfacial heat transfer. As for the CFD approach, a larger predictive capability can be obtained. However, CFD is computationally expensive, and the models applied in CFD still need quite extensive knowledge of the physical phenomena to improve the prediction. Many subprocesses and their influences over the wall-droplets contact heat transfer and the interactions between vapor and droplets are still unknown in sufficient details. Consequently, the various multidimensional CFD approaches have received only limited assessment, including typically a few experimental tests.

Additionally, because of the presence of evaporating droplets, the vapor turbulence and temperature profile over the cross-section can be modified and the magnitude varies intensively along with the flow direction. A general convective heat transfer for various fluids is challenging to develop. Many empirical correlations are limited to specific fluid, though some attempts proposed Nusselt number correcting factor for the effects caused by the presence of droplets. Influences on the wall-vapor convection due to the presence of evaporating droplets should be studied and classified in detail. Unfortunately, this part of work was not improved in the current work since the primary attention was paid on improvements in the prediction of non-equilibrium, which is more critical to post-dryout heat transfer. Usually, the droplet size distribution at a given axial position is characterized by an average droplet diameter and varies along the flow direction by uniform evaporation without break-up considerations. Though droplets break-up can happen in the post-dryout region, no clear evidence indicated this effect is significant.

These merits and limitations of different kinds of approaches lead to the considerations in the current modelling work. The impacts of the droplets' concentration distribution over the cross-section on the interfacial heat transfer between vapor and droplets are considered and focused. Flow region is divided into a film region and a core region. This division makes it possible to consider the droplets' concentration distribution in one-dimensional separated flow models. Details of the proposed post-dryout model are introduced in the next chapter.

3. Model development of post-dryout heat transfer

A brief introduction to the theoretical modelling of full-range post-dryout heat transfer in vertical tubes is presented in this chapter.

3.1. Determination of flow regions

Figure 3.1 shows that the whole post-dryout heat transfer region consists of a developing region and a fully developed region. The flow pattern of the developing region is unstable film boiling with a dispersed flow. Heat transfer enhancements characterize this region because of a residual disturbance, which is caused by the CHF occurrence and the entrained droplets from sputtering liquid (Guo and Leung, 2005). The upstream CHF occurrence enhances the convective heat transfer between wall and vapor by increasing the vapor turbulence while the entrained droplets improve the wall-droplets contact heat transfer. Heat transfer in the fully developed region is not affected by the upstream CHF history, and it depends solely on the local flow conditions (Köhler and Hein, 1986). However, the upstream history started from the formation of the droplets, whereas the onset of annual film boiling can influence the droplet related variables. Moreover, the wet contact heat transfer between the wall and droplets becomes less frequent in the fully developed post-dryout region. The flow pattern in this region is called stable Dispersed Flow Film Boiling (DFFB).

3.1.1. Definitions of two regions

Guo and Leung (2005) defined the developing post-dryout region as the region between the dryout place and the location, where the wall temperature reaches the maximum local value. However, from the experimental data of the axial distribution of wall temperature, a maximum local wall temperature sometimes does not happen in the post-dryout region, but the wall temperature grows steadily along with the tube from post-dryout flow into single vapor convection. Therefore, the terms *developing post-dryout region* and *fully developed post-dryout region* are proposed in this work as follows:

- *Developing post-dryout region*: the region starts from the liquid film dryout place, and ends where the wall surface starts to be fully covered by vapor. The flow structure in this region develops to be relatively stable, and the wall temperature grows fast, as well as the near-wall vapor temperature.s

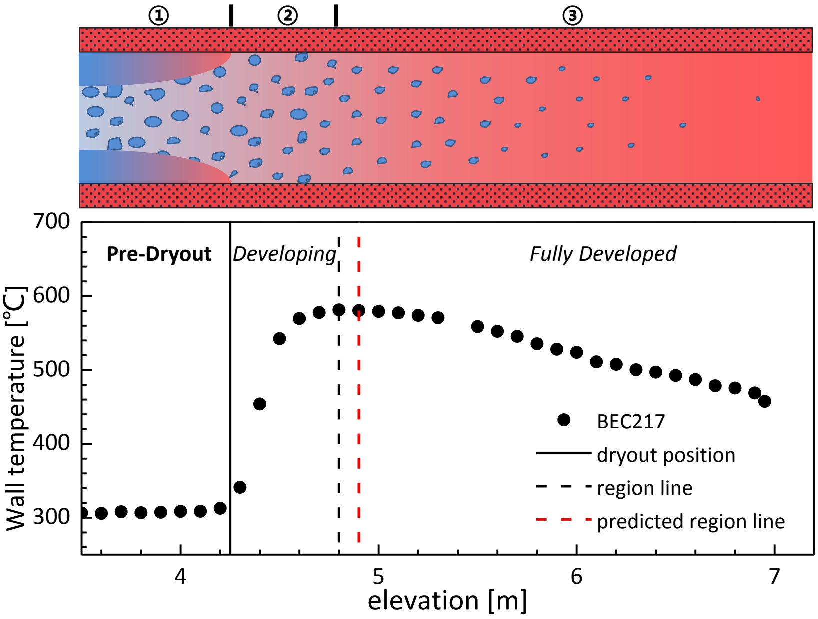

Figure 3.1.: Typical flow patterns and wall temperature profile in the post-dryout region (run no.: 217 (Becker et al., 1983)). ① annular flow; ② unstable or partial film boiling dispersed flow; ③ stable film boiling dispersed flow.

- *Fully developed post-dryout region*: the region begins where a stable and continuous vapor phase has been established. The flow pattern can be called stable mist flow or the stable dispersed flow film boiling. In this region, the wall temperature grows moderately, or first decreases and then increases, and the droplets do not have wet-contact with the wall.

The developing post-dryout region is usually considered starting from the dryout location, up to a constant distance (Chen, 1986), or up to the place where the Graetz number of vapor Gz_v becomes very small (Nguyen and Moon, 2015). A determinative correlation for calculating the length of the developing post-dryout region is still missing according to the public records. In the current work, a large amount of experimental data, which is coming from both the water based Becker experiment (Becker et al., 1983) and our own R-134a based KIT experiment (Köckert et al., 2018), are used to develop an empirical correlation for the length of the developing post-dryout region.

3.1.2. Determination and analysis of the developing region length

First, the separation of the two regions shall be based on the physical phenomenon. It is considered as the place, where the wall temperature starts to grow moderately, or to reach the maximum local value, if existing. The place is considered as a sign of transition of those two regions. The experimental data of the wall temperature show that the local maximum wall temperature does not happen sometimes in the post-dryout region. Instead, the wall temperature always grows slowly also in the fully developed region, in which the flow condition is assumed to have a high non-equilibrium degree.

The accuracy of the method below for determining the regions separation place is limited to the experimental databank itself. The method is applied to both Becker and the KIT experiments. Finally, the obtained regions separation point is close to the location, where the wall temperature starts to grow slowly, or close to the location, where the maximum local wall temperature occurs if existing. The location is assumed as the two regions transition place, and its determination method shall be described as the following steps:

- **(a) data filtering**

  Post-dryout flow develops at void fractions higher than 80%, according to the widely accepted criterion of Groeneveld (1975), which has found confirmation in a few experimental investigations (e.g. Kawaji (1984)). Since the void fraction is not measured in the experiment, in the current work, the void fraction α is calculated by equation below,

  $$\alpha = \frac{1}{\frac{1-x_a}{x_a}\frac{\rho_v}{\rho_d}S + 1} \tag{3.1}$$

  where, x_a is the actual quality, ρ_v and ρ_d are densities of vapor and droplet, and the velocity slip ratio S used is determined by Yoder and Rohsenow (1983),

  $$S \equiv \frac{U_v}{U_d} = 1 + 2.31 \left[\frac{\rho_d}{\rho_v} \frac{1}{x_a} \frac{q_w^{''}}{G i_{v-d} C_D} \frac{d}{D_T} \right]^{0.5} \tag{3.2}$$

  where, U_v and U_d are the velocities of vapor and droplet in the flow direction, x_a is the actual quality, i_{v-d} is the latent heat of vaporization, $q_w^{''}$ is the wall heat flux, G is the inlet mass flux, C_D is the droplet drag coefficient, d is the droplet diameter, and D_T is the inner tube diameter. In the current work, this equation is used for the whole post-dryout region except at dryout, at where the full form of this equation (3.18) is applied. Herein, the velocity slip ratio at dryout S_{do} uses the full form in Eq. (3.18).

  C_D was developed by Groeneveld (1972) for dispersed flow analysis,

  $$C_D = \frac{27}{Re_d^{0.84}} \qquad Re_d < 150 \tag{3.3a}$$

  $$C_D = 0.4 \qquad Re_d \geq 150 \tag{3.3b}$$

  Re_d is the droplet Reynolds number and is defined as below,

  $$Re_d = \frac{\rho_v \left(U_v - U_d\right) d}{\mu_v} \tag{3.4}$$

  The test runs are selected with the criterion of dryout void fraction $\alpha_{do} > 0.8$ to ensure that most of the tests' conditions are in the post-dryout heat transfer region. Finally, 187 runs in the water based Becker experiment and 125 runs in the R-134a based KIT experiment are selected. The calculation of droplet diameter, which is used in Eq. (3.4), will be introduced in section 3.3.1.

- **(b) grouping and picking**

  For each selected test run, n data points $\{\ P_0 \cdots\ P_i \cdots\ P_n\ \}$ have been obtained.

  Following the sequence, a group of every four neighboring points e.g. $\{\ P_{i-2}\ P_{i-1}\ P_i\ P_{i+1}\ \}$ is selected, such that $n-1$ groups can be obtained. For each group, a straight line is fitted as a relationship of wall temperature versus equilibrium quality by using least-squares regression.

  The maximum local slope of the regression lines just downstream the dryout is characterized as the maximum slope. Find the first group where its slope is lower than 20% of the maximum slope. Then, the fourth point in the selected group is finally picked as the two regions transition place. The developing post-dryout region length L_{dev}, in the current work, is defined as the equilibrium quality difference between the two regions transition place and the dryout.

An investigation has been performed to analyze the influence of parameters on the developing post-dryout region length L_{dev}, which could be modelled by a series of possibly relevant dimensionless numbers that are derived from independent variables. Two effects caused by Reynolds number Re and the Boiling number Bo are found to be most significant and will be shown below.

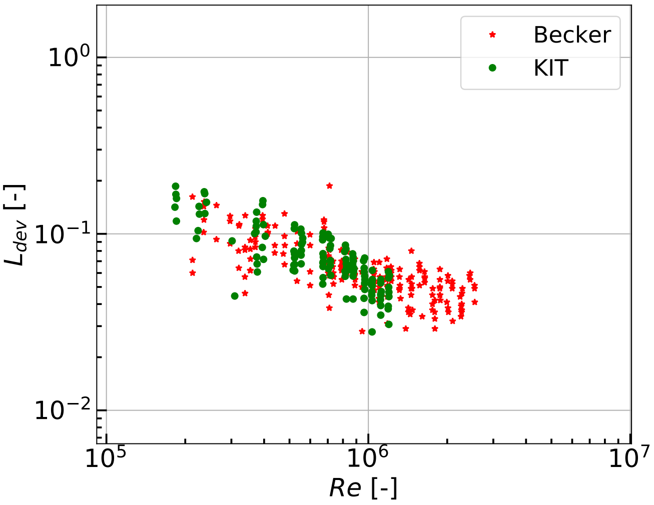

Figure 3.2.: Influence of Reynolds number on the length of the developing post-dryout region.

Heat transfer in the developing post-dryout region could be regarded as a transient, entrance-region problem (Chen, 1986). One of the main factors, which results in heat transfer enhancement in the developing post-dryout region is the residual disturbance due to the dryout occurrence. Therefore, the length of developing post-dryout region L_{dev} changes with Reynolds number Re, as shown in Figure 3.2. Both experiments indicate that the developing post-dryout region length and Reynolds number are inversely correlated. Generally, the larger the turbulent intensity of the flow is, the shorter the developing region length will be.

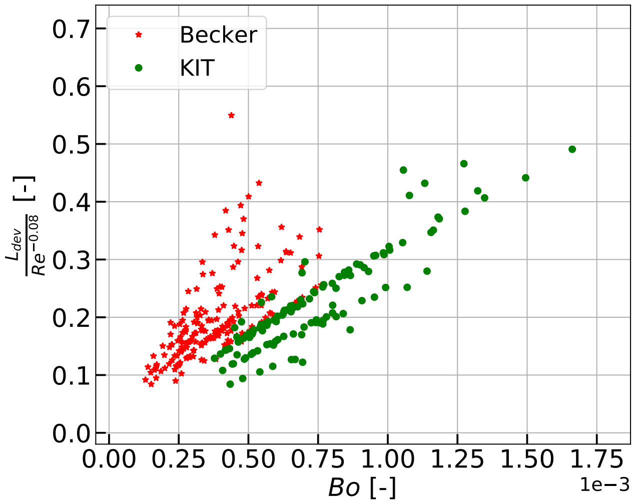

Figure 3.3.: Influence of the Boiling number on the length of the developing post-dryout region.

Another main factor resulting in heat transfer enhancement in the developing post-dryout region is the droplet evaporation, which is mainly caused by the direct wall-droplets contact heat transfer and the interfacial heat transfer between droplets and highly superheated vapor in the near-wall region. The Boiling number represents a stirring effect of the droplets upon the flow, which could reflect the influence of droplet evaporation on the developing post-dryout region length. For isolating the effect on L_{dev} which is caused by Re, an item $Re^{-0.08}$, which is a fit to the plots in Figure 3.2, is divided by L_{dev}. Then the influence of the Boiling number on the length of developing post-dryout region is investigated, as shown in Figure 3.3. Both experiments indicate that the developing post-dryout region length and the Boiling number are positively correlated. Generally, the higher the Boiling number is, the longer the developing region length will be.

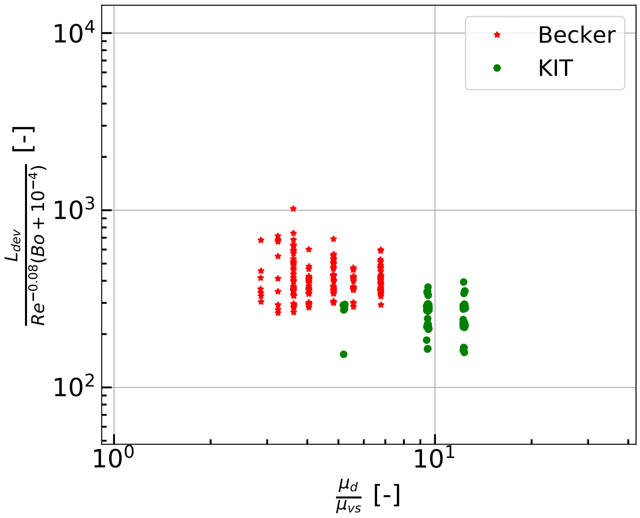

Figure 3.4.: Influence of the viscosity ratio on the length of developing post-dryout region.

For different fluids, influences of the Boiling number on the length of the developing post-dryout region show a similar trend but vary in intensity. To develop a general correlation for L_{dev}, a viscosity ratio $\frac{\mu_d}{\mu_{vs}}$ is used to correct the correlation for different fluids. As shown in Figure 3.4, two fitted items are divided by L_{dev} for isolating the effects caused by Re and Bo. Then the influence of the viscosity ratio is found to have an inversely correlated relationship.

3.1.3. Development and assessment of the length predicting correlation

Based on the above investigations, the post-dryout region length L_{dev} is defined as the equilibrium quality difference and is correlated in the current work. Equations are expressed as follows,

$$L_{dev} \equiv x_{rt} - x_{do} = 900Re^{-0.08}(Bo + 10^{-4})\left(\frac{\mu_d}{\mu_{vs}}\right)^{-0.55} \tag{3.5}$$

where, x_{rt} is the equilibrium quality at the two regions transition place, which is the same as the location at the end of the developing post-dryout region. x_{do} is the equilibrium quality at dryout. μ_d and μ_{vs} are the saturated dynamic viscosity of droplet and vapor, respectively. All fluid property related variables are evaluated at saturation temperature, and definitions of the Boiling number Bo and Reynolds number Re used in the equation are shown as below,

$$Bo = \frac{q_w''}{Gi_{v-d}} \tag{3.6a}$$

$$Re = \frac{GD_T}{\mu_{vs}} \tag{3.6b}$$

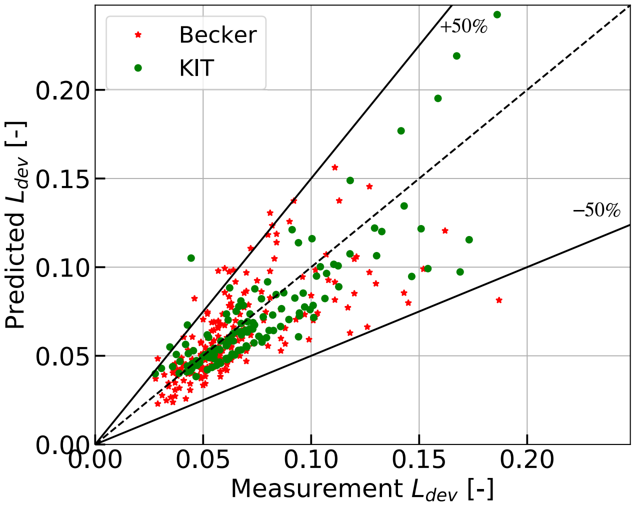

Figure 3.5.: Predictions of the developing post-dryout region length.

Table 3.1.: Developing post-dryout region length L_{dev} predicting accuracy.

	Becker, water	KIT, R-134a	Total
number of points	187	125	312
average e [%]	-0.15	-2.65	-1.16
RMS e [%]	26.62	23.45	25.40

The accuracy of the length predicting correlation is evaluated. Figure 3.5 shows that most of the data points are within the deviation range of ±50%. Herein, the predicting error e is defined as,

$$e = \frac{predicted\ L_{dev} - measurement\ L_{dev}}{measurement\ L_{dev}} \tag{3.7}$$

As shown in Table 3.1, there were 312 test runs compared in total, and the average error and root-mean-square (RMS) error of the predictions are -1.16% and 25.40%, respectively.

3.1.4. Conclusion

To sum up, due to the different flow patterns in the developing and fully developed post dryout regions, it is necessary to distinguish these two regions in the proposed model. A new definition of terms *developing post-dryout region* and *fully developed post-dryout region* is proposed to solve the inconsistency between the measurement and the previous description of the definition by Guo and Leung (2005). To develop a correlation for predicting the developing region length L_{dev}, a method through using the wall temperature slope is applied to both the Becker and KIT experiments to determine the measured two regions transition place. Having obtained the measured L_{dev}, the influence of parameters on L_{dev} is analyzed. Results show that the Reynolds number Re and the Boiling number Bo are strongly associated with L_{dev} in a similar way in both experiments, respectively. Finally, a general correlation is proposed to predict L_{dev}, as shown in Eq. (3.5). The comparison shows that the proposed correlation has a good agreement with both experiments.

3.2. Wall-vapor convective heat transfer

Convective heat transfer between wall and vapor gives the largest contribution to the wall heat removal. The convective heat transfer coefficient in post-dryout heat transfer can be larger or smaller than in single-phase flow since the dispersed phase alters convection by two mechanisms: (a) modification of the temperature profile and (b) modification of the velocity and thermal boundary layers. The first effect results in a strong reduction of the vapor temperature in the near-wall region, which enhances the heat transfer. The second effect is due to the alteration of the viscous sublayer thickness and the slope of the vapor velocity profile, which strongly affects the structure of turbulence that may dampen or increase the turbulence while droplets are in the core. However, these effects are not studied in the current work since the modifications on both the vapor turbulence and the temperature profile are varying along with the tube, and the effects are difficult to be isolated from one to another. Surveys of the works on these topics have been reported by Andreani and Yadigaroglu (1989) and Hetsroni (1989).

In the full-range of post-dryout conditions, the prediction of convective heat transfer in the current work is always regarded as a transient, entrance-region problem with axial distance from the dryout location, expressed as the combination of convective heat transfer at the dryout place and convective heat transfer for the fully developed post-dryout flow.

Numerous correlative models are available to predict the convective heat transfer between wall and vapor. However, most of the correlative works usually originate with a single phase wall-vapor convective heat transfer correlation, which is similar to the Dittus-Boelter equation as below,

$$Nu_{w-v} = 0.023 Re_v^{0.8} Pr_v^{0.4} \tag{3.8}$$

For predicting post-dryout heat transfer in various fluids, the most frequent way is to adopt different correlations for different fluid. For example, the correlation for superheated steam developed by Hadaller and Banerjee (1969) is suggested for water conditions, as shown below,

$$h_{w-v} = 0.008348 \frac{k_{vf}}{D_T} \left(\frac{G x_a D_T}{\mu_{vf} \alpha} \right)^{0.8774} (Pr_{vf})^{0.6112} \tag{3.9}$$

where, h_{w-v} is the heat transfer coefficient between wall and vapor, k_{vf} the film vapor thermal conductivity, μ_{vf} is the film vapor dynamic viscosity, and Pr_{vf} is the film vapor Prandtl number. All properties are evaluated at film vapor temperature. In other cases, e.g. for nitrogen conditions, the Forslund correlation (Forslund and Rohsenow, 1966) is suggested. For the remaining fluids (e.g. freon), the Dittus-Boelter equation with vapor properties evaluated at the film vapor temperature could be applied.

However, in the current work, a general convective heat transfer correlation for all fluids is proposed based on a modification of the existing correlation, which will be introduced in the section below.

3.2.1. Convective heat transfer coefficient in the fully developed post-dryout region

Attempts are made to use a single correlation for convective heat transfer in all fluids. The fully developed post-dryout convective heat transfer coefficient $h_{w-v,fdev}$ at any point of interest, is predicted by the modified Forslund correlation (Forslund and Rohsenow, 1966) in the current work. The original Forslund correlation was developed by using the film boiling tests with liquid nitrogen, and this correlation is found in the current work to have relatively good predicting accuracy in general both for water and R-134a. However, the prediction by using the original Forslund correlation shows a similar overestimation of the heat transfer coefficient in both fluids, when the wall-bulk temperature ratio increases. This is because the influence of lower density and higher viscosity fluid near the wall is not considered, while the wall temperature is high. To account for the large fluid property variations across the tube, a correction factor either in the form of temperature ratio (e.g. Eq. (2.1)) or in the form of viscosity ratio (e.g. Eq. (2.29)) can be multiplied with the convective heat transfer correlation as a conventional treatment. In the current work, a correction factor in the form of a viscosity ratio combined with a constant coefficient of 1.05 are multiplied with the original Forslund correlation. The exponent of the viscosity ratio and the constant coefficient are determined by comparing the proposed model with the experimental databank. Finally, the correlation is modified as below,

$$h_{w-v,fdev} = 0.035\frac{k_{vb}}{D_T}Re_{vb}^{0.743}Pr_{vb}^{0.4} \qquad original \tag{3.10a}$$

$$h_{w-v,fdev} = 0.03675\frac{k_{vb}}{D_T}Re_{vb}^{0.743}Pr_{vb}^{0.4}\left(\frac{\mu_{vb}}{\mu_{vw}}\right)^{0.1} \qquad modified \tag{3.10b}$$

where, k_{vb} is the thermal conductivity of vapor, and all the fluid properties in the above correlations are evaluated at the bulk vapor temperature, except for the vapor viscosity μ_{vw}, which is evaluated at the wall surface temperature. The Vapor Reynolds number Re_v and the vapor Prandtl number Pr_v are commonly defined in the current work as below,

$$Re_v = \frac{Gx_aD_T}{\mu_v\alpha_v} \tag{3.11a}$$

$$Pr_v = \frac{C_{p,v}\mu_v}{k_v} \tag{3.11b}$$

Then, the vapor Reynolds number Re_{vb} and the Prandtl number Pr_{vb} that are used in Eq.(3.10) are calculated by Eq.(3.11) with fluid properties evaluated at the bulk vapor temperature.

3.2.2. Convective heat transfer coefficient in the whole post-dryout region

The convective heat transfer coefficient in the whole post-dryout region is regarded as a combination of the convective heat transfer coefficient for fully developed post-dryout flow $h_{w-v,fdev}$ and convective heat transfer coefficient at dryout $h_{w-v,NB}$, expressed as follows,

$$h_{w-v} = (1-K_1)h_{w-v,fdev} + K_1h_{w-v,NB} \tag{3.12a}$$

$$q^{''}_{w-v} = h_{w-v}(T_w - T_{vb}) \tag{3.12b}$$

where, K_1 is the dimensionless weighting factor, representing the ratio of heat transfer rate at dryout to the heat transfer rate between wall and vapor in total. The value of K_1 varies from 1 at the dryout place to a small value that asymptotically approaches 0, when the fully developed region is reached. $h_{w-v,NB}$ is the heat transfer coefficient at dryout, which is calculated by the Chen correlation (Chen, 1966) for saturated nucleate boiling. To obtain the weighting factor K_1, a correlation is proposed in the current work, which has a similar structure as the weighting factor developed by Nguyen and Moon (2015). The constants in the correlation have been determined by comparison of the predicted wall superheat profiles in the developing post-dryout region with the experimental databank. Finally, the proposed correlation is shown as below,

$$K_1 = \frac{1}{1+\left(\frac{10^4}{Re_{vb}^{\frac{1}{6.0}}}\right)\left(\frac{L_{poi}}{L_{dev}}\right)^{2.5}} \tag{3.13}$$

where, Re_{vb} is defined by Eq. (3.11) with vapor properties evaluated at the bulk vapor temperature, and L_{poi} represents the length of the point of interest, which is the equilibrium quality difference between the point of interest and the dryout place.

3.3. Wall-droplets contact heat transfer

3.3.1. Droplet size model

As mentioned in chapter 1.1, the calculation of droplet size is important and complex. Many experimental and theoretical studies on the characteristic droplet diameter and the droplet size distribution in dispersed flow have been carried out. Several droplet generation mechanisms have been observed or postulated, as summarized by Varone (1990), including: (a) large chunks of liquid throw by boiling in the liquid film, (b) droplets erupted from the film into the vapor core by roll waves, named Helmholtz instabilities, (c) break-up effect after droplets being entrained in the vapor core, and (d) droplets deposition onto the liquid film. Numerous distributions have been used to characterize the droplets size spectrum including various forms of the normal, log-normal, and upper limited log-normal distributions. An example is the droplet size probability distribution function (PDF) that is utilized and recommended by Ganić and Rohsenow (1977) as shown below,

$$\mathrm{P}(d) = 4\frac{d}{\bar{d}^2}\exp\left[-2\left(\frac{d}{\bar{d}}\right)^2\right] \tag{3.14}$$

Herein, P represents the probability distribution function, $\bar{d}$ is the mass weighted average droplet diameter, exp is the exponential function. To further characterize the droplet size distribution, the mean droplet diameter $\bar{d}$ and the critical droplet diameter d_c are needed. The critical droplet diameter for standalone calculations is determined by assuming a critical droplet Weber number We_c in the range of $6 - 7.5$. The mean droplet diameter $\bar{d}$ can be calculated from the critical diameter by integrating to include 99.9% of the total volume. An example of the droplet size PDF, calculated by Eq. (3.14) with a critical diameter of 300 μm, is illustrated by Meholic (2011), as shown in Figure 3.6.

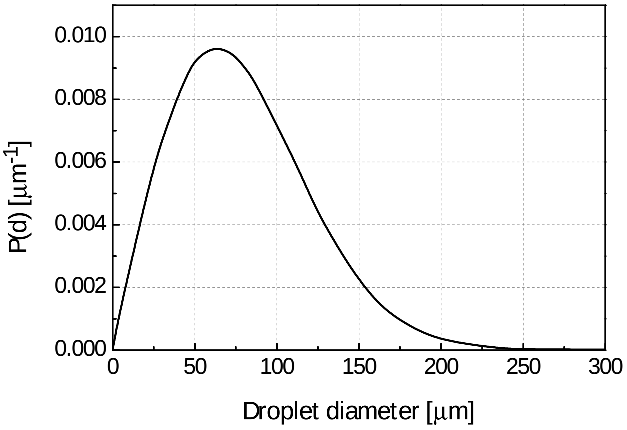

Figure 3.6.: Droplet size probability distribution function for a critical diameter of 300 μm and an average diameter of 126 μm [source: (Meholic, 2011)].

In the current work, the droplets size spectrum is not considered. Instead, the mass average droplet size is used at each axial location of the flow, and the droplet number flow rate is assumed remaining constant, even-though wall-droplets contact heat transfer could completely evaporate the depositing droplets. The droplets are considered as non-deformed spheres, and no break-up or coalescence is assumed to occur downstream of the dryout place. The fluid mass balance can be applied through the whole post-dryout region to calculate the average droplets size at any point of interest d_{poi}. The relation is written as below,

$$\frac{d_{poi}}{d_{do}} = \left(\frac{1-x_a}{1-x_{do}}\right)^{\frac{1}{3}} \tag{3.15}$$

where, d_{do} is the average droplets size at the dryout place, and is also called the initial average droplets diameter in the current work. x_a is the actual quality.

The calculation method for the initial average droplets diameter, that is used in the current work, was developed by Yoder (1980). The method is validated by water, Freon, and nitrogen data. It includes both the droplets formation from annular flow or inverted annular flow and the droplets break-up subsequent to the formation. The average droplet diameter at the dryout place calculated by this method also includes the effect of Weber number break-up downstream of the dryout. It averages the droplet break-up effects in the whole flow region. A summary of those equations for calculating the average droplet diameter at dryout d_{do} is listed as below,

$$\frac{d_c}{D_T} = \frac{\rho_v \sigma}{G^2 D_T} \frac{We_c}{(S_{do}-1)^2 \left(\frac{\rho_v}{\rho_d} + \left(\frac{1}{S_{do}} - \frac{\rho_v}{\rho_d}\right) x_{do}\right)^2} \tag{3.16}$$

$$\alpha_{do} = \frac{1}{\frac{1-x_{do}}{x_{do}} \frac{\rho_v}{\rho_d} S_{do} + 1} \tag{3.17}$$

$$S_{do} = \frac{1 + \sqrt{1 - \left(1 - \frac{4}{3} \frac{\rho_d \rho_v g \left(1 - \frac{\rho_v}{\rho_d}\right)}{G^2 C_D} d_c \left(\frac{\alpha_{do}}{x_{do}}\right)^2\right) \left(1 - \frac{16}{3} \frac{q''_w}{G i_{v-d} C_D} \frac{d_c}{D_T} \frac{\rho_v}{\rho_d} \frac{1}{x_{do}}\right)}}{1 - \frac{4}{3} \frac{\rho_d \rho_v g \left(1 - \frac{\rho_v}{\rho_d}\right)}{G^2 C_D} d_c \left(\frac{\alpha_{do}}{x_{do}}\right)^2} \tag{3.18}$$

$$S_{lf} \equiv \frac{U_v}{U_{lf}} = \left(\frac{\rho_{lf}}{\rho_v}\right)^{0.205} \left(\frac{G D_T}{\mu_{lf}}\right)^{-0.016} \qquad \text{Ahmad (1970)} \tag{3.19}$$

$$x_A = \frac{\left[\frac{S_{do}-1}{S_{lf}-1}\right] \left[\frac{\rho_v}{\rho_{lf}} + \left(\frac{1}{S_{do}} - \frac{\rho_v}{\rho_{lf}}\right) x_{do}\right] - \frac{\rho_v}{\rho_{lf}}}{\frac{1}{S_{lf}} - \frac{\rho_v}{\rho_{lf}}} \tag{3.20}$$

$$\begin{aligned} \frac{d_{do}}{D_T} = \frac{1}{x_{do}-0.1} \Bigg(\frac{d_c}{D_T}(x_A - 0.1) + \left(\frac{\rho_d}{\rho_v}\right)^2 \frac{We_c}{(S_{lf}-1)^2} \frac{\rho_v \sigma}{G^2 D_T} \frac{1}{(\frac{\rho_d}{\rho_v} \frac{1}{S_{lf}} - 1)} \\ \cdot \left[\frac{1}{1 + x_A(\frac{\rho_d}{\rho_v} \frac{1}{S_{lf}} - 1)} - \frac{1}{1 + x_{do}(\frac{\rho_d}{\rho_v} \frac{1}{S_{lf}} - 1)} \right] \Bigg) \end{aligned} \tag{3.21}$$

$$We_c = 6.5 \tag{3.22}$$

Note that all properties of droplets, vapor, and liquid film are evaluated at the saturation temperature T_s. The calculation procedure of the initial average droplets diameter d_{do} is to iterate over the above equations, and the droplet drag coefficient C_D is calculated by Eq. (3.3). S_{lf} is the liquid film velocity slip ratio. S_{do} is the droplet velocity slip ratio at dryout place. x_A is the equilibrium quality at the onset of annular flow. d_c is the critical droplet diameter, namely the maximum droplet diameter. α_{do} is the void fraction at dryout. U_v and U_{lf} are axial velocities of vapor and liquid film. ρ_{lf} is the density of liquid film. μ_{lf} is the dynamic viscosity of liquid film. σ is the surface tension, and g is the gravitational acceleration.

3.3.2. Heat flux between wall and droplets

Numerous researchers including Forslund, Kendall, Rohsenow, Ganic, and Guo developed models trying to account for the heat transfer to droplets through contacting the heated wall in post-dryout flow (Forslund and Rohsenow, 1968; Kendall and Rohsenow, 1978; Ganić and Rohsenow, 1977; Guo and Mishima, 2002). Kendall and Rohsenow (1978) implemented studies mainly on the heat transfer to droplets impacting on a hot surface. High heat transfer rates are found associated with wall surface wetting by the liquid, while wall surface temperatures are between the saturation and the minimum stable film boiling temperature. Low heat transfer rates are found associated with non-wetting or dry impacts at surface temperatures above the minimum stable film boiling temperature. Kendall found that there is less than 5% of the total heat transferred through wall-droplets contact heat transfer, of which the contribution is very limited. A full-range post-dryout heat transfer model should include this part of heat transfer since it affects the droplets size variation along with the tube. The contact heat transfer rate could be significant in the developing post-dryout region, especially while the wall superheat is not so high.

In the current work, wall-droplet contact heat transfer is characterized by a parameter called the effectiveness ε, which refers the ratio of the actual heat transferred during wall-droplet collisions to the heat needed to entirely evaporate all the deposition droplets. Then the heat flux between wall and droplets q''_{w-d} could be calculated by following equation,

$$q''_{w-d} = \frac{i_{v-d} V_d \rho_d \frac{\beta_1}{\beta_2} \varepsilon}{2} \tag{3.23}$$

where, V_d is the droplet deposition velocity. The model for calculating effectiveness ε used in the current work was developed by Kendall and Rohsenow (1978), and β_1 and β_2 are two coefficients accounting for the effect of superheat on the vapor temperature profile, which are included in this model. A summary of equations used in this model is listed as below,

$$\varepsilon = 2.6 \left(\frac{\rho_v}{\rho_d}\right)^{\frac{1}{2}} \left(\frac{\bar{R}}{d}\right)^{\frac{1}{8}} \left[\frac{\beta_2 k_v (T_w - T_s)}{i_{v-d}(\rho_v \sigma d)^{\frac{1}{2}}}\right]^{\frac{1}{2}} \left[I_2 \frac{\mu_v i_{v-d}}{\beta_2 k_v (T_w - T_s) + I_1}\right]^{-\frac{1}{4}} \tag{3.24}$$

$$I_1 = 0.225,\ I_2 = 1.5 \tag{3.25}$$

$$\bar{R} = \frac{R_{max} + 0.43d}{2} \tag{3.26}$$

$$\frac{R^2_{max}}{d^2} = \frac{2}{3}\left(1 + \frac{We_p}{12}\right)\cos^2\left[\frac{1}{3}\arccos\left(\frac{-1.225}{1 + \frac{We_p^{3/2}}{12}}\right)\right] \tag{3.27}$$

$$We_p \equiv \frac{\rho_d V_d^2 d}{\sigma} \tag{3.28}$$

$$\text{if} \quad We_p < 1.74 \quad \text{then} \quad R_{max} = 0.43d \tag{3.29}$$

$$\beta_1 \equiv \frac{1 + 0.43\frac{C_{p,v}(T_w - T_s)}{i_{v-d}}}{1 + 0.3\frac{C_{p,v}(T_w - T_s)}{i_{v-d}}} \tag{3.30}$$

$$\beta_2 \equiv \frac{1}{1 + 0.3\frac{C_{p,v}(T_w - T_s)}{i_{v-d}}} \tag{3.31}$$

$$\delta^4 = 0.45\pi \bar{R}^4 \left(\frac{1}{We_p}\right)^{1/2} \left[\frac{\beta_2 \mu_v k_v (T_w - T_s)}{i_{v-d} \rho_v \sigma d}\right] \left[I_2 + \frac{\beta_2 k_v (T_w - T_s)}{\mu_v i_{v-d}} I_1\right] \tag{3.32}$$

$$\frac{\delta_c}{D_T} = \frac{\beta_1}{Nu_{w-v}} \left[\frac{T_w - T_s}{T_w - T_v}\right] \tag{3.33}$$

Note that all above vapor properties are evaluated at the bulk vapor temperature T_{vb}. δ and δ_c are the wall-droplet separation distance and critical wall-droplet separation distance. If $\delta > \delta_c$, the wall-droplets contact heat transfer is excluded in the proposed model. ε is the heat transfer effectiveness. $\bar{R}$ is the average droplet extension radius. T_w is the wall inner surface temperature. R_{max} is the maximum droplet extension radius. We_p is a Weber number based on the droplet deposition velocity.

The droplet deposition velocity V_d can be represented in a dimensionless form of V^+, which is defined as,

$$V^+ = \frac{V_d}{u^*} \tag{3.34}$$

where, u^* is the shear velocity estimated from the single-phase turbulent relation as below,

$$u^* = U_v \sqrt{\frac{f}{2}} \tag{3.35}$$

With the friction factor f, calculated from

$$\frac{f}{2} = \frac{0.023}{Re_{vb}^{0.2}} \tag{3.36}$$

Liu and Ilori (1974) found the dimensionless droplet deposition velocity V^+ to be highly relevant with a dimensionless particle relaxation time, and for dispersed flow conditions, generally V^+ could be taken as constant at $V^+ = 0.15$. All the vapor properties are evaluated at the bulk vapor temperature. Thus, the calculation of droplet deposition velocity V_d becomes

$$V_d = \frac{0.023}{Re_{vb}^{0.1}} U_v \tag{3.37}$$

3.4. Vapor-droplets interfacial heat transfer

The interfacial heat transfer between vapor and droplets depends on the local vapor temperature and on the distance of the droplet from the heated wall. Therefore, the total interfacial heat transfer depends on the droplet concentration distributed over the cross-section of the tube, and also depends on the vapor temperature profile. This part of heat transfer gives the secondary largest contribution to the wall heat removal, and it affects the flow acceleration caused by the vapor quality increase. This part of heat transfer determines the thermal non-equilibrium degree in the post-dryout flow. Currently, the most common way of modelling this part of heat transfer in one-dimensional separated flow models is to assume that the droplet distribution over the cross-section is uniform, and the interfacial heat transfer coefficient can be calculated by using the well-known Ranz-Marshall correlation (Ranz et al., 1952) with the reference vapor at bulk vapor temperature. Moreover, a shielding factor f_s, correlated by Yuen and Chen (1978), can be applied if the effect of mass variation on the interfacial heat transfer is considered in the model.

However, many experiments argue against the uniform droplet concentration assumption. Hagiwara et al. (1980) measured the existence of droplet concentration profile in adiabatic tubes. Ganić and Rohsenow (1979) and Lee and Almenas (1982) studied the trajectories

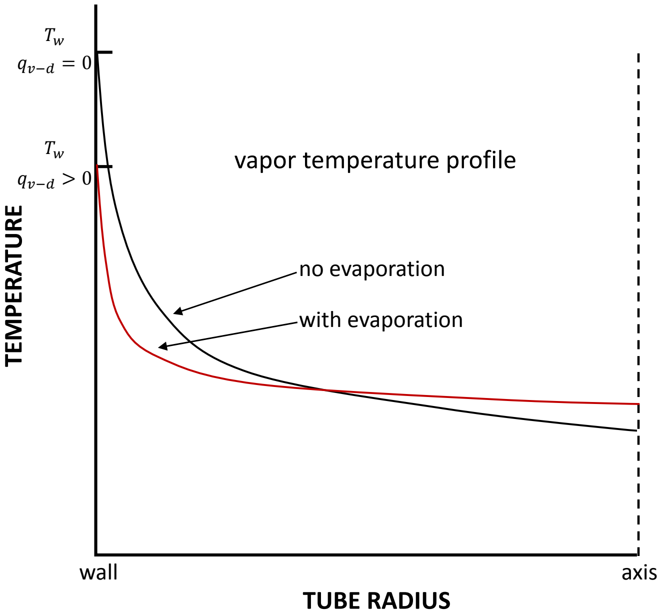

Figure 3.7.: Vapor radial temperature profile in post-dryout flow [source: (Varone, 1990)].

of droplets entering a thermal boundary layer. A major conclusion from these works is that most of the droplets are distributed in the turbulent core, and could arrive in the proximity of the wall only if they had acquired a substantial transversal velocity by some mechanisms.

Another argument against the usage of bulk vapor temperature as the reference vapor temperature can be concluded from the works of Hull (1982) and Varone (1990). Their research intended to determine if the presence of the evaporating droplets have an appreciable effect on the wall-vapor convective heat transfer coefficient, and to characterize the behavior of the wall-vapor Nusselt number with the presence of evaporating droplets. Their research results indicated that the presence of evaporating droplets could flatten the radial vapor temperature profile in the core as shown in Figure 3.7, and the evaporation rate is a function of the radial position that increasing rates of evaporation with tube radius due to the increasing vapor superheat. Since most droplets are distributed in the turbulent core according to the first argument for droplet concentration assumption, the usage of bulk vapor temperature as the reference vapor temperature in calculating the interfacial heat transfer rate could result in wrong estimation of the heat transfer coefficient.

These somewhat surprising characteristics of the hydrodynamic behavior of a cluster of droplets and the flattening of vapor radial temperature profile have to be taken into account in a mechanistic description of the phenomena, as they not only significantly simplify but also can improve the mathematical modelling. In one-dimensional separated flow models, consideration of the impact of the droplets' concentration distribution over the cross-section on the interfacial heat transfer between vapor and droplets is challenging. Rare attempts have included the above two arguments according to public records. Therefore, the theoretical modelling focuses on the analysis of parameters' influence on the thermal non-equilibrium, and the cross-section of the flow needs to be divided into a film region and a core region to account for the above two concerns.

3.4.1. Analysis of the wall temperature profile

In most of the experimental measurements, data points between the regions transition place and the following minimum local wall temperature place (if existing) are roughly located on a line with a linear relationship of wall temperature versus equilibrium quality. The slope of the wall temperature profile in the fully developed region is highly relevant to the evaporation of droplets. If some radial direction forces drive more droplets in the turbulent core into the near-wall region, where the vapor is highly superheated, more vapor would be generated, and the wall can be cooled better. As a result, the slope in the fully developed region develops to be more negative. The flow in such condition can be considered as more approaching thermal equilibrium flow. In general, for tests with same dryout quality, the test has a more negative slope of the wall temperature profile in the fully developed region can have a smaller non-equilibrium degree. Through the developing region determination method introduced in section 3.1.2, both the regions transition place and the following minimum local wall temperature place (if existing) can be determined. Then a straight line can be fitted in the fully developed region on the relationship of wall temperature versus equilibrium quality by using least-squares regression, as shown in Figure 3.8.

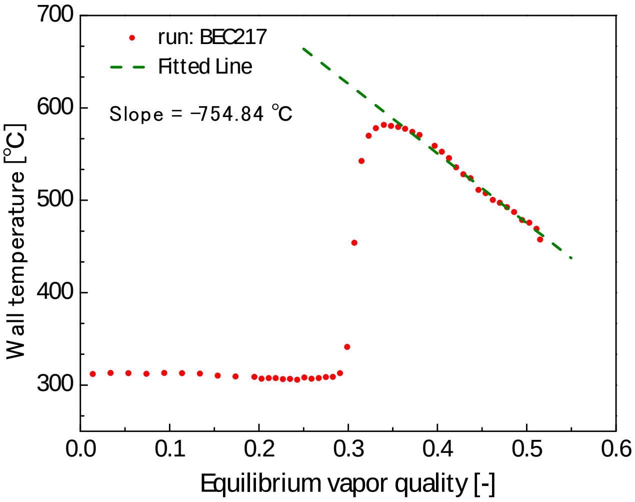

Figure 3.8.: Slope of wall temperature profile in the fully developed region.

Both the water based Becker experiment and the R-134a based KIT experiment are used to analyze the thermal non-equilibrium. All the utilized tests are selected with a criterion of dryout void fraction $\alpha_{do} > 0.8$ to ensure that most of the tests' conditions are in the post-dryout flow region. After having obtained the slope of the wall temperature profile in the fully developed post-dryout region, influences of parameters at dryout place on the slope of the wall temperature profile are studied. Re_{do}, x_{do}, and D_T/d_{do} are found to influence the slope greatly, as shown in Figure 3.9. Re_{do} is the vapor Reynolds number at dryout as defined in Eq. (3.11) with properties evaluated at the saturation temperature. x_{do} is the vapor quality at dryout and D_T/d_{do} is the diameter ratio of the tube to the droplet at dryout, and d_{do} is calculated by the method introduced in section 3.3.1.

Upstream of the dryout place, the continuous liquid phase depletes to a very thin film mainly by evaporation and entrainment, down to a critical thickness, where the dryout occurs. In the developing post-dryout region, droplets near the wall are fast evaporated since the near-wall droplets have a larger possibility to impinge the wall, and the near-wall vapor temperature also grows fast into superheated state. In the fully developed post-dryout region, most of the droplets are dispersed in the core region of the flow, and could be driven into the near-wall region (also named *film region* in the current work) by the interfacial forces in the radial direction (e.g. lift force, evaporation force and turbulent dispersion force). Since the vapor temperature in the film region is superheated, the droplets' evaporation in this region could be intensive. On the other hand, though most

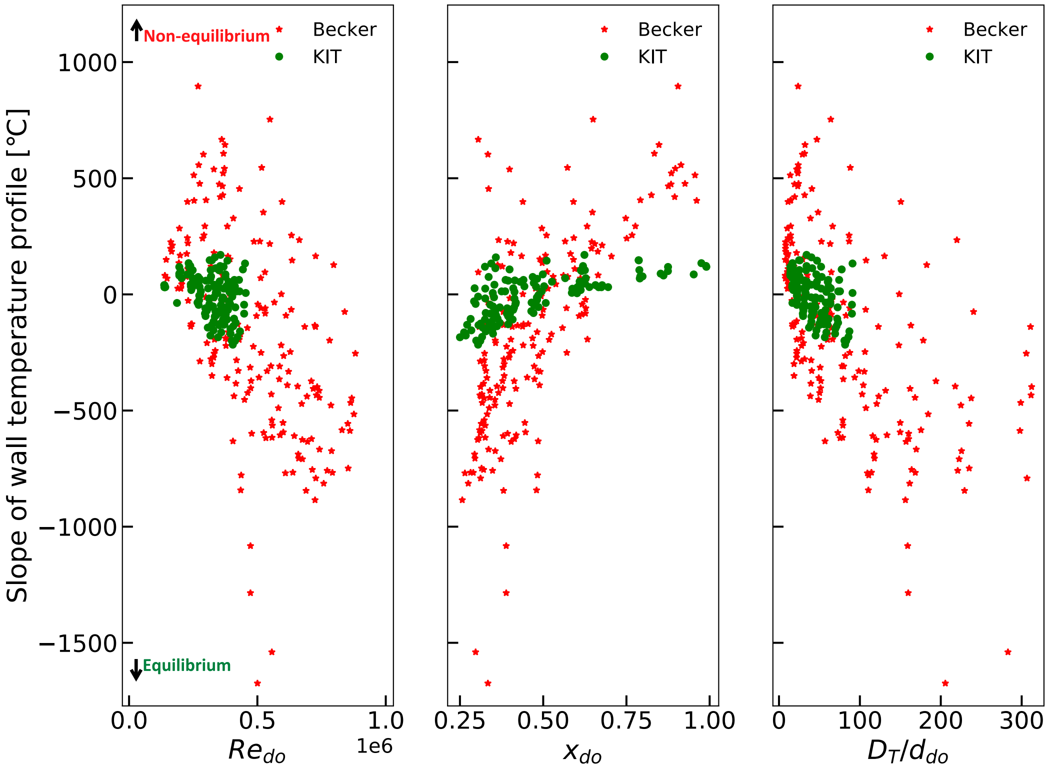

Figure 3.9.: Influences of $Re_{do}, x_{do}, D_T/d_{do}$ on the slope of wall temperature profile in the fully developed region.

droplets are in the core region of the flow, the vapor temperature in this region is just slightly higher than the droplet temperature. Thus the heat transfer rate between vapor and droplets in the core region can be small.

From the view of force balance, the droplets' movements are controlled by the interfacial forces. The drag force exerted on the droplets by the vapor is consistent with the motion of a droplet in the vapor, and it is the primary driver to accelerate the droplets. The droplets' concentration profile distributed over the cross-section of the flow is influenced by the radial direction forces, including mainly lift force, evaporation force (or thrust force), turbulent dispersion force, and virtual mass force.

The lift force refers to the shear-induced lift force acting on a dispersed phase in the presence of a rotational continuous phase. This force is proportional to the continuous phase shear rate. Though the development for the lift force model in droplet dispersed flow is not well established (McLaughlin, 1993; Sugioka and Komori, 2007), this force plays an important role and has a significant effect on the radial distribution of droplets according to the views of Legendre and Magnaudet (1998).

The asymmetrical evaporation around a droplet causes an evaporation force. The force acts perpendicular to the direction of the flow and always tends to push away the droplet towards the core region of the flow. As shown in Figure 3.9, with D_T/d_{do} increasing, the droplet is getting relatively smaller, the asymmetrical evaporation effect is less significant. Thus, more droplets would be driven towards the film region. Moreover, droplets with a smaller diameter can achieve a better interfacial heat transfer between vapor and droplets, and a more negative slope of wall temperature profile can be achieved in the fully developed post-dryout region.

The turbulent dispersion force results in the dispersed phase to be transported from regions of high volumetric concentration to regions of low volumetric concentration due to turbulent fluctuations, caused by the combined action of turbulent eddies and interphase drag (Burns et al., 2004). According to the above argument for droplets concentration profile over the cross-section, most of the droplets are in the core region of the flow. Thus, the turbulent dispersion force always tends to push the droplets towards the wall. As shown in Figure 3.9, an increase of Re_{do} can cause an increase of turbulence, and a decrease of x_{do} can cause an increase of droplets quality difference between the core region and the film region of the flow. Both effects result in a more significant turbulent dispersion force, and more droplets are pushed away into the film region, finally resulting in a more negative slope of the wall temperature profile in the fully developed region. Generally speaking, this force can be significant, while the density of vapor is close to the density of droplet or the size of the droplet is small. Thus, for high pressure condition, the thermal non-equilibrium degree is usually small.

Usually, the virtual mass force is negligible in droplet dispersed flow since the density of the carried vapor is too small, compared to the density of droplets. Thus, this force does not have much influence on the droplets (Paladino and Maliska, 2004). In general, the decrease of x_{do} means more droplets in the fully developed post-dryout region. Then more droplets would arrive at the hot film region, finally resulting in a more negative slope of the wall temperature profile.

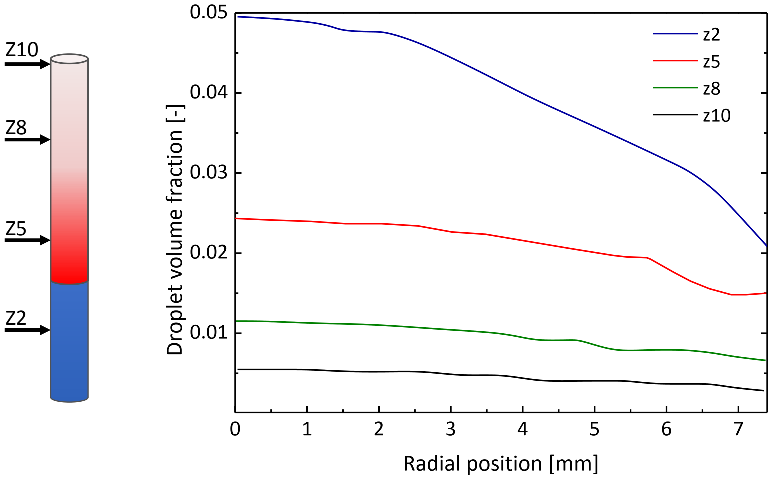

Figure 3.10.: Droplet concentration profiles at different locations for Becker test 271 [source: (Li and Anglart, 2016)].

The droplets concentration distribution over the cross-section is suitable to be investigated through CFD approach by considering the above-discussed forces that exert on droplets, though some of the mechanisms related to these forces are not well established. Since post-dryout heat transfer, especially the distribution of droplets in the flow, are highly history-dependent phenomena, the simulation on these phenomena better starts from the pre-dryout region. One of such works was implemented by Li and Anglart (2016), which is summarized in paragraph 2.2.3. Figure 3.10 shows the droplet volume fraction distribution over the cross-section at different elevations of the tube. The result shows that the droplet volume fraction generally decreases in the bulk flow due to the overall interaction of droplet evaporation, deposition, and entrainment. At all elevations, most of the droplets are in the core region, and the volume faction decreases along with the increasing radial position. This result confirms the assumption adopted in the current work, that most of the droplets are in the turbulent core region and can be driven into the film region while they had acquired a substantial transversal velocity by some mechanisms.

3.4.2. Cross-sectional region division

Based on the above discussions, the concentration of droplets affects the interfacial heat transfer significantly, and understanding of the trajectories of the droplets is crucially essential for predicting the non-equilibrium. For modelling these impacts on the interfacial heat transfer between wall and vapor due to the droplets' concentration profile, the cross-section of the flow is divided into a *core region* and a *film region*, as shown in Figure 3.11.

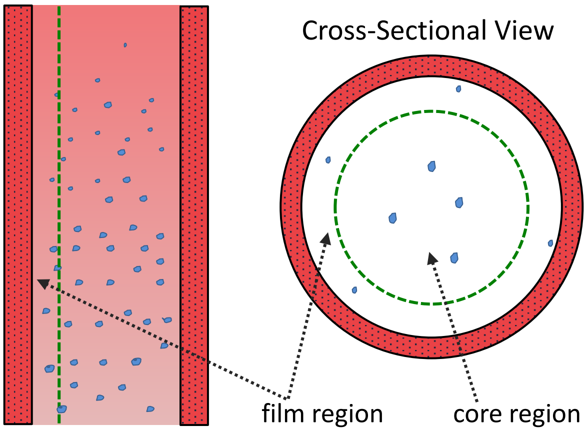

Figure 3.11.: Sketch of the film region and core region.

In the current work, droplets can be driven from the core region into the film region by some forces in the radial direction. Unlike the usual uniform droplets concentration assumption, the initial droplets at dryout are assumed to be totally in the core region. The core and film regions are characterized with two vapor temperatures T_{vc} and T_{vf}, respectively, which are defined as below,

$$T_{vc} = \frac{T_s + T_{vb}}{2} \tag{3.38a}$$

$$T_{vf} = \frac{T_w + T_{vb}}{2} \tag{3.38b}$$

where, T_s, T_w, and T_{vb} are the saturation, wall, and bulk vapor temperatures, respectively.

3.4.3. Interfacial heat transfer coefficient

Usually, the interfacial heat transfer coefficient is predicted by the well-known Ranz-Marshall correlation (Ranz et al., 1952). However, the application range of the Reynolds number is limited to be less than 200. Hughmark (1967) extended the Ranz-Marshall correlation, such that it can be applied to a wider range of Reynolds numbers. The correlation should not be used outside the recommended Prandtl number range. A shielding factor f_s correlated by Yuen and Chen (1978) is applied in the current work to consider the mass variation effect on the interfacial heat transfer. Finally, the correlation is expressed as follows,

If $0 \leq Re_d < 776.06$ and $0 \leq Pr_v < 250$,

$$h_{v-d} = f_s \frac{k_v}{d} \left(2 + 0.6 Re_d^{0.5} Pr_v^{0.33}\right) \tag{3.39a}$$

If $Re_d \geq 776.06$ and $0 \leq Pr_v < 250$,

$$h_{v-d} = f_s \frac{k_v}{d} \left(2 + 0.27 Re_d^{0.62} Pr_v^{0.33}\right) \tag{3.39b}$$

where, Re_d is the droplet Reynolds number defined in Eq. (3.4), and the shielding factor f_s is calculated through equation,

$$f_s = \frac{1}{\left[1 + \frac{C_{p,v}(T_v - T_s)}{i_{v-d}}\right]} \tag{3.40}$$

Interfacial heat transfer coefficients in the core region $h_{v-d,vc}$ and in the film region $h_{v-d,vf}$ are calculated separately by using the above equations with vapor properties evaluated at the vapor temperatures in its corresponding regions.

The total interfacial heat transfer is considered as a combined contribution of the interfacial heat transfer in the core and film regions. Therefore, a weighting factor K_2 is proposed in this study, representing the ratio of droplet evaporation happening in the film region to the total, and its value plays a most important role in the determination of the non-equilibrium of the flow. The modelling of factor K_2 is mainly based on the analysis in section 3.4.1, in which influence of variables on the slope of the wall temperature profile has been investigated and explained through the view of force balance. The overall transferred interfacial heat flux q''_{v-d} can be expressed as follows:

$$q''_{v-d} = (1 - K_2) h_{v-d,vc}(T_{vc} - T_s) + K_2 h_{v-d,vf}(T_{vf} - T_s) \tag{3.41}$$

where, K_2 is bounded in the range of [0 , 1],

$$K_2 = 4500 \alpha_v^2 \left(\frac{Re_d}{Re_{vb}}\right)^{1.5} \left(\frac{D_T}{d}\right) (x_e - x_{do})^2 \tag{3.42}$$

K_2 models the impacts of droplets' concentration on the interfacial heat transfer. Its value reflects the effects on the droplets' movements that are caused by the above discussed three radial direction forces. α_v is the void fraction. Re_d is the droplet Reynolds number, which includes the axial velocity difference between vapor and droplets. It also reflects the relative velocity in the transverse direction. The droplets movement in transverse direction caused by turbulent dispersion force is proportional to the transverse drag, which is relevant with the transverse velocity difference. Thus K_2 is proportional to Re_d. Re_{vb} reflects the turbulent intensity, though this term is positively relevant with the turbulent dispersion force. It also positively relates to the transverse lift force, which pulls droplets from the film region into the core region. Thus, ratio $\frac{Re_d}{Re_{vb}}$ is used in the correlation. The term $\frac{D_T}{d}$ is proportional to the evaporation force as discussed in section 3.4.1. As the assumption adopted in the current work is that most of the droplets are in the turbulent core region, the droplets can be driven into the film region while they had acquired a substantial transversal velocity by some mechanisms. It is considered to have no droplets in the film region at dryout, and more droplets would be driven into the film region while the place is further downstream from the dryout, since the movement caused by the transverse forces is a time-dependent phenomenon. Therefore, the term $x_e - x_{do}$ is used in the correlation. The constant exponents and coefficient in the correlation of K_2 are determined by comparison of the predicted wall superheat profiles in the fully developed post-dryout region with experiments, which will be shown in chapter 4. The proposed model, in general, can predict the wall superheat profiles very well under different flow conditions.

3.4.4. Conclusion and discussion

Interfacial heat transfer between vapor and droplets highly depends on the local vapor temperature and on the distance of the droplet from the heated wall. In post-dryout flow, most of the droplets are in the core region and can arrive in the film region if they had acquired a substantial transversal velocity by some forces. The droplets' movement in the radial direction is influenced mainly by the lift force, evaporation force, and turbulent dispersion force. Both the discussion of two arguments based on others' experimental researches, and the analysis of the thermal non-equilibrium degree based on the slope of wall temperature profile, directly or indirectly confirmed the impacts of droplets concentration on the interfacial heat transfer. It is necessary to include these impacts since the interfacial heat transfer gives the secondary largest contribution to the wall heat removal.

Therefore, the cross-section of the flow is divided into a core region and a film region with two different characteristic temperatures, respectively. The division of the cross-section of the flow makes it possible to account for the impacts of droplets' concentration on the interfacial heat transfer in one-dimensional separated flow models. Then, based on the investigation of influences of the parameters on the slope of the wall temperature profile in the fully developed post-dryout region, a weighting factor K_2 is proposed as shown in Eq. (3.42), reflecting effects on the droplets' trajectories caused by the lift force, evaporation force, and turbulent dispersion force.

3.5. Energy balance calculation

The energy balance is applied in the calculation of actual vapor quality, bulk vapor temperature, and wall temperature.

calculation of droplet size

The droplet size is uniformly decreasing along with the flow by evaporation caused by the interfacial heat transfer between vapor and droplets and the direct contact heat transfer between wall and droplets, which can be calculated as below,

$$\frac{\mathrm{d}d}{\mathrm{d}Z} = -2\left[\frac{q''_{v-d}}{U_d \rho_d i_{v-d}} + \frac{1}{3}\frac{d}{D_T}\frac{V_d}{U_d}\varepsilon\right] \tag{3.43}$$

where, d is the droplet diameter, Z is the distance from dryout in the axial direction, and U_d is the droplet axial velocity.

calculation of actual vapor quality

Through the liquid mass balance, Eq. (3.15) is obtained. The actual vapor quality can be calculated as below,

$$x_a = 1 - (1 - x_{do})\left(\frac{d}{d_{do}}\right)^3 \tag{3.44}$$

calculation of bulk vapor temperature

With assuming constant $C_{p,vb}$, an overall equilibrium energy balance can be obtained,

$$x_e - x_{do} = \frac{4q''_w}{G i_{v-d}}\frac{Z}{D_T} \tag{3.45}$$

Through the non-equilibrium vapor energy balance, the remaining heat, which is not used to evaporate droplets, would heat up the vapor, and the equation is expressed as below,

$$G x_a (i_{vb} - i_{vs}) = 4q''_w \frac{Z}{D_T} - G i_{v-d}(x_a - x_{do}) \tag{3.46}$$

where, i_{vb} is the specific enthalpy of the bulk vapor, and i_{vs} is the specific enthalpy of the saturated vapor. Combining Eq. (3.45) and Eq. (3.46), the vapor temperature can be calculated as below,

$$C_{p,vb}(T_{vb} - T_s) \approx (i_{vb} - i_{vs}) = \frac{x_e - x_a}{x_a} i_{v-d} \tag{3.47}$$

Herein, $C_{p,vb}$ is the specific heat capacity of the bulk vapor, and T_{vb} is the bulk vapor temperature.

calculation of wall temperature

In order to calculate the wall temperature, the overall energy balance on the wall is expressed as below,

$$q_w^{''} = \alpha_v q_{w-v}^{''} + (1 - \alpha_v) q_{w-d}^{''} \tag{3.48}$$

where, $q_w^{''}$ is the total heat flux on the wall. The wall-droplets contact area is treated by using the droplet volumetric fraction $(1 - \alpha_v)$. Combining the equations for $q_{w-v}^{''}$ in Eq. (3.12b) and $q_{w-d}^{''}$ in Eq. (3.23), the wall inner surface temperature T_w can be calculated as below,

$$T_w - T_{vb} = \frac{q_w^{''}}{\alpha_v h_{w-v}} - \frac{(1 - \alpha_v) i_{v-d} V_d \rho_d \frac{\beta_1}{\beta_2} \varepsilon}{2 \alpha_v h_{w-v}} \tag{3.49}$$

3.6. Programming flow diagram

The computing program begins at dryout and marches stepwise downstream to calculate the axial temperature profile. Input conditions are the mass flux G, wall heat flux $q_w^{''}$, tube diameter D_T, dryout quality x_{do}, pressure P, and the type of the fluid. It has been assumed that post-dryout heat transfer occurs while void fraction at dryout $\alpha_{do} > 0.8$.

After input of the required information, the droplets model can give the void fraction and the initial droplet average diameter at dryout. If the dryout void fraction α_{do} is less than 0.8, the flow is not considered as a post-dryout flow; then the calculation terminates. If the dryout void fraction is satisfied with the criterion, the fully developed convective heat transfer coefficient $h_{w-v,fdev}$ between wall and vapor is calculated by Eq. (3.10), as well as the nucleate boiling heat transfer coefficient at dryout $h_{w-v,NB}$. The convective heat transfer coefficient in the whole post-dryout region h_{w-v} is regarded as a combination of convective heat transfer coefficient for fully developed post-dryout flow $h_{w-v,fdev}$ and convective heat transfer coefficient at dryout $h_{w-v,NB}$ calculated by Eq. (3.12). To accomplish the calculation of h_{w-v}, the weighting factor K_1 needs to be calculated in advance by Eq. (3.13). The required variable L_{dev} in Eq. (3.13) can be calculated by the proposed developing region length correlation, as shown in Eq. (3.5).

Then, the wall-droplet contact heat transfer coefficient h_{w-d} is continuously computed by the models, which are introduced in chapter 3.3.2. As for the computing of interfacial heat transfer coefficient between vapor and droplets h_{v-d}, heat transfer coefficients in the film region and the core region are firstly calculated separately and irrelevantly, and then the weighting factor K_2 is calculated by Eq. (3.42). Thus, h_{v-d} can be obtained.

While the convective heat transfer coefficient between wall and vapor h_{w-v}, contact heat transfer coefficient between wall and droplets h_{w-d}, and interfacial heat transfer coefficient between vapor and droplets h_{v-d} are obtained, the energy balance equations introduced in chapter 3.5 can be applied to calculate the actual vapor quality, bulk vapor temperature, and wall temperature. If these three variables in the whole post-dryout region are not converged, then new values are assigned for these three variables, the iteration starts again from the calculating of three heat transfer coefficients h_{w-v}, h_{w-d}, and h_{v-d} until the convergence criterion is satisfied, then computing is accomplished and ended.

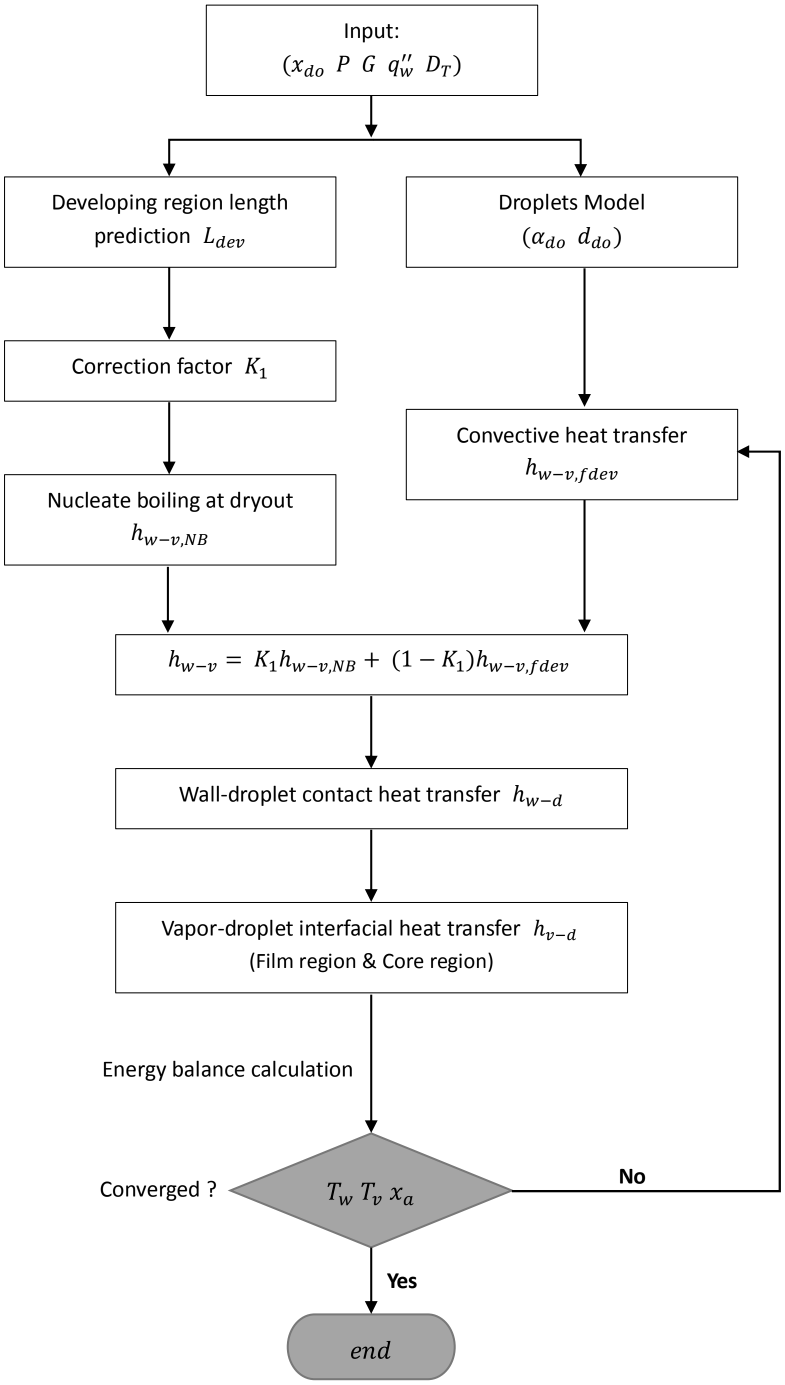

Figure 3.12.: Flow diagram of computing program.

3.7. Conclusion

In this chapter, a general model for full-range post-dryout heat transfer in vertical tubes has been introduced in detail. The most important original works are in two aspects: the determination of a developing post-dryout region and the calculation of interfacial heat transfer between vapor and droplets. Main works and conclusions are summarized here:

developing post-dryout region determination

Due to the different flow patterns in the developing and fully developed post-dryout regions, it is necessary to distinguish these two regions in the model. Original works include,

- Definition of terms *developing post-dryout region* and *fully developed post-dryout region* is proposed to describe and distinguish these two regions.
- A method through using the wall temperature slope is applied on both Becker and the KIT experiments to determine L_{dev}. This method is limited to the experiment databank itself and cannot be applied while the data points are too sparse. However, this method works well with the utilized two experiments.
- Influences of parameters on L_{dev} are analyzed. Reynolds number Re and the Boiling number Bo are found to be strongly associated with L_{dev} in a similar way in both experiments, respectively.
- A general correlation for L_{dev} is derived by regression analysis, as shown in Eq. (3.5). The correlation can provide a good prediction of the developing region length.

interfacial heat transfer prediction

Despite that most of the one-dimensional separated flow models assume that the droplets' concentration distribution over the cross-section of the flow is uniform, and the bulk vapor temperature is used as a reference temperature in the prediction of interfacial heat transfer between vapor and droplets. Many authors confirmed the non-uniform concentration profile of droplets, and the presence of droplets can flatten the radial vapor temperature profile. It is necessary to account for these somewhat surprising characteristics of the hydrodynamic behavior of a cluster of droplets and the flattening of the vapor radial temperature profile, as these kinds of considerations not only significantly simplify but also can improve the mathematical modelling.

Based on the above conclusions, works are implemented as following,

- Analysis of the thermal non-equilibrium degree is implemented based on the slope of the wall temperature profile. Influences of Re_{do}, x_{do} and D_T/d_{do} on the slope of the wall temperature profile in the fully developed region are explained through the view of force balance.
- The cross-section of the flow is divided into a core region and a film region with two different characteristic temperatures T_{vc} and T_{vf}, respectively.
- A weighting factor K_2, which reflects the effects on droplets' movements caused by the lift force, evaporation force, and turbulent dispersion force, is proposed as shown in Eq. (3.42).

Besides, some original works are implemented in the aspects of modelling of convective heat transfer between wall and vapor, which includes,

- The Forslund correlation is modified to account for the large fluid property variations across the tube, as shown in Eq. (3.10).
- The convective heat transfer coefficient in the whole post-dryout region is regarded as a combination of the convective heat transfer coefficient in the fully developed post-dryout region $h_{w-v,fdev}$ and the heat transfer coefficient at dryout $h_{w-v,NB}$. A weighting factor K_1 is developed, which represents the ratio of heat transfer rate at dryout to the heat transfer rate between wall and vapor, as shown in Eq. (3.13).

4. Assessment of the proposed model

A general theoretical model for post-dryout heat transfer was introduced in the last chapter. Therefore, in this chapter, the proposed model is first assessed by comparing with four widely used models and two experiments with uniform axial heat flux, including experiments Becker (Becker et al., 1983) and KIT (Köckert et al., 2018). Further, the proposed model is compared with some other models and experimental data from the literature on the predictions of wall and vapor temperatures. The contribution of direct contact heat transfer in post-dryout flow is also analyzed under different flow conditions. Moreover, the proposed model is assessed by using an experiment with non-uniform axial heat flux conducted by Becker et al. (1992), which is commonly named BeckerII in the current work.

4.1. Parameters of Becker and KIT experiments

Becker experiment (Becker et al., 1983) was carried out at KTH in a vertically oriented, electrically, and uniformly heated tube with an upward flow of water. In total, 3944 data points were obtained in the whole post-dryout region with a selection criterion of dryout void fraction $\alpha_{do} > 0.8$. Becker experiment covers the following ranges of parameters:

Fluid: $water$
Heated length: $7000\ mm$
Inner diameter: $14.90,\ 10.00,\ and\ 24.69\ mm$
Inlet subcooling: $\sim 10\ ^{\circ}\mathrm{C}$
Pressure: $3 - 20.5\ MPa$
Mass flux: $500 - 3000\ kg/(m^2\ s)$
Heat flux (uniform): $90 - 1250\ kW/m^2$
Steam quality (equilibrium): $0.03 - 1.66$

The KIT experiment (Köckert et al., 2018) was performed at the KIT Model Fluid Facility (KIMOF). The refrigerant R-134a is used in a vertical round tube with a upward flow. The tube is heated uniformly with an inside diameter of 10 mm and a heated length of 3100 mm. In total, 2375 data points were obtained in the whole post-dryout region with a selection criterion of dryout void fraction $\alpha_{do} > 0.8$. The KIT experiment covers the following ranges of parameters:

Fluid: *R-134a*
Heated length: $3100\ mm$
Inner diameter: $10.00\ mm$
Inlet subcooling: $\sim 10\ °C$
Pressure: $1.1,\ 1.6,\ and\, 2.8\ MPa$
Mass flux: $300 - 1500\ kg/(m^2\ s)$
Heat flux (uniform): $20 - 140\ kW/m^2$
Steam quality (equilibrium): $0.15 - 1.76$

4.2. Comparisons of heat transfer coefficients

For a general assessment of the prediction accuracy of the proposed model, the heat transfer coefficients are compared between the proposed model and the experiments. All data are selected with a criterion of dryout void fraction $\alpha_{do} > 0.8$ to ensure most of the conditions are in the post-dryout region, though the proposed model can predict a wider range. Then there are 3944 data points in Becker experiment and 2375 data points in the KIT experiment selected. The heat transfer coefficient (HTC) is defined as below,

$$h = \frac{q_w^{''}}{T_w - T_s} \tag{4.1}$$

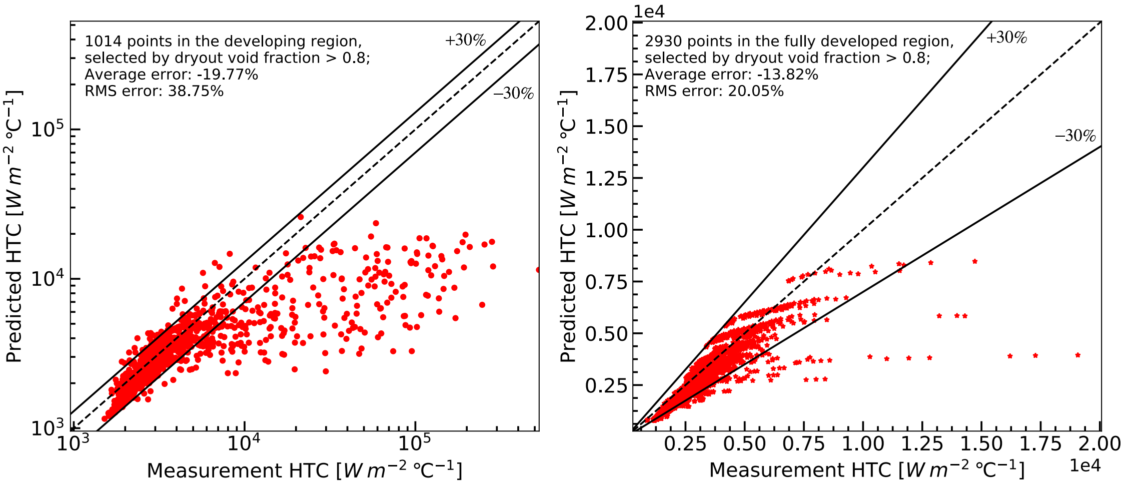

Figure 4.1.: HTC comparisons with the water based Becker experiment, (a) in the developing post-dryout region, (b) in the fully developed region.

Figure 4.1 compares the predicted HTC with the measured ones in the water based Becker experiment. 1014 points in the developing post-dryout region are compared. The results show that, on the average, the proposed model underestimates the experimental HTC by 19.77% with an RMS error of 38.75%. On the other hand, 2930 points in the fully developed post-dryout region are compared. The results show that, on the average, the proposed model underestimates the experimental HTC by 13.82% with an RMS error of 20.05%. The error of the prediction is defined as the ratio of the difference between the predicted HTC and the measurement HTC to the measurement HTC.

Figure 4.2 compares the predicted HTC with the measured ones in the R-134a based KIT experiment. 555 points in the developing post-dryout region are compared. The results

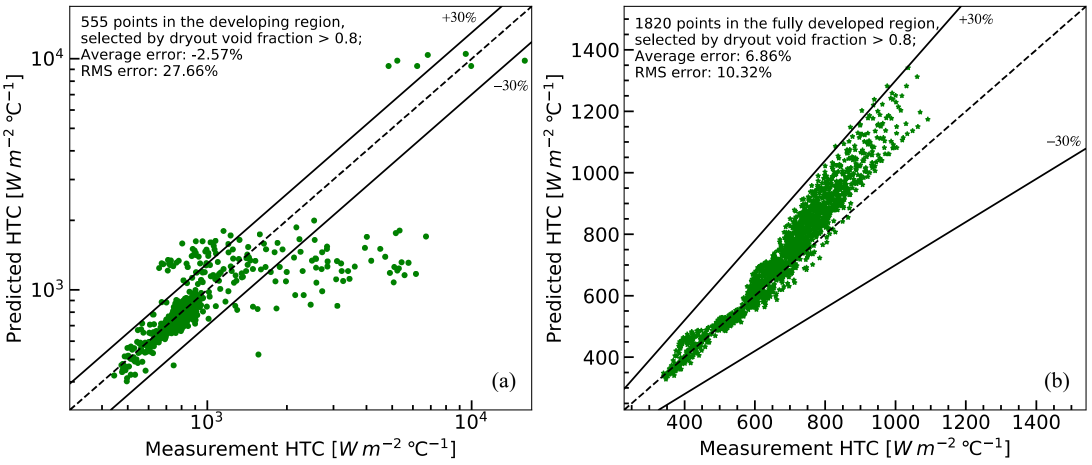

Figure 4.2.: HTC comparisons with the R-134a based KIT experiment, (a) in the developing post-dryout region, (b) in the fully developed region.

show that, on the average, the proposed model underestimates the experimental HTC by 2.57% with an RMS error of 27.66%. On the other hand, 1820 pints in the fully developed post-dryout region are compared. The results show that, on the average, the proposed model overestimates the experimental HTC by 6.86% with an RMS error of 10.32%. The error of the prediction is defined the same as that in comparison with Becker experiment.

Both Figures 4.1 and 4.2 show that the proposed model greatly underestimates the predictions of high HTC in the developing post-dryout region. For such high HTC, a rough estimation of the wall superheat can be calculated by Eq. (4.1). The intermediate heat flux and intermediate HTC for Becker experiment are 670 kW/m^2 and 40 $kW/(m^2\ °\mathrm{C})$, respectively. Meanwhile, the intermediate heat flux and intermediate HTC for the KIT experiment are 80 kW/m^2 and 3 $kW/(m^2\ °\mathrm{C})$, respectively. Therefore, the wall superheats at these high HTC conditions are around 20 °C. The locations of these conditions are just behind the dryout, where the measured wall temperature oscillates intensively. The wall is sometimes dry and sometimes wet. This temperature, however, is determined as a time-based average value. Wall superheat of two adjacent data points in this area can have a difference of more than 200 °C, which can be identified from the comparisons in section 4.3.1. Thus, the systematic error that produced in the experimental determination of dryout can lead to 90% underestimation of the HTC by the proposed model.

Table 4.1.: HTC prediction accuracy of CSO, GRO, LCS, ATHLET, and the proposed model compared with the water based Becker experiment.

	Developing region (1014 points)		Fully developed region (2930 points)		Whole region (3944 points)	
	average e [%]	RMS e [%]	average e [%]	RMS e [%]	average e [%]	RMS e [%]
CSO	-56.43	63.34	-11.32	46.43	-23.13	51.40
GRO	-9.79	48.31	82.44	112.95	58.31	100.16
LCS	-28.67	44.63	4.84	21.04	-3.89	29.09
ATHLET	106.54	154.72	191.00	209.40	168.91	196.57
Proposed model	-19.77	38.75	-13.82	20.05	-15.35	26.17

For the prediction of HTC, four widely used models (CSO, GRO, LCS, and ATHLET) are compared with the proposed model. In the whole comparisons in this chapter, the term ATHLET is used to represent the modified Dougall-Rohsenow correlation in the ATHLET code. Results of the HTC predictions compared with Becker experiment are listed in Table 4.1. The CSO model shows that HTC in both the developing region and the fully developed region are underestimated in general. The GRO model obviously underestimates HTC in the fully developed region. The LCS achieves comparable accuracy with the proposed model in both regions. The modified Dougall-Rohsenow correlation (Liesch et al., 1975) in the ATHLET code is used, and ATHLET always overestimates HTC in all regions since it does not account for the thermal non-equilibrium. Among all the models, the proposed model predicts the best in all regions by comparing the RMS error, and on average, the proposed model underestimates HTC in all the regions.

Table 4.2.: HTC prediction accuracy of CSO, GRO, LCS, ATHLET, and the proposed model compared with the R-134a based KIT experiment.

	Developing region (555 points)		Fully developed region (1820 points)		Whole region (2375 points)	
	average e [%]	RMS e [%]	average e [%]	RMS e [%]	average e [%]	RMS e [%]
CSO	-63.00	67.00	-18.11	41.96	-28.75	49.06
GRO	-23.95	35.28	29.70	41.97	16.99	40.48
LCS	5.28	35.30	56.42	59.37	44.30	54.64
ATHLET	103.82	134.76	148.72	155.51	138.08	150.85
Proposed model	-2.57	27.66	6.86	10.32	4.66	16.14

Results of the HTC predictions compared with the KIT experiment are listed in Table 4.2. The CSO model shows that HTC in both the developing region and the fully developed region are still underestimated in general. The GRO model and ATHLET show a similar predicting behavior while compared with Becker experiment. The LCS shows apparent overestimation of HTC in the fully developed region. This could be on one side due to the usage of Hadaller correlation (Hadaller and Banerjee, 1969) in the LCS for convection, which was developed only for steam, and is not compatible with R-134a. On the other side, this is due to an empirical correction factor R_{Nu} that multiplied with the convective heat transfer correlation, which improves the HTC prediction for water but over-predicts the HTC for R-134a significantly. Among all the models, the proposed model predicts the best in all the regions by comparing the RMS error of HTC. On average, the proposed model overestimates HTC in the fully developed post-dryout region.

4.3. Model's performance evaluation under different conditions

4.3.1. Model's performance under different pressures

Figures 4.3, 4.4, and 4.5 show the wall superheat predictions of the LCS and the proposed model under different pressures with intermediate mass fluxes. Both the water based Becker experiment and the R-134a based KIT experiment are compared with the LCS and the proposed model. The LCS is chosen to compare because it achieves comparable accuracy with the proposed model for predicting HTC. All the compared cases are selected with a criterion of dryout void fraction $\alpha_{do} > 0.8$.

For low pressure in water as shown in Figure 4.3 (a), the LCS predicts the wall temperature magnitude better than the proposed model, but the proposed model predicts the wall temperature profile better than the LCS. For intermediate pressure in water as shown in Figure 4.4 (a), both the LCS and the proposed model predict well the temperature magnitude, and the proposed model predicts the temperature profile better than the LCS.

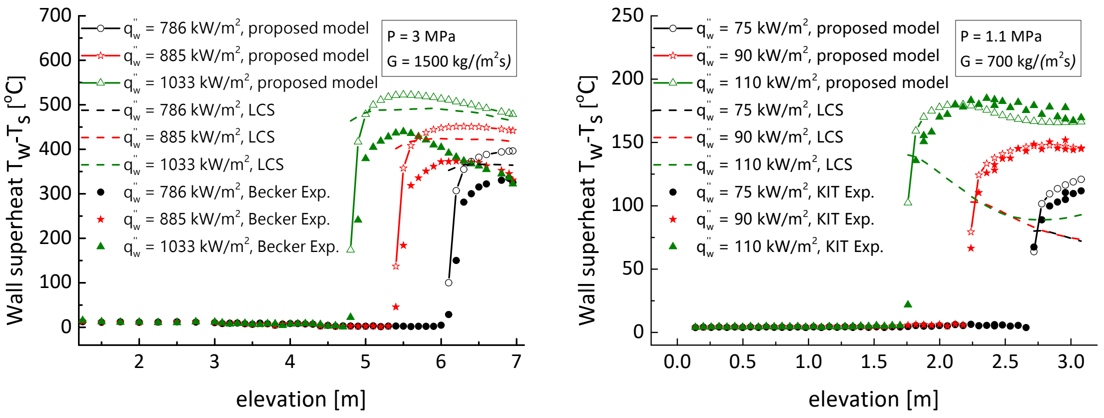

(a) low pressure in water, Becker (b) low pressure in R-134a, KIT

Figure 4.3.: Wall superheat comparisons between models (LCS, proposed model) and experiments (Becker, KIT) under conditions of intermediate mass flux and low pressures.

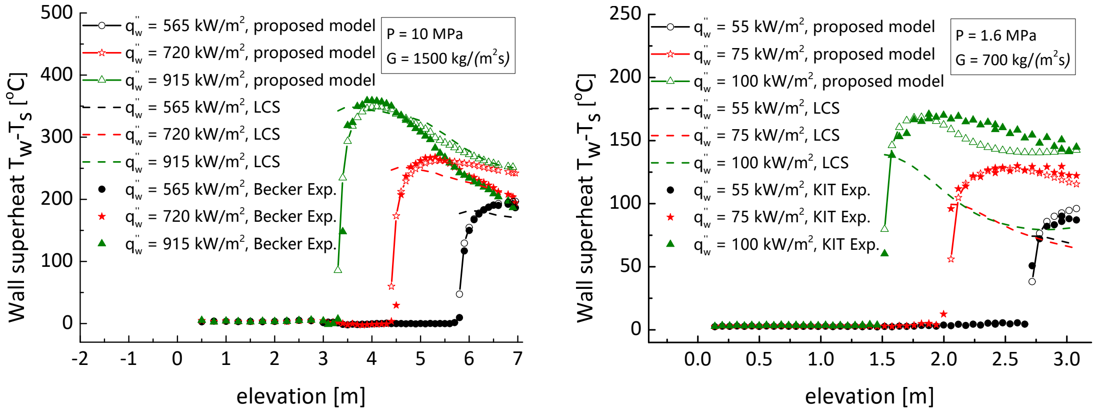

(a) intermediate pressure in water, Becker (b) intermediate pressure in R-134a, KIT

Figure 4.4.: Wall superheat comparisons between models (LCS, proposed model) and experiments (Becker, KIT) under conditions of intermediate mass flux and intermediate pressures.

For high pressure in water, as shown in Figure 4.5 (a), the proposed model predicts better than the LCS both the wall temperature magnitude and the wall temperature profile.

For all different pressures in R-134a, as shown in Figure 4.3 (b), Figure 4.4 (b), and Figure 4.5 (b), the proposed model predicts much better than the LCS both the wall temperature magnitude and the wall temperature profile. The LCS significantly over-predicts HTC in the R-134a flow condition, and the reasons for this overestimation are mentioned in chapter 4.2, which could be the incompatibility of the utilized Hadaller correlation or the overfitting of empirical correction factor R_{Nu} that multiplied on the convective heat transfer correlation.

In general, compared with Becker experiment, the proposed model predicts better at intermediate and high pressures than at low pressure. Compared with the KIT experiment, the proposed model predicts more or less the same accuracy under different pressures. Moreover, from the comparisons of the slope of the wall temperature profile in the fully developed region, the slopes in water and R-134a conditions are slightly overestimated and underestimated by the proposed model, respectively.

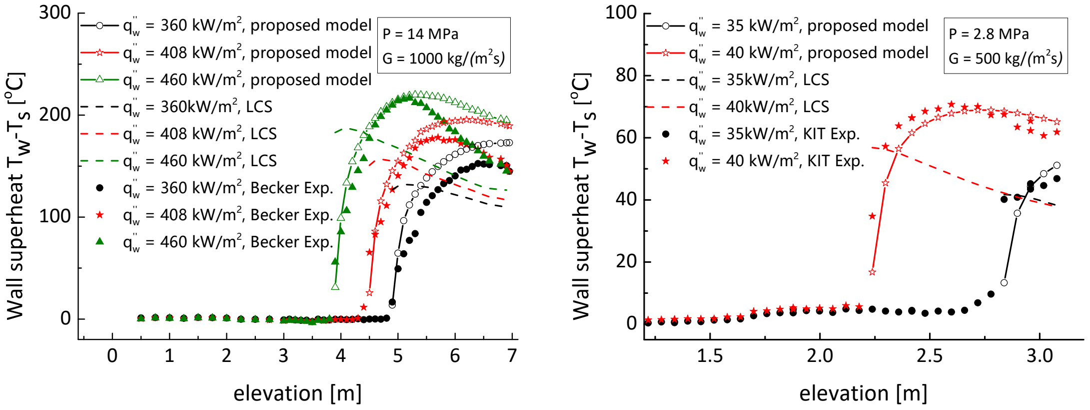

(a) high pressure in water, Becker

(b) high pressure in R-134a, KIT

Figure 4.5.: Wall superheat comparisons between models (LCS, proposed model) and experiments (Becker, KIT) under conditions of intermediate mass flux and high pressures.

4.3.2. Model's performance under different flow qualities

Wall temperature predictions of models (ATHLET, proposed model) are compared with experiments (Becker, Bennett, KIT, and Cumo) under different flow qualities. Table 4.3 summarized the parameters of compared tests. In some flow conditions with very high vapor quality, the droplets have only weak influences on the post-dryout heat transfer. Especially, while the thermal non-equilibrium is small, the flow can be considered as an equilibrium mixture convection with a primary contribution from the vapor. For such kind of conditions, many equilibrium correlations for post-dryout flow can predict very well, and one of the most representative correlations is the modified Dougall-Rohsenow, which is herein used in the ATHLET. For low flow quality conditions, the droplets not only can greatly impact on the convection but also influence the thermal non-equilibrium intensively. In these conditions, the accuracies of models differ.

Table 4.3.: Test parameters of experiments (Becker, Bennett, KIT, and Cumo) with different flow qualities.

	Pressure $[MPa]$	Tube diameter $[mm]$	Mass flux $[kg/(m^2s)]$	Heat flux $[kW/m^2]$	Dryout quality $[-]$
Becker, water	7.0	14.9	500	509	0.90
	7.0	14.9	3105	1212	0.32
Bennett, water	7.0	12.6	394	545	0.92
	7.0	12.6	3800	1700	0.30
KIT, R-134a	1.6	10.0	304	55	0.85
	1.6	10.0	1498	115	0.25
Cumo, R-12	2.0	4.75	840	104	0.45
	2.0	4.75	1200	100	0.30

Figure 4.6(a) shows the wall superheat comparisons between models (ATHLET, proposed model) and Becker experiment (Becker et al., 1983) under conditions of low and high flow qualities. While the flow quality is low as 0.32, the proposed model predicts very well the wall superheat magnitude and profiles. The ATHLET predicts nearly almost the constant wall superheat in the whole post-dryout region, and the wall superheat is highly underestimated. While the flow quality is very high as 0.90, the proposed model predicts

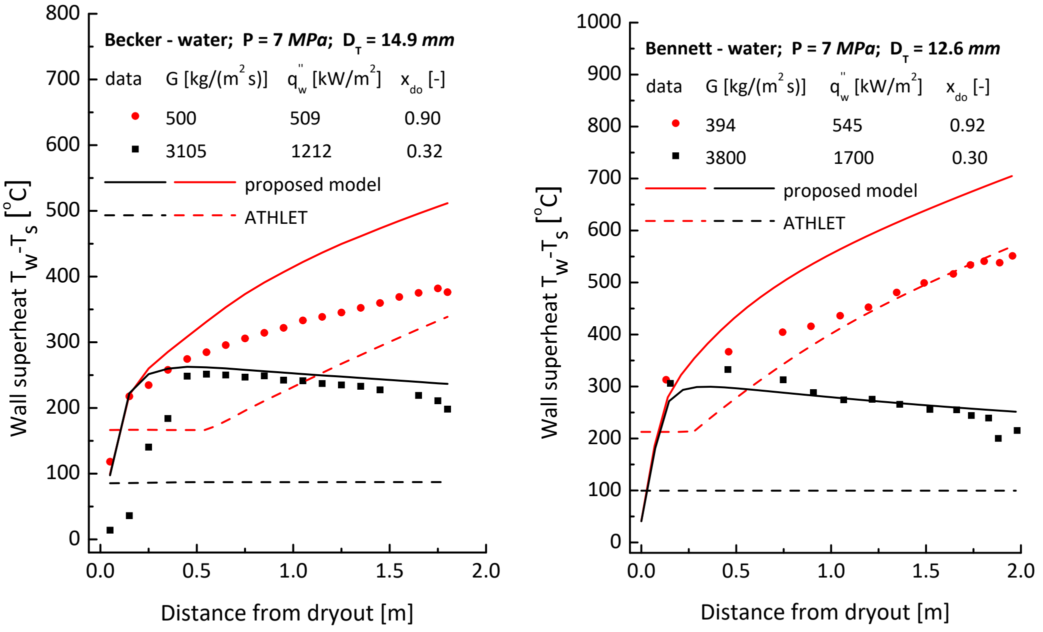

(a) Becker experiment (Becker et al., 1983) (b) Bennett experiment (Bennett et al., 1968)

Figure 4.6.: Wall superheat comparisons between models (ATHLET, proposed model) and water experiments with different flow qualities.

well in the developing post-dryout region and overestimates the wall superheat in the fully developed region. The proposed model predicts poorly, especially in the area when the equilibrium quality is greater than 1.0. On the contrary, the ATHLET predicts well in this region. The results can be explained that in the high actual quality flow, especially while the equilibrium quality is far greater than 1.0, the flow can be considered as a single-phase flow, and the ATHLET is equivalent to the Dittus-Boelter equation under such conditions. Thus the ATHLET performs very well under these conditions of very high quality flow. It can be concluded from these results that the modified Forslund correlation adopted in this proposed model underestimates the convective heat transfer coefficient in water with a very high quality flow.

Similar results are found in the wall superheat comparisons between models (ATHLET, proposed model) and Bennett experiment (Bennett et al., 1968), as shown in Figure 4.6(b). For very high quality flows, the wall superheat is overestimated by the proposed model, and the ATHLET performs very well in this comparison. For low quality flow, the proposed model predicts well the wall superheat magnitude and profiles in the whole region.

Figure 4.7 shows the wall superheat comparison between models (ATHLET, proposed model) and the KIT experiment (Köckert et al., 2018) in R-134a. While the flow quality is low as 0.25, the proposed model predicts good wall superheat profiles but underestimates the magnitude. The ATHLET predicts nearly a constant wall superheat in the whole post-dryout region, and the magnitude is highly underestimated. While the flow quality is very high as 0.85, the proposed model predicts well the wall superheat magnitude and profiles. The ATHLET predicts well the wall superheat profile in the fully developed region but predicts the magnitude badly, even in the area where the equilibrium quality exceeds 1.0. It can be concluded from these results that the modified Forslund correlation adopted in the proposed model predicts the wall-vapor convective heat transfer coefficient well in R-134a with a very high quality flow, but overestimates the convective heat transfer enhancement caused by the presence of droplets in R-134a with a low quality flow.

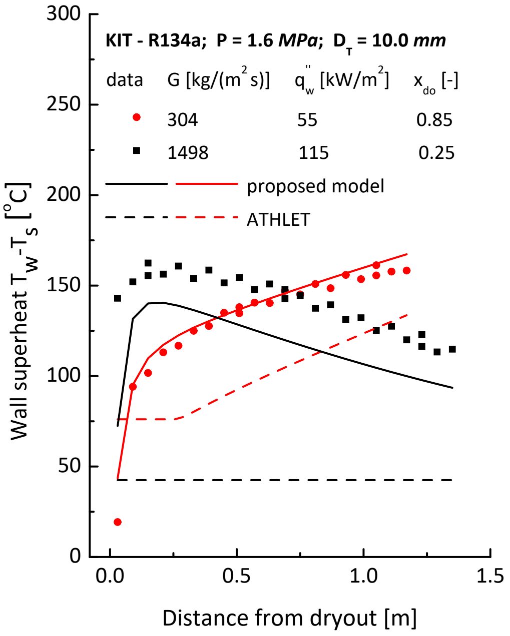

Figure 4.7.: Wall superheat comparisons between models (ATHLET, proposed model) and the KIT experiment (Köckert et al., 2018) with different flow qualities.

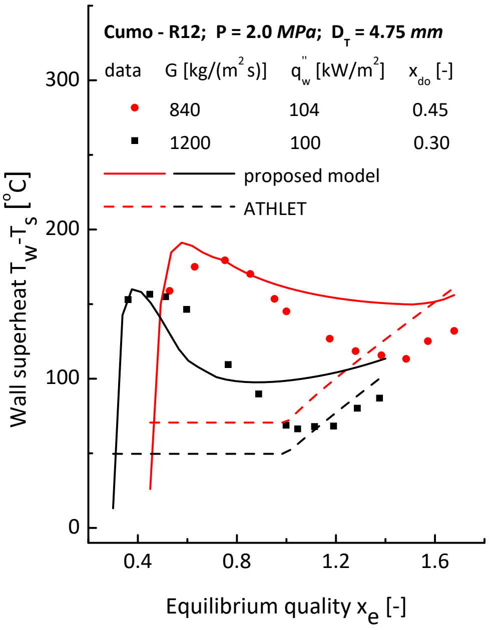

Figure 4.8.: Wall superheat comparisons between models (ATHLET, proposed model) and Cumo experiment (Cumo et al., 1974) with different flow qualities.

Figure 4.8 shows the wall superheat comparisons between models (ATHLET, proposed model) and the Cumo experiment (Cumo et al., 1974) in R-12. Though the two qualities are low, the ATHLET overestimates the wall superheat in the area where the equilibrium quality exceeds 1.0, and the proposed model only predicts the trend of wall superheat profile. The inaccuracies could be due to the small diameter of the tube. However, the proposed model also overestimates the wall-vapor convective heat transfer enhancement caused by the presence of droplets in the fully developed region of a very low quality flow. This is similar to the result found in comparison with the KIT experiment.

To sum up, for a high quality flow, the influences on the post-dryout heat transfer due to the presence of droplets are small, and for a low quality flow, the influences are significant. Based on the comparison of results, the proposed model is found to predict well the wall superheat profile. However, the model tends to overestimate the magnitude of the wall superheat for a high quality flow in water, and underestimates the magnitude of the wall superheat for a low quality flow in R-134a.

4.3.3. Model's performance under different thermal non-equilibrium

Table 4.4.: Test parameters of experiments (Becker, KIT) with different thermal non-equilibrium.

	Pressure $[MPa]$	Tube diameter $[mm]$	Mass flux $[kg/(m^2s)]$	Heat flux $[kW/m^2]$	Dryout quality $[-]$
Becker, water	3.0	14.9	500	570	0.825
	20.0	14.9	2600	600	0.372
KIT, R-134a	1.1	10.0	500	90	0.79
	2.8	10.0	1300	60	0.22

Under high pressure with high mass flux conditions, the vapor has a higher density and a larger turbulence intensity, which results in a small non-equilibrium degree. While under low pressure with low mass flux conditions, the vapor is significantly lighter than the droplets, and the turbulence intensity is small. This results in a high non-equilibrium degree. Table 4.4 summarized the parameters of the compared tests.

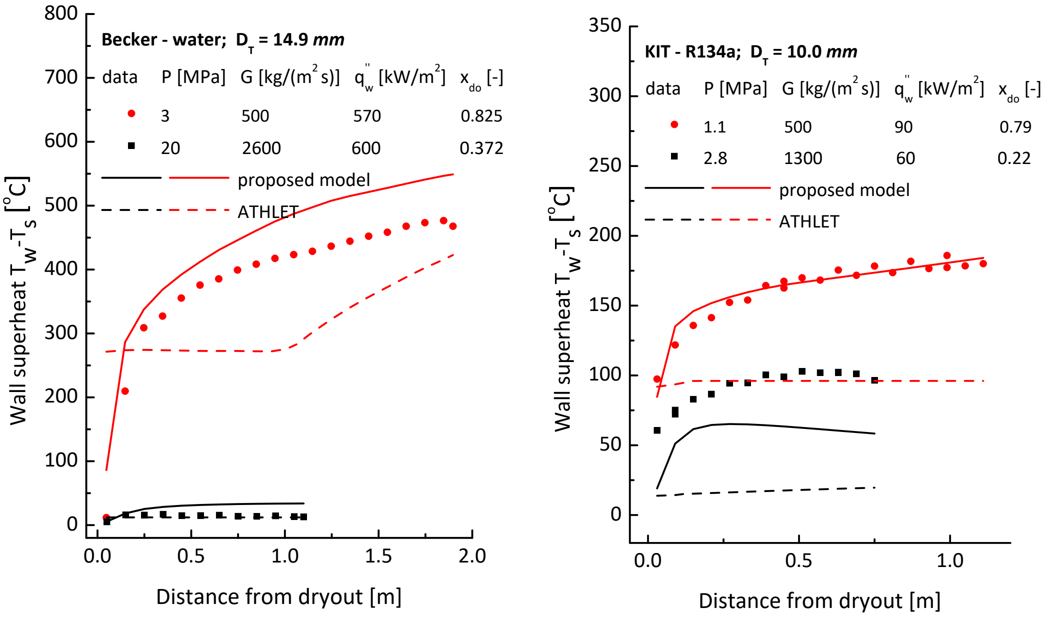

(a) Becker experiment (Becker et al., 1983)

(b) KIT experiment (Köckert et al., 2018)

Figure 4.9.: Wall superheat comparisons between models (ATHLET, proposed model) and experiments with different thermal non-equilibrium.

Figure 4.9(a) shows the wall superheat comparison between models (ATHLET, proposed model) and Becker experiment (Becker et al., 1983) in water. While the pressure is high as 20 MPa and the mass flux is high as 2600 $kg/(m^2s)$, the thermal non-equilibrium degree is small. The ATHLET can well predict the wall superheat in these conditions, and the proposed model overestimates the wall superheat. While the pressure is low as 3 MPa

and the mass flux is low as 500 $kg/(m^2s)$, the thermal non-equilibrium degree is large. The ATHLET obviously underestimates the wall superheat under these conditions, and the proposed model slightly overestimates the magnitude of the wall superheat, but well predicts the profiles.

Figure 4.9(b) shows the wall superheat comparisons between models (ATHLET, proposed model) and the KIT experiment (Köckert et al., 2018) in R-134a. While the pressure is 2.8 MPa and the mass flux is 1300 $kg/(m^2s)$, the thermal non-equilibrium degree could be small, though both the pressure and the mass flux are not high enough. The proposed model can well predict the wall superheat profiles but obviously underestimates the magnitude. The calculated dryout void fraction, in this case, is 0.57, not in the post-dryout region. However, the ATHLET is not suitable in this case since the pressure and mass flux are not high enough. There is still a weak thermal non-equilibrium, and the presence of droplets enhances the wall-vapor convection. While the pressure is low as 1.1 MPa and the mass flux is low as 500 $kg/(m^2s)$, the thermal non-equilibrium is strong. The ATHLET obviously underestimates the wall superheat under these conditions, and the proposed model excellently predicts both the magnitude and the profiles of the wall superheat.

4.3.4. Influence of tube diameters on the model's performance

Table 4.5.: Test parameters of water experiments with different tube diameters.

	Tube diameter [mm]	Pressure [MPa]	Mass flux [$kg/(m^2s)$]	Heat flux [kW/m^2]	Dryout quality [$-$]
Era, 6mm	6.0	7.0	2200	1000	0.48
Becker, 10mm	10.0	7.0	2000	791	0.452
Becker, 14.9mm	14.9	7.0	2000	1050	0.4

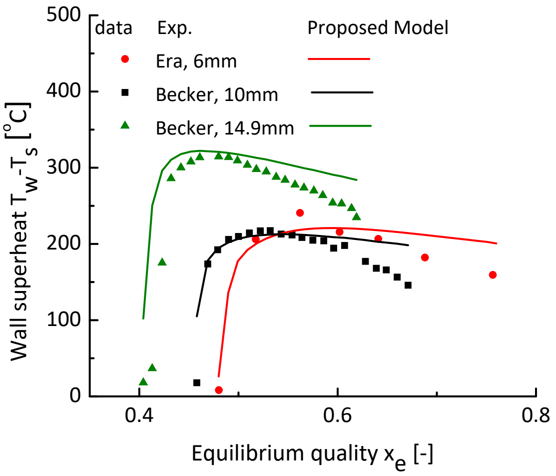

Figure 4.10.: Wall superheat comparisons between the proposed model and the water experiments (Era (Era et al., 1966), Becker (Becker et al., 1983)) with different diameters.

A series of similar flow conditions in different tube diameters are compared to investigate the influence of the tube diameter on the performance of the proposed model. Parameters of the compared experiments are listed in Table 4.5.

Figure 4.10 shows the wall superheat comparisons results. The Dryout quality measured in test *Era, 6mm* is higher than the dryout quality in test *Becker, 14.9mm*. The slightly higher mass flux in test *Era, 6mm* should lead to lower dryout quality. It can be concluded that the tube diameter influences the onset of dryout in a way that a smaller diameter results in a higher dryout quality. From the slope of the wall superheat profile in the fully developed region, the tube diameter does not influence the slope too much, but the proposed model predicts the slope a little positive while the diameter is small. This relates to the modelling of the weighting factor K_2. From the magnitude of the wall superheat, comparing tests *Becker, 14.9mm* and *Era, 6mm*, it can be concluded that the smaller tube diameter can result in a better heat transfer in the fully developed post-dryout region.

4.3.5. Conclusion

To sum up the comparison results in section 4.3, in general, the proposed model can well predict the wall superheat in both water and R-134a for post-dryout heat transfer. The LCS can well predict the magnitude of the wall superheat in water but predicts very poorly in R134a. The reason could be the incompatibility of the utilized Hadaller correlation or the overfitted empirical correction factor R_{Nu}, which is multiplied with the convective heat transfer correlation. The ATHLET only achieves accurate predictions in the very high quality flow or the flow with a very small thermal non-equilibrium degree. Usually, the conditions of very high pressure with very high mass flux can have a very small thermal non-equilibrium. The reason is that the model in the ATHLET code considers the flow without thermal non-equilibrium.

On the performance evaluation of the proposed model, the proposed model generally can well predict both the magnitude and the profiles of the wall superheat in both water and R-134a. However, the wall-vapor convective heat transfer enhancement, which is caused by the presence of droplets in the fully developed region, is overestimated in R-134a while the flow quality is low or the thermal non-equilibrium is small and underestimated in water while the flow quality is high. The wall superheat profiles are excellently predicted in both water and R-134a, indicating that the interfacial heat transfer between vapor and droplets is well modelled in the current work.

4.4. Comparison with existing models

4.4.1. Comparison with GRO, CSO, LCS, and ATHLET

The mainly used four existing models are GRO (Groeneveld and Delorme, 1976), CSO (Chen et al., 1979), LCS (Varone and Rohsenow, 1986), and ATHLET (Austregesilo et al., 2012). The GRO and CSO models directly correlate the relationship between the actual and equilibrium qualities to consider the thermal non-equilibrium. As the LCS considers three-path heat transfer that involves heat transfer among the heated wall, vapor, and droplets, dryout information is required by this solution. The modified Dougall-Rohsenow correlation (Liesch et al., 1975) in the ATHLET code is used in the current work, and it is a simple equilibrium correlation. Details of the selected models are summarized in chapter 2. The proposed model and these selected models are compared by calculating the post-dryout heat transfer under both the typical water and R-134a conditions. The compared two tests come from Becker and the KIT experiments, respectively. The parameters of these two tests are typical for post-dryout heat transfer with moderate conditions of pressure, mass flux, and heat flux, as listed in Table 4.6.

Figure 4.11 (a) shows the comparison result under typical water conditions for post-dryout heat transfer. The proposed model predicts well the wall superheat profile and magnitude. The LCS can predict a satisfied magnitude of the wall superheat, and it performs much better than the GRO, CSO, and ATHLET. Since the ATHLET adopts the equilibrium assumption, the vapor temperature increases to be above the saturation temperature while the equilibrium quality exceeds 1, resulting in a noticeable wall temperature increases. The

Table 4.6.: Test parameters of Becker and the KIT experiments for typical water and R-134a conditions, respectively.

Test Id	Fluid	Tube diameter $[mm]$	Pressure $[MPa]$	Mass flux $[kg/(m^2s)]$	Heat flux $[kW/m^2]$
Case1	water	10.0	7.0	1010.1	695
Case2	R-134a	10.0	1.6	500	65

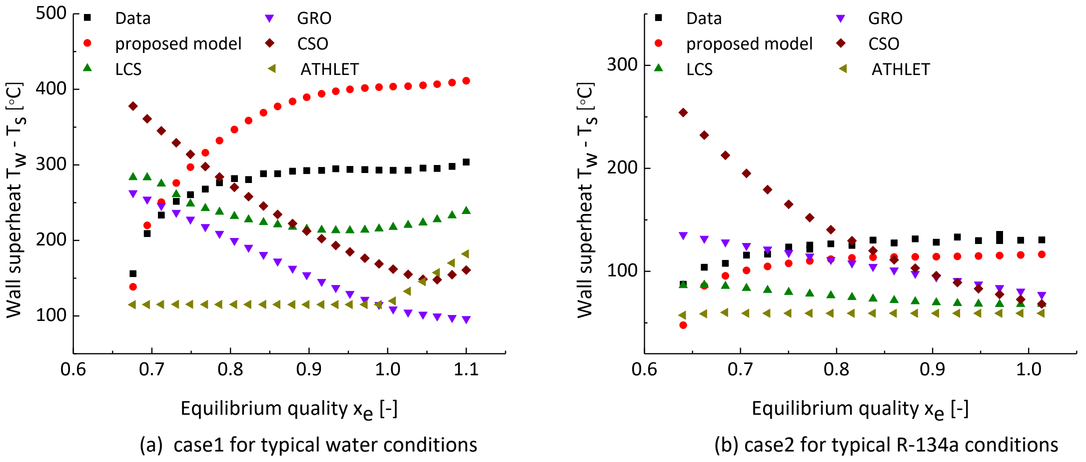

(a) case1 for typical water conditions

(b) case2 for typical R-134a conditions

Figure 4.11.: Comparison of wall superheat with GRO, CSO, LCS, and ATHLET.

CSO used an empirical correlation to predict the actual quality x_a, it predicted that x_a reaches to 1, while the equilibrium quality x_e is 1.05. Both the GRO and the CSO cannot predict well the wall superheat profiles.

Figure 4.11 (b) shows the comparison result under typical R-134a conditions for post-dryout heat transfer. The proposed model predicts well the wall superheat profiles and magnitude. All of LCS, GRO, and CSO predicted a decreasing profile of the wall superheat, and this tendency is also found in comparison with many other cases of the R-134a based KIT experiment. The ATHLET predicts the wall superheat nearly constant, while equilibrium quality $x_e < 1$, and predicts an increasing profile, while $x_e > 1$.

4.4.2. Comparison with Nishikawa et al. (1986)

As introduced in chapter 2, Nishikawa et al. (1986) conducted studies of post-dryout heat transfer based on the experimental data in Freon 22 (R-22) at high sub-critical pressures.

Table 4.7.: Test parameters of experiment in R-12 (Groeneveld, 1972).

Test Id	Tube diameter $[mm]$	Pressure $[MPa]$	Mass flux $[kg/(m^2s)]$	Heat flux $[kW/m^2]$	Dryout quality $[-]$
Case1	7.8	1.07	2713	290	0.353
Case2	7.8	1.07	665	123	0.622

Two cases from Groeneveld (1972) were selected and compared by Nishikawa. Parameters are listed in Table 4.7, and both cases are at low pressure. Case1 could have a smaller thermal non-equilibrium degree in the flow than Case2, which cannot be concluded for sure but only speculated when looking at the flow conditions. In both cases, the proposed model predicts worse than the Nishikawa model. The magnitude of the wall superheat

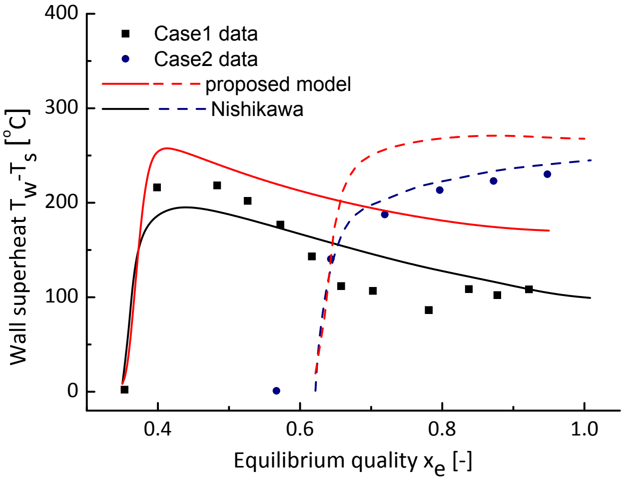

Figure 4.12.: Comparison of wall superheat with Nishikawa et al. (1986).

is obviously overestimated in both cases. When calculating Case2, the proposed model predicts that all the droplets are pushed away from the core region into the film region, the thermal non-equilibrium degree could be overestimated since the slope of the wall superheat profile in the fully developed region is underestimated. Merely from these two comparisons, though the proposed model predicts not severely in general, the model is found that the adopted correlation for convective heat transfer between wall and vapor in the proposed model tends to underestimate the HTC, and the interfacial heat transfer prediction in the proposed model tends to overestimate the HTC in R-12 conditions.

4.4.3. Comparison with Meholic (2011)

As introduced in chapter 2, Meholic (2011) developed a first-principle approach to quantify the direct contact heat transfer, and the model included thermal radiative and interfacial heat transfer between vapor and droplets. Two cases from Becker et al. (1983) selected and compared by Meholic shall be used here to have an evaluation of the model proposed in the current work.

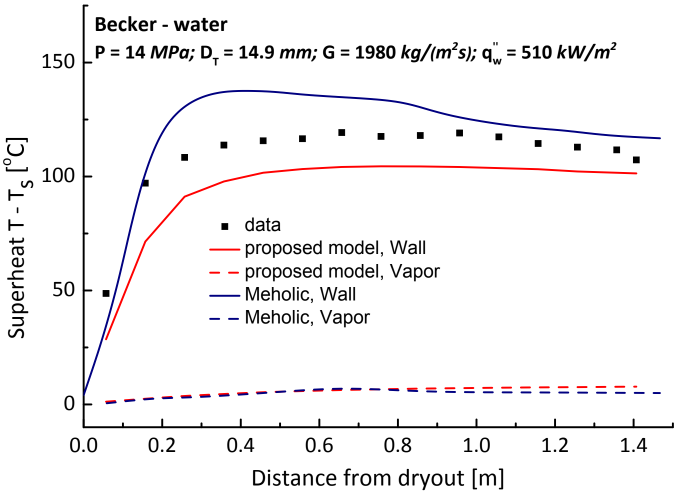

Figure 4.13.: Comparison of wall and bulk vapor superheats with Meholic (2011) for Case1.

Figure 4.13 shows the wall and bulk vapor superheats comparisons between Meholic model and the proposed model for Case1 with flow conditions of pressure 14 MPa, mass flux

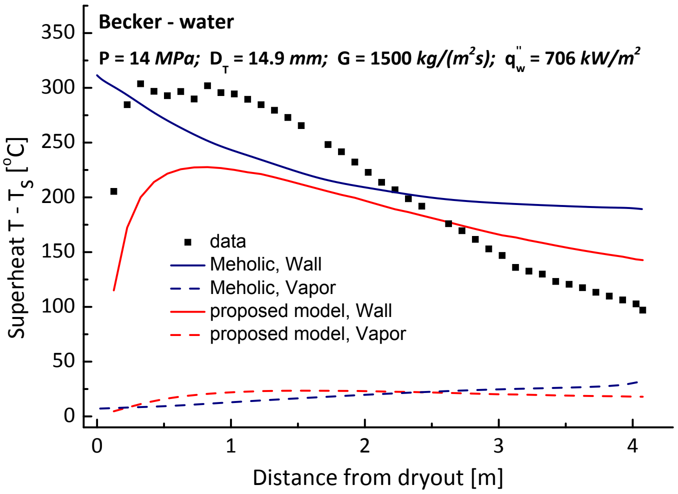

Figure 4.14.: Comparison of wall and bulk vapor superheats with Meholic (2011) for Case2.

$1980 kg/(m^2 s)$, and wall heat flux $510 kW/m^2$. Both models predict well the wall superheat. As for the prediction of vapor superheat, the two models predict a temperature increase of vapor just downstream of the dryout, and then keep nearly constant in the whole post-dryout region. It can be speculated that at the beginning of the post-dryout flow, the vapor in the film region is fast heated up, and the thermal non-equilibrium increases. While the flow reaches the fully developed post-dryout region, a large number of droplets are pushed away from the core region into the film region to lower the vapor temperature. Due to the high mass flux, the heat input is nearly all used to evaporate the droplets. Thus the bulk vapor temperature remains nearly constant.

Figure 4.14 shows the wall and bulk vapor superheats comparisons between Meholic model and the proposed model for Case2 with flow conditions of pressure 14 MPa, mass flux 1500 $kg/(m^2 s)$, and wall heat flux 706 kW/m^2. For the wall superheat comparison, the proposed model predicts the magnitude slightly better than Meholic model, and the proposed model well predicts the wall superheat profile. The reason is that the proposed model predicts a temperature decrease of the vapor along with the flow. For the predictions of vapor superheat, Meholic model predicts an increasing profile. Unlike this result, the proposed model predicts the bulk vapor superheat firstly to increase fast to very high, and then to decrease slowly in the fully developed region. It can be speculated that at the beginning of post-dryout flow, the proposed model captured a fast increase of the bulk vapor temperature as the mass flux is relatively low and the heat flux is relatively high, compared to the condition in Figure 4.13. Due to the relatively higher wall superheat in this condition, the vapor temperature in the film region is higher at the beginning of the flow. While the flow reaches the fully developed region, more droplets are pushed away into the film region and getting evaporated. The continuing evaporation of droplets increases the core turbulence intensity. This effect would strengthen the evaporation in the film region and lower the bulk vapor temperature along with the flow.

4.4.4. Comparison with Li and Anglart (2016)

As introduced in chapter 2, Li and Anglart (2016) developed an integrated CFD model for high quality two-phase flow, including trans-dryout regions from annular-mist regime to mist regime. Two different cases from Becker et al. (1983) experiment were used and compared by Li, and the parameters of the flow conditions are summarized in Table 4.8.

Figure 4.15(a) and Figure 4.15(b) show the wall superheat comparisons between the two models and Becker experiment tests 265 and 270, respectively. Both conditions are at an

Table 4.8.: Test parameters of Becker experiment.

Test Id	Tube diameter $[mm]$	Pressure $[MPa]$	Mass flux $[kg/(m^2s)]$	Heat flux $[kW/m^2]$	Dryout quality $[-]$
265	14.9	7.0	1484	878	0.497
270	14.9	7.0	997	670	0.648

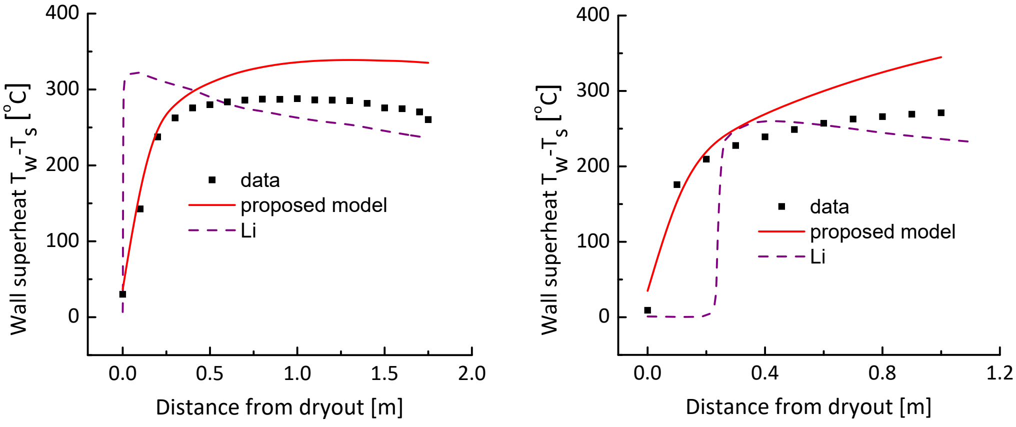

(a) Test 265 (b) Test 270

Figure 4.15.: Comparison of wall superheat with Li and Anglart (2016) for Becker experiment tests.

intermediate pressure, mass flux, and heat flux, representing the most typical post-dryout flow. In both comparisons, results show that the proposed model can well predict the wall superheat profiles but overestimates the magnitude, and the CFD model predicts the average wall superheat magnitude but always predicts a decreasing profile of the wall superheat after a quick wall temperature jump at dryout. The reasons can be speculated based on CFD modelling. There is only one transverse direction force considered in the CFD model, which is the turbulent dispersion force. This force can result in a continuous movement of droplets from the core region into the film region until impinging on the wall. Thus the thermal non-equilibrium degree is underestimated by the CFD model. This CFD model can predict only a decreasing profile of wall temperature except for conditions, which have only a few droplets in the flow.

4.5. Discussion on wall-vapor convection correlations

Based on the comparisons with existing models and correlations for post-dryout heat transfer in fluid: water, R-134a, and R-12, it can be indicated that the proposed model generally can provide good predictions of the magnitude and profiles of the wall temperature. Unlike the most previous models, which adopt different correlations for different fluid, the current work attempts to develop a general model by using the same equations for various fluids in vertical tubes. Forslund correlation (Forslund and Rohsenow, 1966) is modified to consider the large fluid property variations across the tube for convective heat transfer between wall and vapor in the current work, as shown in Eq. (3.10).

Impacts due to the presence of droplets on the convective heat transfer are complex. The effect can be heat transfer enhancement or deterioration. Though the modified Forslund correlation well average the impacts of the presence of droplets in different fluids, and it gave satisfying wall temperature prediction in the comparisons with existing models and correlations, it is still worth to discuss the selection of the wall-vapor convection correlation.

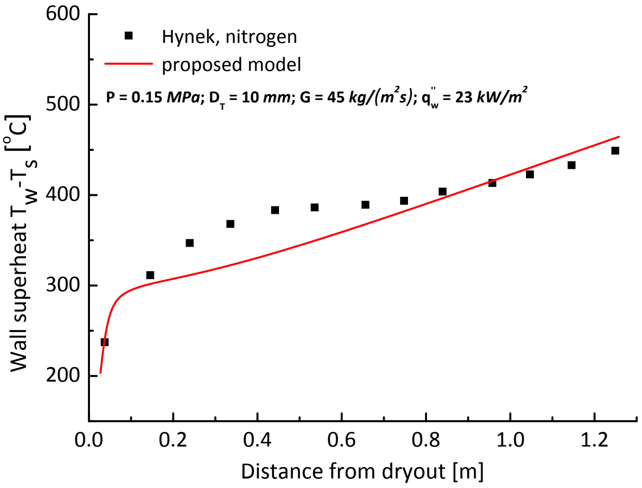

Figure 4.16.: Comparison of wall superheat between the proposed model and the nitrogen based test from Hynek (1969).

From the HTC comparison results shown in Tables 4.1 and 4.2, in general, the proposed model underestimates the HTC in water and overestimates the HTC in R-134a.

Since Forslund correlation was developed from dispersed flow film boiling tests in nitrogen, a comparison between the proposed model with nitrogen data from Hynek (1969) is implemented. Results in Figure 4.16 show that the proposed model can well predict the magnitude and profiles of the wall superheat. That indicates the adopted modified Forslund correlation well predicts the HTC between wall and vapor in this nitrogen test.

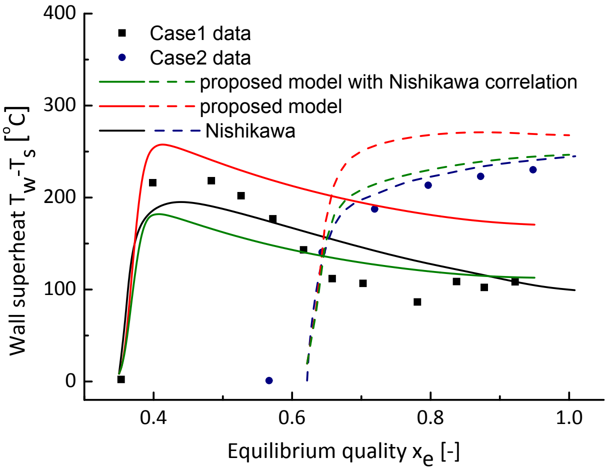

Figure 4.17.: Wall superheat predictions of the proposed model with Nishikawa correlation, the proposed model, and Nishikawa model.

In comparison with Nishikawa model by using the experiment in R-12 from Groeneveld (1972) as shown in Figure 4.12, though the proposed model predicts not badly in general, results show that the adopted modified Forslund correlation for convective heat transfer between wall and vapor in the proposed model tends to underestimate the HTC. On the contrary, Nishikawa model predicts the average magnitude of the wall superheat in both cases. Nishikawa developed the convective heat transfer correlation for his model for R-22, and the use in the fully developed region is shown as below,

$$h_{w-v} = 0.0048 \frac{k_v}{D_T} \left[\frac{G D_T}{\mu_v} \left(x_a + (1 - x_a) \frac{\rho_v}{\rho_d} \right) \right]^{0.92} Pr_v^{0.4} \tag{4.2}$$

With vapor properties evaluated at the bulk vapor temperature.

The proposed model with using the above Nishikawa correlation for predicting convective heat transfer between wall and vapor is compared, as shown in Figure 4.17. The results show that the proposed model with Nishikawa correlation predicts more or less the same profiles, but a better wall superheat magnitude than the proposed model. This indicates that the modified Forslund correlation underestimates the HTC between wall and vapor in these two R-12 cases.

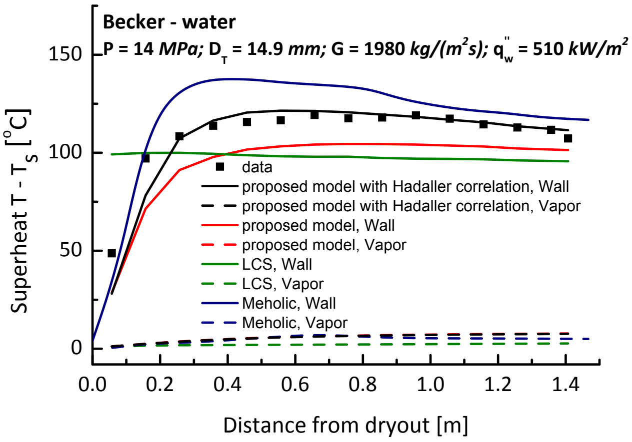

Figure 4.18.: Predictions of the proposed model with Hadaller correlation, the proposed model, the LCS, and Meholic model for Case1.

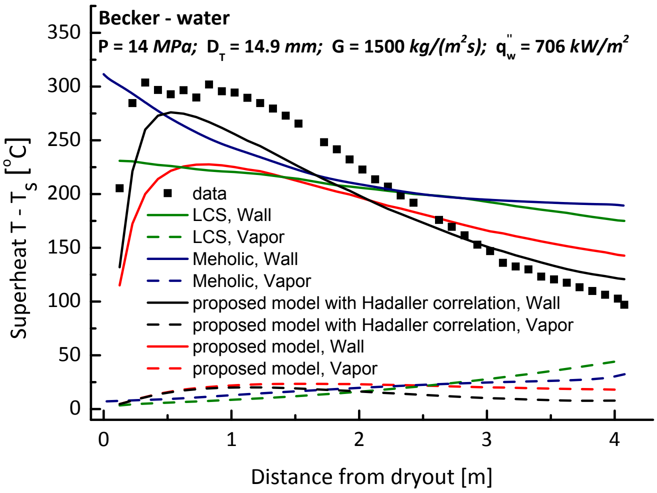

Figure 4.19.: Predictions of the proposed model with Hadaller correlation, the proposed model, the LCS, and Meholic model for Case2.

Hadaller correlation is frequently suggested to be used for the convective heat transfer between wall and vapor in water. The equation is shown below,

$$h_{w-v} = 0.008348 \frac{k_{vf}}{D_T} \left(\frac{G x_a D_T}{\mu_{vf} \alpha} \right)^{0.8774} (Pr_{vf})^{0.6112} \tag{4.3}$$

With vapor properties are evaluated at the film vapor temperature.

Figures 4.18 and 4.19 show the predictions of wall and vapor superheats in Case1 and Case2 by the proposed model with Hadaller correlation, the proposed model, the LCS, and Meholic model. The results show that the proposed model with Hadaller correlation has a better agreement in the prediction of temperature profiles and magnitude than the proposed model. For the predictions of vapor superheat in Figure 4.19, the proposed model with Hadaller correlation predicts a more decreasing profile in the fully developed post-dryout region. This is due to the higher film temperature obtained at the beginning. More evaporation would be generated and the accelerated vapor results in more droplets being driven into the film region to be evaporated. This indicates that the modified Forslund correlation over-averaged the HTC between wall and vapor in these two cases.

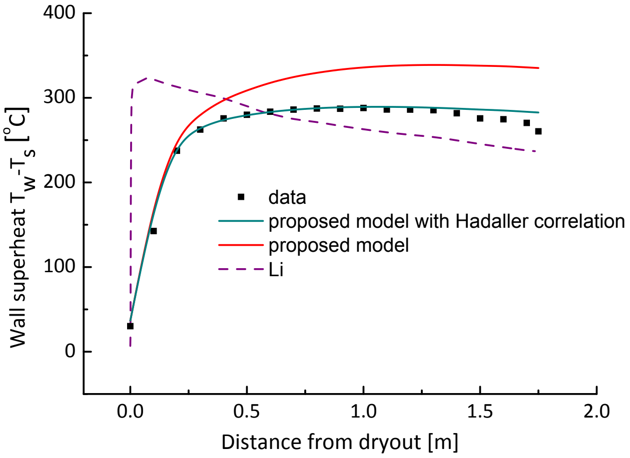

Figure 4.20.: Predictions of the proposed model with Hadaller correlation, the proposed model, and Li model on Becker experiment test 265.

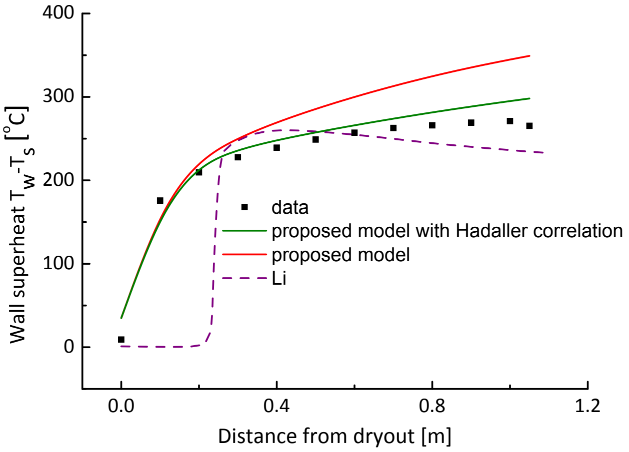

Figure 4.21.: Predictions of the proposed model with Hadaller correlation, the proposed model, and Li model on Becker experiment test 270.

Figures 4.20 and 4.21 show the predictions for wall and vapor superheat by the proposed model with Hadaller correlation, the proposed model, and Li model. The results show that the proposed model with Hadaller correlation has a better agreement in the prediction of the temperature profiles and magnitude than the proposed model. Due to the different selection of the convective heat transfer correlation, the proposed model predicts a different wall superheat slope in the fully developed post-dryout region.

To sum up, the use of the convective heat transfer correlation dramatically influences the accuracy of the proposed model. However, no reliable correlation exists for convective heat transfer between wall and vapor that has accounted for the impacts due to the presence of droplets for various fluids. These effects can result in heat transfer enhancement or deterioration depending on the fluid and flow conditions. Without considering these effects mechanistically, the correlation varies by the fitted exponents of Reynolds number and Prandtl number, and the exponents in the correlations for different fluid usually have a big difference since the magnitudes of these effects are varying by different fluids. Besides, the prediction of non-equilibrium also dramatically influences the accuracy of the model, as shown in Figure 4.19. The LCS and the proposed model with Hadaller correlation use the same correlation for convective heat transfer between wall and vapor, but very different wall superheats are calculated by this two models mainly due to the very differently predicted vapor superheat. The currently adopted modified Forslund correlation generally can provide good agreement in different fluids. However, if high-level accuracy is required, the convective heat transfer correlation can be selected for the specific fluid or to include the impacts on the convective heat transfer, which are due to the presence of droplets, into the convective heat transfer correlation between wall and vapor.

4.6. Prediction of the developing post-dryout region length

Table 4.9.: Verification results of predictions of developing region length.

	Water Experiments	**Freon Experiments**	**Total**
points number	23	7	30
average e [%]	-7.02	0.39	-5.29
RMS e [%]	37.63	24.04	34.93

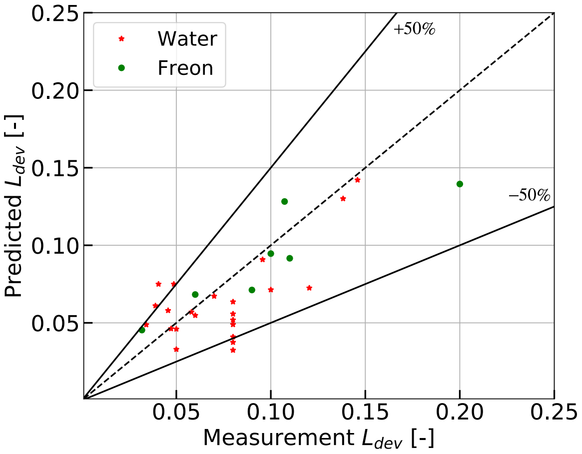

Figure 4.22.: Verification of predictions of developing region length.

A list of data coming from literature Bennett et al. (1968), Era et al. (1966), Cumo et al. (1974), Groeneveld (1972), and Nishikawa et al. (1983) are generated with uniform axial heat flux. The data are used to verify the prediction of the developing region length. Parameters of these data and the prediction results by Eq. (3.5) in the proposed model are listed in Table B.1.

Figure 4.22 shows the prediction results. Most predictions are within the deviation range of ±50%. Herein, the predicting error e is defined by Eq. (3.7), and the average error and RMS error are shown in Table 4.9. The verification shows that the developed correlation has similar accuracy for post-dryout flow in Freon compared with the results of the KIT experiment, which was introduced in chapter 3.1.3. However, the verification shows worse accuracy in water compared with the results of Becker experiment. Though a very limited number of data from literature is used for the verification, the results show that the proposed correlation can be used to predict the length of the developing post-dryout region.

4.7. Analysis of direct contact heat transfer between wall and droplets

Table 4.10.: Test parameters of experiments (Becker, KIT) under high and low pressures.

	Pressure $[MPa]$	Tube diameter $[mm]$	Mass flux $[kg/(m^2s)]$	Heat flux $[kW/m^2]$	Dryout quality $[-]$
Becker, water	14.0	14.9	1005	460	0.383
	3.0	14.9	1003	730	0.566
KIT, R-134a	2.8	10.0	492	40.1	0.51
	1.1	10.0	498	80.1	0.789

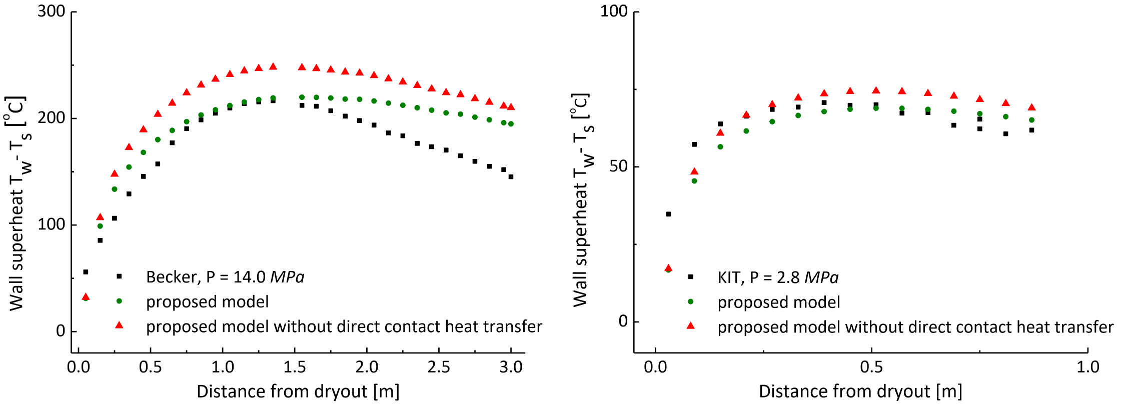

(a) high pressure in water, Becker

(b) high pressure in R-134a, KIT

Figure 4.23.: Contribution of direct wall-droplets contact heat transfer under high pressure.

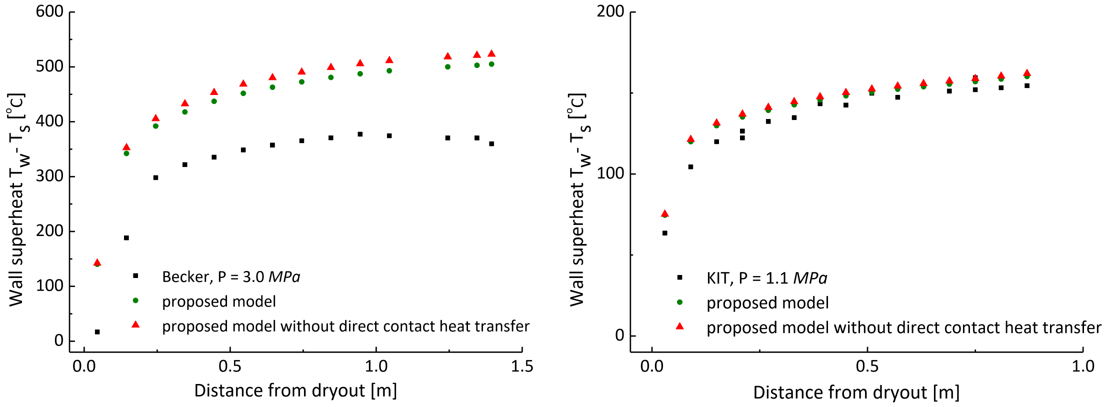

(a) low pressure in water, Becker

(b) low pressure in R-134a, KIT

Figure 4.24.: Contribution of direct wall-droplets contact heat transfer under low pressure.

As introduced in chapter 3.3.2, numerous researchers have investigated the contribution of direct contact heat transfer in post-dryout flow. The most accepted consensus is that the contribution of direct contact heat transfer could be significant in the developing post-dryout region, but is very limited in the fully developed post-dryout region. Generally, it could be less than 10% of the total heat to be transferred through wall-droplets contact heat transfer. In the current work, wall-droplets contact heat transfer is characterized by a parameter called the heat transfer effectiveness ε. The proposed model for calculating the effectiveness ε was developed by Kendall and Rohsenow (1978). The contribution of direct contact heat transfer between wall and droplets to the wall cooling is investigated through calculating post-dryout heat transfer by the proposed model with and without the inclusion of the direct contact part. Table 4.10 lists the parameters of different flow conditions of Becker and the KIT experiments.

Figure 4.23 shows the predictions of wall superheat by the proposed model with and without the inclusion of direct contact heat transfer under high pressures. The proposed model predicts obviously lower wall superheat than the model without the inclusion of direct contact heat transfer for both the water based Becker test and the R-134a based KIT test. This phenomenon can be explained such that a higher pressure results in a smaller non-equilibrium degree due to the higher density ratio ρ_v/ρ_d, which means the turbulent dispersion effects can be larger. That also means that droplets can be easier driven into the film region, causing a larger contact possibility. From the summarized equation (3.24), the effectiveness ε is proportional to $\sqrt{\rho_v/\rho_d}$, which confirms the explanation.

Figure 4.24 shows the prediction of wall superheat by the proposed model with and without the inclusion of the direct contact heat transfer under low pressure. The proposed model predicts similar wall superheat as the model without the inclusion of the direct contact heat transfer for both the water based Becker test and the R-134a based KIT test. This phenomenon means that the contribution of direct contact heat transfer to the post-dryout flow is small. It can be explained that a lower pressure results in a larger non-equilibrium degree due to the lower density ratio ρ_v/ρ_d, which leads the turbulent dispersion effect to be small. Thus, the droplets have less chance to impinge on the wall.

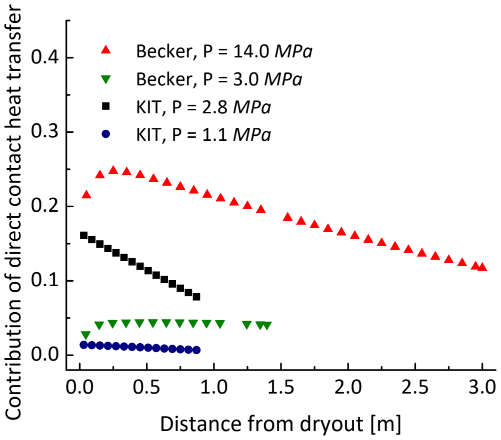

Figure 4.25.: Percentage of the heat transferred by the direct contact between wall and droplets to the total input.

Figure 4.25 shows the percentage of heat that transferred by the direct contact between wall and droplets to the total input in above calculated four tests. Under high pressure in the water, more than 20% of the total heat is transferred through wall-droplets contact heat transfer in the developing post-dryout region, and the contribution percentage decreases to around 10% in the fully developed post-dryout region. Under high pressure in R-134a, the contribution percentage is around 10% in the whole region and decreases along with the flow direction. Under low pressures, the contribution percentage decreases very slowly along with the flow direction, and the magnitude is in general tiny, which is less than 5%. Especially for the test in R-134a, the contribution percentage decreases to a value lower than 1%.

The contribution of direct contact heat transfer between wall and droplets obtained in this analysis is shown being more significant while in high pressure than in low pressure for both water and R-134a, and the contribution is more significant in the developing region than that in the fully developed region. For low pressures, this part of heat transfer can be neglected.

4.8. Assessment under conditions of non-uniform axial heat flux

Many of the practical applications in which post-dryout phenomena is highly interesting, such as nuclear reactors and steam generators, are characterized by strong axial variations of heat flux. The influence of non-uniform axial heat flux on CHF is quite obvious (Yang et al., 2006; Adamsson and Anglart, 2010). It is especially significant for conditions of high quality at CHF point, which is likely to be dryout. However, there are very few studies on the influence of the non-uniform axial heat flux on the post-dryout heat transfer. Keeys et al. (1972) developed a post-dryout model with a very good prediction for uniform axial heat flux conditions and found that the model needs to be modified to account for the effect of non-uniform axial heat flux conditions. Becker et al. (1988) investigated post-dryout heat transfer in a tube with circumferential non-uniform heating and then Becker et al. (1992) experimentally investigated the influence of axial heat flux distributions on post-dryout heat transfer for the flow of water in vertical tubes. 5 different wall heat flux profiles were carried out in this experiment, including inlet peak, middle peak, outlet peak, narrow middle peak, and narrow inlet peak. In total, 15928 data points were obtained in the whole post-dryout regime with a selection criterion of dryout void fraction $\alpha_{do} > 0.8$ from this databank. BeckerII experiment covers the following ranges of parameters:

Fluid: *water*

Heated length: 7000 mm

Inner diameter: 14.99 mm

Inlet subcooling: ~ 10 °C

Pressure: $1 - 16.0\ MPa$

Mass flux: $500 - 3100\ kg/(m^2\ s)$

Heat flux profile: inlet peak, middle peak, outlet peak, narrow middle peak and narrow inlet peak

Heat flux: $87 - 3087\ kW/m^2$

Steam quality (equilibrium): $0.07 - 1.45$

Both dryout and post-dryout heat transfer are history-dependent phenomena to some extent. For example, the droplets formation and non-equilibrium are depending on their upstream history. The variations of flow conditions (e.g. pressure, mass flux, heat flux) can have a great influence on the post-dryout heat transfer. Especially for such empirically derived relations for droplet size, non-equilibrium or actual quality, which are based on the local conditions, could be sensitive to such varying conditions. To apply the proposed model in the calculation of post-dryout heat transfer under conditions of non-uniform axial heat flux, the usage of the proposed model is different with the usage under conditions of uniform axial heat flux on the following two parts,

- heat flux q_w'' at dryout is used to calculate the initial droplet size in Eq. (3.18), and
- heat flux q_w'' at dryout is used to calculate the developing region length in Eq. (3.5).

4.8.1. Comparisons of heat transfer coefficients

For a general assessment of the accuracy of the proposed model in the prediction of post-dryout heat transfer with non-uniform axial heat flux conditions, comparisons of heat transfer coefficient are performed between the proposed model and BeckerII experiment. All the data are selected with a criterion of dryout void fraction $\alpha_{do} > 0.8$ to ensure most of the conditions are in the post-dryout region. Then there are 3820 data points in the developing region and 12108 data points in the fully developed region selected. The heat transfer coefficient (HTC) is defined by Eq. (4.1).

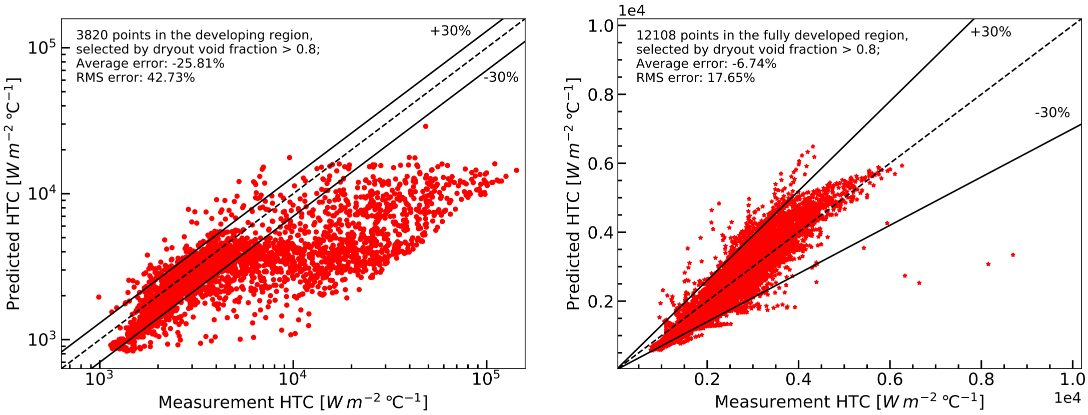

Figure 4.26.: HTC comparisons with BeckerII experiment, (a) in the developing post-dryout region, (b) in the fully developed region.

Figure 4.26 compares the predicted HTC with the measured ones in the water based BeckerII experiment with 5 different wall heat flux profiles. There are 3820 points in the developing post-dryout region compared. The results show that, on the average, the proposed model underestimates the experimental HTC by 25.81% with an RMS error of 42.73%. On the other hand, 12108 pints in the fully developed post-dryout region are compared. The results show that, on the average, the proposed model underestimates the experimental HTC by 6.74% with an RMS error of 17.65%. The error of the prediction is defined as the ratio of the difference between the predicted HTC and the measurement HTC to the measurement HTC.

Similar to the comparison results in section 4.2, the predictions of high HTC in the developing region are greatly underestimated by the proposed model for these non-uniform axial heat flux conditions. The reason was explained as the wall superheat is changing very fast in the area of high HTC. Thus the systematic error that produced in the experimental determination of dryout can lead to a very different prediction of HTC in this area by the proposed model. However, the current work is focused on the accurate prediction of the wall superheat profile rather than on the magnitude in these high HTC areas.

For predicting the HTC, four existing models (CSO, GRO, LCS, ATHLET) are compared with the proposed model. Results of the HTC predictions compared with BeckerII experiment are listed in Table 4.11. All the models, excluding the model in the ATHLET code, underestimate HTC in the developing region. For predictions in the fully developed region, the CSO model underestimates the HTC while compared with Becker experiment under uniform heat flux conditions, but greatly overestimates the HTC while compared with BeckerII experiment under non-uniform axial heat flux conditions. The GRO model predicts BeckerII experiment much better than predicts Becker experiment, and the LCS predicts worse BeckerII experiment than Becker experiment. Like the GRO, the ATHLET

Table 4.11.: HTC predicting accuracy of CSO, GRO, LCS, ATHLET, and the proposed model compared with the water based BeckerII experiment.

	Developing region (3820 points)		Fully developed region (12108 points)		Whole region (15928 points)	
	average e [%]	RMS e [%]	average e [%]	RMS e [%]	average e [%]	RMS e [%]
CSO	-34.71	50.55	45.54	64.63	28.21	61.87
GRO	-13.59	44.76	54.26	69.00	38.10	64.07
LCS	-23.40	41.61	18.25	26.50	8.82	30.58
ATHLET	57.32	107.17	134.01	142.20	111.83	133.00
Proposed model	-25.81	42.73	-6.74	17.65	-11.32	25.97

also achieves better predictions of BeckerII experiment. Among all the models, the proposed model predicts the best in general by comparing the RMS error. On average, the proposed model still underestimates the HTC in all regions. The reason can be explained as the post-dryout flow in BeckerII experiment with non-uniform axial heat flux could have a smaller non-equilibrium degree compared with the Becker experiment. The proposed model maintains the same performance under such non-uniform heat flux conditions compared to under the uniform heat flux conditions. This is due to the consideration of an upstream effect in the proposed model. For such equilibrium correlations or models that always predict very small non-equilibrium, such as the ATHLET and the GRO, their performances in comparison with BeckerII experiment are raised. For the CSO and the LCS, some empirical relations and factors are derived for uniform axial heat flux conditions based on the local flow parameters, and such relations and factors did not include the influence coming from upstream, which would lead to wrong estimations under non-uniform heat flux conditions.

4.8.2. Wall superheat predictions under inlet peak heat flux conditions

Figure 4.27 shows the wall superheat comparisons between the proposed model and BeckerII experiment under inlet peak heat flux conditions. All the compared cases are selected with three representative pressures with intermediate mass flux conditions. The wall heat flux axial distribution is shown in Figure 4.27(a), the heat flux moderately increases to peak around 1.5 times of the average value at the place around 1/5 of the heated length, and then decreases slowly to around half of the average heat flux $\overline{q''_w}$ at the end of the tube.

Figure 4.27(b) shows the wall superheat comparisons under low pressure conditions. Dryout in these compared cases occur at the heat flux decreasing part. The proposed model predicts excellent wall superheat profiles in the whole post-dryout region and slightly overestimates the magnitude. Figure 4.27(c) shows the wall superheat comparisons under intermediate pressure conditions. Dryout in all of these compared cases occur at the heat flux decreasing part. The proposed model predicts very well both the wall superheat magnitude and the profiles in whole post-dryout region. Figure 4.27(d) shows the wall superheat comparisons under high pressure conditions. Dryout in these compared cases also occur at the heat flux decreasing part. The proposed model predicts good wall superheat profiles in the whole region for all these cases, and slightly overestimates the wall superheat magnitude for the two cases that have lower average heat fluxes $\overline{q''_w}$, and slightly underestimates the wall superheat magnitude for the case that has high $\overline{q''_w}$. As investigated in section 4.7, the direct contact heat transfer under conditions of high pressure with uniform axial heat flux is significant, especially in the developing post-dryout region. For these high pressures with non-uniform axial heat flux conditions, this effect could be more significant compared to the uniform axial heat flux condition. As shown in Figure

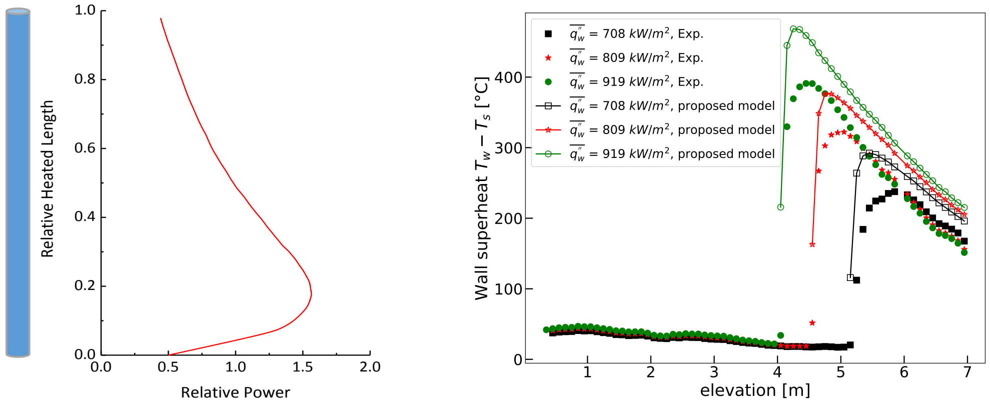

(a) Inlet peak heat flux (b) $P:\ 1\,MPa$; $G:\ 1500\,kg/(m^2\ s)$

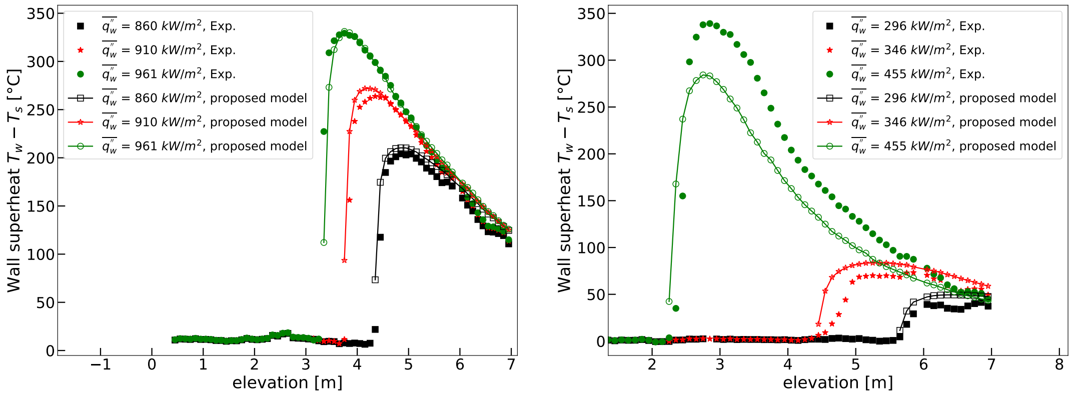

(c) $P:\ 7\,MPa$; $G:\ 1500\,kg/(m^2\ s)$ (d) $P:\ 14\,MPa$; $G:\ 1000\,kg/(m^2\ s)$

Figure 4.27.: Wall superheat predictions under inlet peak heat flux conditions.

4.27(d), the wall superheat in the developing region of the two cases that have lower $\overline{q''_w}$ is not so high, and it increases linearly. The proposed model can predict the trend of a slower increase of the wall superheat in the developing region for uniform axial heat flux conditions. However, for these two cases, the proposed model obviously overestimates the wall superheat in the developing region. This could be due to two reasons: First is the non-uniform axial heat flux conditions, which probably results in more wall-droplet direct contact heat transfer, and the proposed model underestimates this part of heat transfer. Second is the low wall superheat, which could be lower than the rewetting temperature. Thus the wall-droplets contact can easily wet the wall surface. In such cases, the wet contact heat transfer between wall and droplets takes a larger percentage of the heat transfer contribution compared to the other cases, where the wall superheat is high.

4.8.3. Wall superheat predictions under middle peak heat flux conditions

Figure 4.28 shows the wall superheat comparisons between the proposed model and BeckerII experiment under middle peak heat flux conditions. All the compared cases are selected with three representative pressures with intermediate mass flux conditions. The wall heat flux axial distribution is shown in Figure 4.28(a), the heat flux moderately increases to peak around 1.5 times of the average value at the place around 1/2 of the heated length, and then decreases moderately to around half of the average heat flux $\overline{q''_w}$ at the end of the tube. Dryout in all of these cases occur at the heat flux decreasing part.

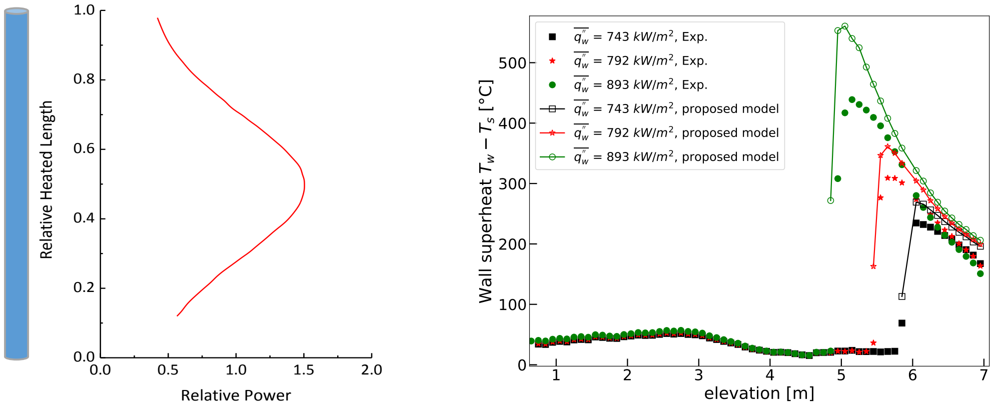

(a) Middle peak heat flux (b) $P:\ 1\,MPa;\ G:\ 1500\,kg/(m^2\,s)$

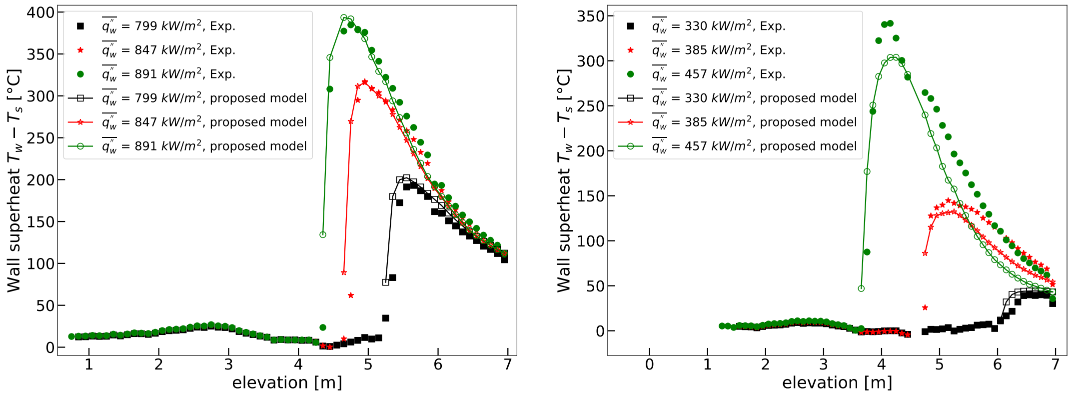

(c) $P:\ 7\,MPa;\ G:\ 1500\,kg/(m^2\,s)$ (d) $P:\ 14\,MPa;\ G:\ 1000\,kg/(m^2\,s)$

Figure 4.28.: Wall superheat predictions under middle peak heat flux conditions.

Figure 4.28(b) shows the wall superheat comparisons under low pressure conditions. The proposed model predicts excellent wall superheat profiles in the whole post-dryout region and slightly overestimates the magnitude. Figure 4.28(c) shows the wall superheat comparisons under intermediate pressure conditions. The proposed model predicts very well the wall superheat magnitude and profiles in the whole post-dryout region. Figure 4.28(d) shows the wall superheat comparisons under high pressure conditions, and the proposed model predicts good wall superheat profiles in the whole region for all these cases. It slightly underestimates the wall superheat magnitude for the two cases that have higher average heat fluxes $\overline{q''_w}$, and slightly overestimates the wall superheat magnitude for the case that has low $\overline{q''_w}$. Wall superheat in the developing region of the case with lowest $\overline{q''_w}$ shows the same trend with that in the inlet peak heat flux conditions. The wall superheat is found to be not so high, and it increases linearly. For such cases, the proposed model obviously overestimates the wall superheat.

4.8.4. Wall superheat predictions under outlet peak heat flux conditions

Figure 4.29 shows the wall superheat comparisons between the proposed model and BeckerII experiment under outlet peak heat flux conditions. All the compared cases are selected with three representative pressures with intermediate mass flux conditions. The wall heat flux axial distribution is shown in Figure 4.29(a), the heat flux slowly increases to peak around 1.5 times of the average value at a place around 4/5 of the heated length, and then decreases moderately to around half of the average heat flux $\overline{q''_w}$ at the end of the tube.

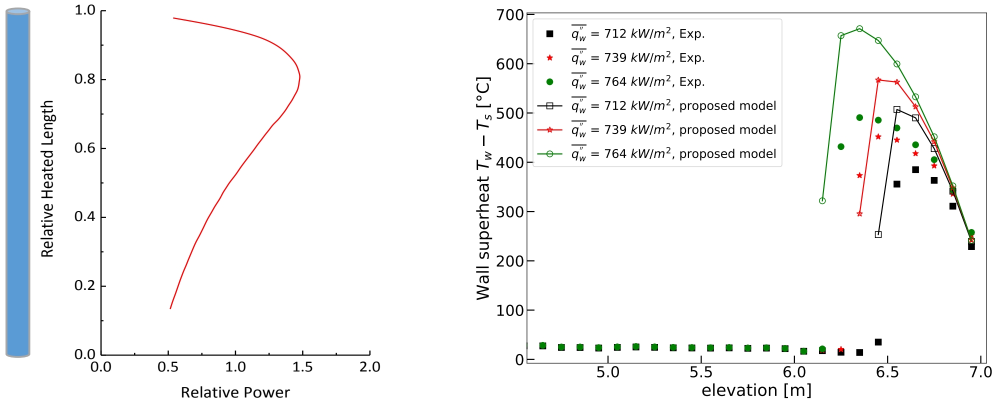

(a) Outlet peak heat flux (b) $P:\ 1\,MPa;\ G:\ 1500\,kg/(m^2\ s)$

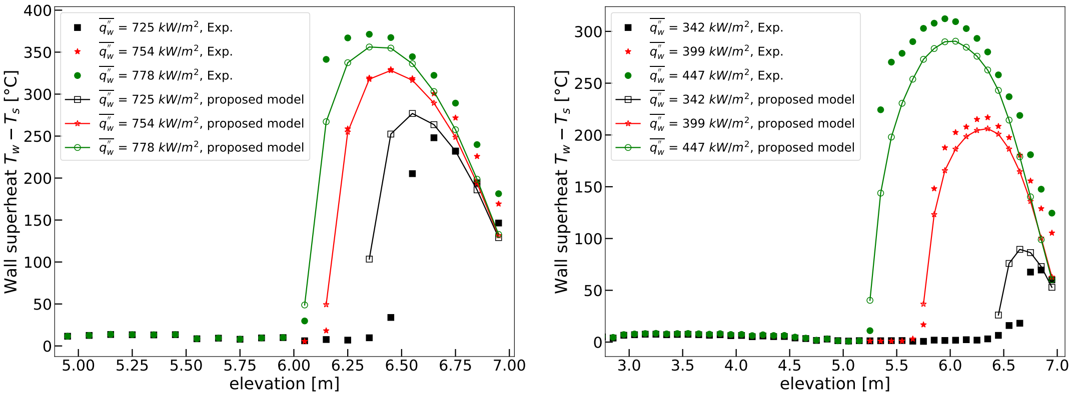

(c) $P:\ 7\,MPa;\ G:\ 1500\,kg/(m^2\ s)$ (d) $P:\ 14\,MPa;\ G:\ 1000\,kg/(m^2\ s)$

Figure 4.29.: Wall superheat predictions under outlet peak heat flux conditions.

Figure 4.29(b) shows the wall superheat comparisons under low pressure conditions. Dryout in all of these compared cases occur at the heat flux decreasing part. The proposed model predicts good wall superheat profiles in the whole post-dryout region, and firstly overestimates the wall superheat magnitude around the heat flux peak place, and then the predicted wall superheat drops quickly in the heat flux moderate decreasing part. Figure 4.29(c) shows the wall superheat comparisons under moderate pressure conditions. Dryout in these compared cases occur at the heat flux decreasing part. The proposed model predicts well the wall superheat profiles and magnitudes in the whole post-dryout region. Figure 4.29(c) shows the wall superheat comparisons under high pressure conditions. Dryout in the case with the highest average heat flux occurs at the heat flux increasing part. The proposed model underestimates the wall superheat in the two cases that have higher $\overline{q''_w}$. The wall superheat in the developing region of the case that has the lowest $\overline{q''_w}$ shows the same trend of a slowly increasing. Reasons are explained as the wall can be wetted in such conditions and the wet contact heat transfer between wall and droplets contributes more, or the wall-droplets contact heat transfer is underestimated by the proposed model for such conditions, or both the former two reasons.

4.8.5. Wall superheat predictions under narrow middle peak heat flux conditions

Figure 4.30 shows the wall superheat comparisons between the proposed model and BeckerII experiment under narrow middle peak heat flux conditions. All the compared cases are selected with three representative pressures with intermediate mass flux conditions. The wall heat flux axial distribution is shown in Figure 4.30(a), the heat flux fast increases to peak around 2.0 times of the average value at the place around 1/2 of the heated length, and then decreases fast to around half of the average heat flux $\overline{q''_w}$ at the end of the tube. Dryout in all of these compared cases occur at the heat flux decreasing part.

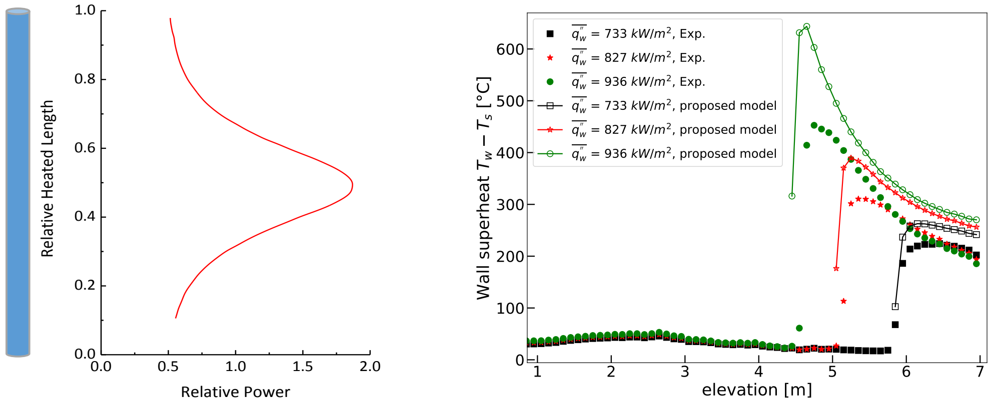

(a) Narrow middle peak heat flux

(b) $P:\ 1\,MPa$; $G:\ 1500\,kg/(m^2\ s)$

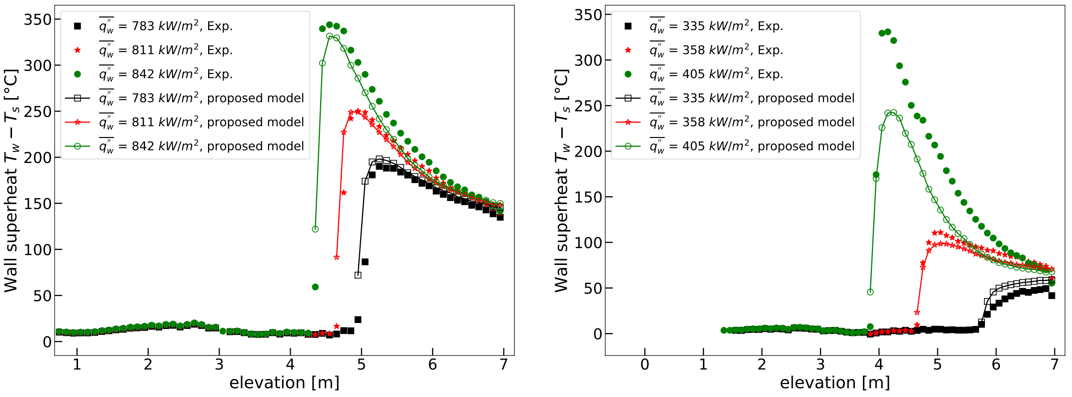

(c) $P:\ 7\,MPa$; $G:\ 1500\,kg/(m^2\ s)$

(d) $P:\ 14\,MPa$; $G:\ 1000\,kg/(m^2\ s)$

Figure 4.30.: Wall superheat predictions under narrow middle peak heat flux conditions.

Figure 4.30(b) shows the wall superheat comparisons under low pressure conditions. The proposed model predicts good superheat profiles and overestimates the magnitudes. Figure 4.30(c) shows the wall superheat comparisons under intermediate pressure conditions. The proposed model predicts very well the wall superheat magnitude and profiles in the whole post-dryout region. Figure 4.30(d) shows the wall superheat comparisons under high pressure conditions, and the proposed model also predicts good profiles, slightly underestimates the wall superheat for the two cases that have higher average heat flux, and overestimates the wall superheat for the case that has lowest $\overline{q''_w}$. In this case, the wall superheat in the developing region is also found to have a slowly increasing trend.

4.8.6. Wall superheat predictions under narrow inlet peak heat flux conditions

Figure 4.31 shows the wall superheat comparisons between the proposed model and BeckerII experiment under narrow middle peak heat flux conditions. All the compared cases are selected with three representative pressures with intermediate mass flux conditions. The

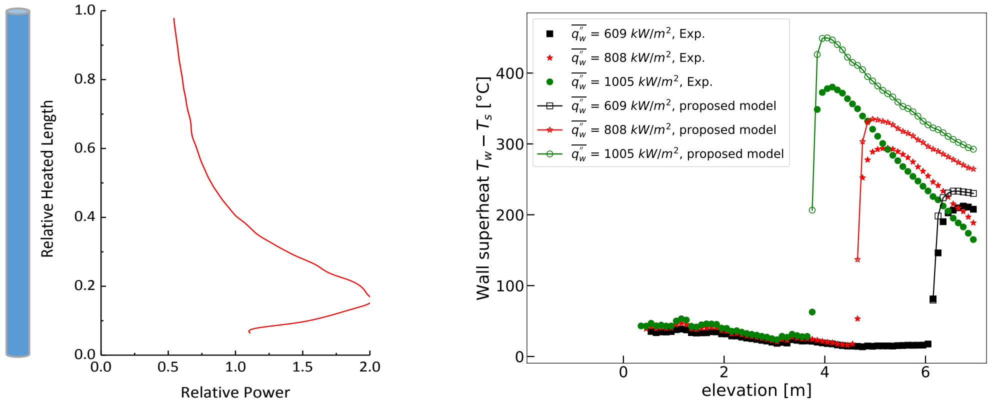

(a) Narrow inlet peak heat flux

(b) $P:\ 1\,MPa$; $G:\ 1500\,kg/(m^2\ s)$

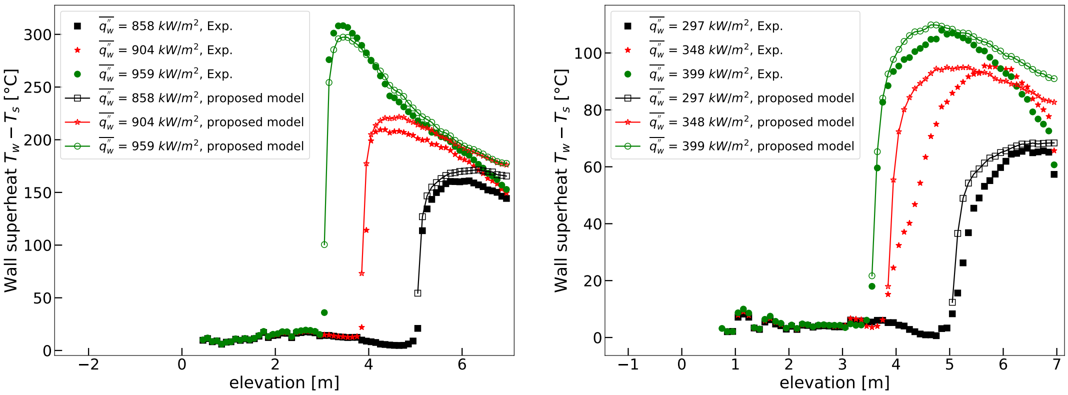

(c) $P:\ 7\,MPa$; $G:\ 1500\,kg/(m^2\ s)$

(d) $P:\ 14\,MPa$; $G:\ 1000\,kg/(m^2\ s)$

Figure 4.31.: Wall superheat predictions under narrow inlet peak heat flux conditions.

wall heat flux axial distribution is shown in Figure 4.31(a), the heat flux sharply increases to peak around 2.0 times of the average value at a place around 1/5 of the heated length, and then decreases fast to around half of the average heat flux $\overline{q_w''}$ at the end of the tube. Dryout in all of these compared cases occur at the heat flux decreasing part.

Figure 4.31(b) shows the wall superheat comparisons under low pressure conditions. The proposed model overestimates the magnitudes of wall superheat. Figure 4.31(c) shows the wall superheat comparisons under intermediate pressure conditions. The proposed model predicts good wall superheat profiles and slightly overestimates the magnitudes. Figure 4.31(d) shows the wall superheat comparisons under high pressure conditions. The proposed model overestimates the magnitudes of the wall superheat, and the wall superheat in the developing region of the two cases that have lower average heat flux $\overline{q_w''}$ also increase slowly, when the wall superheat is not so high.

4.8.7. Prediction of the developing region length under non-uniform heat flux conditions

For simplicity, the prediction for the developing region length under non-uniform heat flux conditions by the proposed model is calculated by Eq. (3.5) with the heat flux q_w'' at dryout is used. BeckerII experiment is selected with a criterion of dryout void fraction $\alpha_{do} > 0.8$, then there are 734 test runs obtained to compare with the predictions. As shown in Figure 4.32, most predictions are within the deviation range of ±50%. Herein, the predicting error e is defined in Eq. (3.7), and the average error and RMS error of the predictions are 11.65% and 31.44%, respectively.

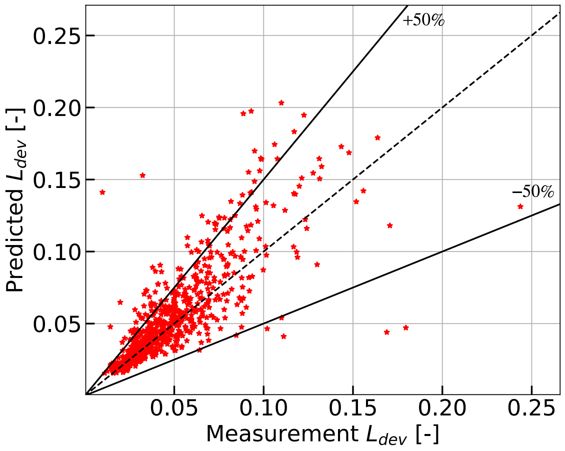

Figure 4.32.: Developing region length predictions under non-uniform heat flux conditions.

The developing region length L_{dev} is on average obviously overestimated, which is due to the usage of dryout heat flux for such non-uniform heat flux conditions. Dryout in most test runs of this BeckerII experiment occur at the heat flux decreasing part, and a higher heat flux would result in a longer developing region length through Eq. (3.7). Thus, the usage of dryout heat flux would result in overestimation.

4.9. Conclusion and discussion

In this chapter, four existing post-dryout heat transfer models including GRO (Groeneveld and Delorme, 1976), CSO (Chen et al., 1979), LCS (Varone and Rohsenow, 1986), and ATHLET (Austregesilo et al., 2012), and three experiments including two uniform axial heat flux Becker (Becker et al., 1983) and the KIT (Köckert et al., 2018) experiments and one non-uniform axial heat flux BeckerII (Becker et al., 1992) experiment, are mainly used in the assessment of the proposed model.

conditions of uniform axial heat flux

First, there are 3944 data points in Becker experiment and 2375 data points in the KIT experiment, which are selected by a criterion of dryout void fraction $\alpha_{do} > 0.8$ to ensure the most of the flow conditions are in the post-dryout region, though the proposed model can predict a broader range. Then the proposed model and the four existing models are compared with these data. The results show that the proposed model predicts HTC the best both the water based Becker and the R-134a based KIT experiments, among these models. The proposed model generally underestimates Becker experimental HTC by 13.82% with an RMS error of 20.05%, and overestimates the KIT experimental HTC by 6.86% with an RMS error of 10.32%, in the fully developed post-dryout region.

Secondly, predictions of the wall superheat by the proposed model are investigated by comparing with experiments under different conditions. In general, compared with Becker experiment, the proposed model predicts better at intermediate and high pressures than at low pressure. Compared with the KIT experiment, the proposed model predicts more or less the same accuracy under different pressures. For high quality flow, the influences on the post-dryout heat transfer due to the presence of droplets are small, and for low quality flow, the influences are significant. The comparison shows that the proposed model well predicted the wall superheat profile. However, the model tends to overestimate the magnitude of wall superheat for high quality flow in water and underestimates the magnitude of wall superheat for low quality flow in R-134a. For the conditions of small and large thermal non-equilibrium, the proposed model overestimates the wall superheat for both conditions in water, underestimates the wall superheat for large thermal non-equilibrium in R-134a, and well predicts the wall superheat for small thermal non-equilibrium in R-134a. This is due to the correlation, which is used in the proposed model for convective heat transfer between wall and vapor does not consider the impact caused by the presence of droplets. Thus the discussion on the selection of the wall-vapor convection correlation is also implemented, and the conclusion is that a correlation with fitted exponents of Reynolds number and Prandtl number can not well model the impacts of the presence of droplets on the convective heat transfer for various fluids in wide ranges of flow conditions. The currently adopted modified Forslund correlation generally can provide a good prediction for different fluids in a wide range of flow conditions. However, if high accuracy is required, the convective heat transfer correlation can be selected for a specific fluid or to include the impacts on convective heat transfer due to the presence of droplets. Besides, the tube diameter is found to influence post-dryout heat transfer by means of that a smaller diameter resulting in a higher dryout quality and a better heat transfer in the fully developed region, but it nearly does not influence the slope of the wall superheat profile.

What's more, the proposed model is compared with some other existing models including Nishikawa et al. (1986), Meholic (2011), and Li and Anglart (2016) and some other experiments including Bennett et al. (1968), Cumo et al. (1974), Era et al. (1966), Groeneveld (1972), and Hynek (1969). The results show that the proposed model can provide good predictions for various fluids in a wide range of flow conditions. While comparing the bulk vapor temperature, the proposed model is the only model that can predict a profile of first increasing and then decreasing, which is also agreed by Varone (1990), in which, the author predicted this kind of profile by considering effects of gradual droplet breakup downstream of dryout.

Last, a list of data coming from literature Bennett et al. (1968), Era et al. (1966), Cumo et al. (1974), Groeneveld (1972), and Nishikawa et al. (1983) were generated under uniform axial heat flux conditions and are used to verify the predicting accuracy of developing region length L_{dev}. Parameters of these data and the prediction results by Eq. (3.5) in the proposed model are listed in Table B.1. Though a very limited number of data from literature are used for verification, the results show that the proposed correlation can be used to predict the length of developing post-dryout region. The contribution of direct contact heat transfer between the wall and droplets is analyzed. It is found that this part of heat transfer is more significant in the developing post-dryout region than in the fully developed region. Besides, the direct contact heat transfer contributes much more significantly at high pressures than at low pressures. It can be concluded that, at low pressures, the direct contact heat transfer between wall and droplets can be neglected.

conditions of non-uniform axial heat flux

There are 3820 data points in the developing region and 12108 data points in the fully developed region selected from BeckerII experiment with the criterion of dryout void fraction $\alpha_{do} > 0.8$. Then the proposed model and four existing models are compared with these data. The results show that the proposed model predicts HTC the best and generally underestimates BeckerII experimental HTC by 6.74% with an RMS error of 17.65% in the fully developed region. Under non-uniform axial heat flux conditions, empirical relations and factors, which are derived for uniform axial heat flux conditions based on the local flow parameters, could lead to wrong estimations under non-uniform heat flux conditions.

The proposed model maintains the same performance in such non-uniform heat flux conditions compared to the uniform heat flux conditions. This is due to the consideration of an upstream effect in the model.

Predictions of wall superheat by the proposed model are investigated by comparing with BeckerII experiment under different non-uniform axial heat flux conditions. Generally, the proposed model can well predict the wall superheat profiles and magnitudes in the whole post-dryout region, and tends to overestimate the wall superheat while the pressure is low. For all conditions of 5 different axial wall heat flux profiles, including inlet peak, middle peak, outlet peak, narrow middle peak, and narrow inlet peak, the wall superheat is found to increase very slowly in the developing region while the pressure is high and the wall superheat is low. The proposed model can obviously overestimate the wall superheat for such cases. The reasons are explained as the wall can be wetted in such conditions and the wet contact heat transfer between wall and droplets contributes more, or the wall-droplets contact heat transfer is underestimated by the proposed model for such conditions, or both the former two reasons.

The predicting accuracy of the developing region length L_{dev} under the non-uniform axial heat flux conditions is verified by comparing with BeckerII experiment. The average error and RMS error of the predictions are 11.65% and 31.44%, respectively. The apparent overestimation is due to the usage of the dryout heat flux, which is higher than the average heat flux in the developing region.

5. Fluid-to-fluid modelling of post-dryout heat transfer

Fluid-to-fluid modelling is a technique by which the thermal and hydraulic behaviors of a given system can be studied using a model fluid with the lower latent heat of vaporization and lower critical pressure rather than using the water. The interest in the fluid-to-fluid modelling arises primarily because of the problems in the thermal and hydraulic design of pressurized water-cooled nuclear reactors. Dryout and post-dryout heat transfer are such problems. In order to reduce the cost and technical difficulties of the water-based post-dryout experiments, Freon family fluids have been frequently used as the model fluid because of their lower latent heat of vaporization and lower critical pressure.

5.1. Previous works

Dimensional analysis has been applied successfully in both the theoretical modelling of CHF phenomenon and the fluid-to-fluid modelling of CHF. However, fluid-to-fluid modelling of post-dryout heat transfer is not well established according to the review of public literature, and rare studies were found devoted to this topic. One work in the past is introduced as following,

Groeneveld et al. (1997)

Groeneveld et al. (1997) indicated that in the fluid-to-fluid modelling of two-phase flow phenomena such as CHF and post-dryout heat transfer, geometric and dynamic similarities must be satisfied. Generally, the scaling of post-dryout heat transfer should be implemented by using the same heated length over diameter (L_T/D_T) ratio in both model and prototype facilities. In practices, the modelling accuracy can be enhanced if identical geometries used. Thermodynamics similarity requires the equivalent thermodynamic properties of the two fluids, which can be achieved when qualities in both model and prototype facilities are equal at any axial location (L_T/D_T) along with the length.

The actual quality in post-dryout flow is hard to be controlled directly or indirectly since non-equilibrium exists, Groeneveld et al. (1997) utilized the equilibrium qualities equal to achieve this thermodynamic similarity. Through the heat balance equation,

$$x_e(L_T) = 4\left(\frac{q_w^{''}}{Gi_{v-d}}\right)\left(\frac{L_T}{D_T}\right) - \left(\frac{\Delta i}{i_{v-d}}\right) \tag{5.1}$$

With assuming a constant heat flux $q_w^{''}$. Then, the dimensionless number $q_w^{''}/Gi_{v-d}$ and the inlet quality $\Delta i/i_{v-d}$ must be equal, respectively. For the hydrodynamic similarity, equal density ratios (ρ_v/ρ_d) in both fluids were required. As for the dimensionless number $\Psi(G)$ involving mass flux, it is the important part to apply compensated distortion coefficients to make it appropriate for the studied phenomena. Groeneveld et al. (1997) suggested to use the group $Re_v Pr^{0.5}$ as dimensionless number $\Psi(G)$ through concluding research results from Hammouda et al. (1996), in which post-dryout heat transfer was studied in three different Freons.

5.2. Derivation of dimensionless numbers

In the current work, the scaling method of fluid-to-fluid modelling for post-dryout heat transfer is based on the dimensional analyses by using Buckingham Pi-theorem (Buckingham, 1914). First of all, scaling in the current work is performed for the heat flux controlled system. Thus the wall temperature is considered as the dependent variable. For such systems, properties of the fluid, which are in the near-wall region, are not controllable. Therefore, the near-wall fluid properties cannot be taken into consideration in the scaling method, though this could probably limit the developed scaling method into a small application range, where the wall superheat cannot be too high.

To develop the scaling method, it is necessary first to know the relevant dimensionless numbers that determine the post-dryout heat transfer. The dimensionless numbers are derived from the combination of a series of independent variables which usually can be found by logic or intuition and developed from previous experiences with problems of a similar nature. However, it is impossible to ensure that all the essential quantities have been included.

Based on the experiences of theoretical investigation in post-dryout heat transfer, The independent variables that determine the wall temperature in a post-dryout flow in a round tube can be described as below,

The system describing variables: P, G, $q_w^{''}$, Δi, L_T, D_T, g

where P is the system pressure, G is the inlet mass flux, $q_w^{''}$ is the wall heat flux, Δi is the subcooling of the inlet flow, equals the enthalpy difference of the saturation liquid and the flow at inlet. L_T is the heated length of the tube, and D_T is the inner diameter of the tube, g is gravitational acceleration.

The detail analyses usually take into account the pressure P via saturation temperature T_s, or via physical properties that evaluated at the saturation temperature. The primary properties would be used in the derivation of dimensionless numbers are listed as below,

The properties describing variables: i_{v-d}, ρ_d, ρ_v, μ_d, μ_v, $C_{p,d}$, $C_{p,v}$, k_d, k_v, σ

where, i_{v-d} is the latent heat of evaporation, ρ_d and ρ_v are the droplet and vapor densities at saturation temperature individually, μ_d and μ_v are the droplet and vapor viscosities at saturation temperature individually, $C_{p,d}$ and $C_{p,v}$ are the droplet and vapor specific heat capacities at constant pressure individually, k_d and k_v are the droplet and vapor thermal conductivities at saturation temperature individually, σ is the surface tension.

With all possibly relevant variables are obtained, the most interested variable, which is the wall inner surface superheat $T_w - T_s$, can be described as a function of these variables,

$$T_w - T_s = \mathrm{F}\left(G, q_w^{''}, \Delta i, L_T, D_T, g, i_{v-d}, \rho_d, \rho_v, \mu_d, \mu_v, C_{p,d}, C_{p,v}, k_d, k_v, \sigma\right) \tag{5.2}$$

A theoretical study of the dimensionless analysis by Langhaar (1951) shown that the number of dimensionless products in a complete set is equal to value of the total number of variables minus the rank of their dimensional matrix. Since $\Delta i/i_{v-d}$, L_T/D_T, ρ_d/ρ_v, μ_d/μ_v, $C_{p,d}/C_{p,v}$, k_d/k_v are evidently dimensionless numbers, 6 variables (Δi, L_T, ρ_d, μ_d, $C_{p,d}$,k_d) can be tentatively disregarded. For the dimensions in the field of fluid mechanics and heat transfer, 4 independent units are frequently used, including kg, m, s, and °C. Then the dimensional matrix of variables is shown in the table below,

$$\begin{array}{c|ccccccccccc}
 & T_w - T_s & G & q_w^{''} & i_{v-d} & D_T & g & \rho_v & \mu_v & C_{p,v} & k_v & \sigma \\
\hline
kg & 0 & 1 & 1 & 0 & 0 & 0 & 1 & 1 & 0 & 1 & 1 \\
m & 0 & -2 & 0 & 2 & 1 & 1 & -3 & -1 & 2 & 1 & 0 \\
s & 0 & -1 & -3 & -2 & 0 & -2 & 0 & -1 & -2 & -3 & -2 \\
{}^{\circ}\mathrm{C} & 1 & 0 & 0 & 0 & 0 & 0 & 0 & 0 & -1 & -1 & 0
\end{array}$$

There are 11 variables, and the rank of the matrix is 4. Accordingly, this matrix can produce 7 dimensionless numbers. Thus, there are 13 dimensionless numbers in the complete set, including those 6 tentatively disregarded dimensionless numbers.

Consequently, the function in Eq. (5.2) can be transformed by using Buckingham Pi-theorem in the form of one possible set of π terms,

$$\pi_1 = \mathrm{F}\left(\pi_2, \pi_3, \pi_4, \cdots, \pi_{13}\right) \tag{5.3}$$

where, the π terms are expressed as below,

$\pi_1 =$	$\frac{q_w^{''} D_T}{k_v (T_w - T_s)}$	Nusselt number	$\pi_2 =$	$\frac{q_w^{''}}{G i_{v-d}}$	Boiling number
$\pi_3 =$	$\frac{G D_T}{\mu_v}$	Reynolds number	$\pi_4 =$	$\frac{G^2 D_T}{\rho_d \sigma}$	Weber number
$\pi_5 =$	$\frac{\mu_v C_{p,v}}{k_v}$	Prandtl number	$\pi_6 =$	$\frac{G}{\rho_d \sqrt{g D_T}}$	Froude number
$\pi_7 =$	$\frac{\Delta i}{i_{v-d}}$	Subcooling number	$\pi_8 =$	$\frac{L_T}{D_T}$	Geometric similarity
$\pi_9 =$	$\frac{\rho_d}{\rho_v}$	Density ratio	$\pi_{10} =$	$\frac{k_d}{k_v}$	Thermal conductivity ratio
$\pi_{11} =$	$\frac{\mu_d}{\mu_v}$	Viscosity ratio	$\pi_{12} =$	$\frac{C_{p,d}}{C_{p,v}}$	Specific heat capacity ratio
$\pi_{13} =$	$\frac{G}{\rho_d \sqrt{i_{v-d}}}$	Velocity ratio			

In above dimensionless numbers, π_1 is the dependent dimensionless number that includes the variable of interest $T_w - T_s$, and the remains are called independent dimensionless numbers formed by independent variables. Though there are many different complete sets of dimensionless numbers that can be formed, in the current work, the above group of dimensionless number is chosen on the basis of the following considerations,

- Except the one chosen dependent dimensionless number π_1 - Nusselt number, each independent dimensionless number to the greatest extent includes only one independent variable that can be regulated experimentally. This allows the maximum amount of experimental control over the dimensionless numbers.
- Most of the dimensionless numbers are expressed as classic numbers (e.g. Reynolds, Prandtl, Weber), especially while the numbers have their physical significance in post-dryout flow.

- For the properties used in the dimensionless numbers, all are evaluated at the saturation temperature, and the use of which phase's properties (since same dimensions they have) depends on the dimensionless number's physical meaning. For example, the Reynolds number relates to the intensity of flow, and vapor properties are used because the vapor is the continuous phase with more than 80% volume fraction in the flow.

The dependent dimensionless number involving wall superheat is chosen as Nusselt number, since Nusselt number is the ratio of convective to conductive heat transfer normal to the surface, characterizing the heat transfer in the flow. According to the theorem, the dependent dimensionless number π_1 in the model can equal the same number in the prototype if all those 11 independent dimensionless numbers of the model are equal to the same numbers of the prototype, respectively. Obviously, it is impracticable to satisfy this requirement. A true model that faithfully scales all significant characteristics of the prototype is almost impossible, especially in a two-phase system. Therefore, some independent dimensionless numbers that do not play a significant role in the determination of post-dryout heat transfer would be discarded.

The post-dryout heat transfer could be characterized mainly by the importance of wall-vapor convective heat transfer and non-equilibrium degree. For the convection between wall and vapor, π_3 and π_5 are crucial based on the experience of single phase flow heat transfer. Moreover, the convective heat transfer between wall and vapor in post-dryout flow and non-equilibrium degree are both influenced by the presence of droplets, mainly through the quality x_a, the droplet diameter d, and the droplet trajectories. π_4 can be important in the determination of droplet diameter, which is a crucial variable that not only influences the interfacial heat transfer between vapor and droplets but also influences the wall-droplets direct contact heat transfer. As for π_6, Froude number indicates the influence of the gravity on the post-dryout heat transfer. Though Froude number is sometimes considered in some theoretical models, compared to some other dimensionless numbers (Reynolds number and Weber number) involving mass flux, it is not so crucial since the buoyancy effects are not significant in forced convection. π_9 and π_{11} are frequently used in the empirically derived correlations for post-dryout flow, both numbers influence the inter-phase hydrodynamic behavior, in which π_9 is often used to determine the pressure in the fluid-to-fluid modelling of two-phase system, and the density ratio is also used in previous scaling methods for post-dryout heat transfer, as summarized in section 5.1. As for two other properties ratios π_{10} and π_{12}, the thermal conductivity ratio and the specific heat capacity ratio are functions of temperature, and they don't influence the inter-phase hydrodynamic behavior. Thus these two ratios are assumed relatively unimportant. Besides, rare correlations include these two properties ratios based on literature review. These dimensionless numbers involving mass flux and properties ratios that were considered important in the post-dryout heat transfer are studied in the current work to achieve the hydrodynamic similarity.

The thermodynamic similarity is also required for the fluid-to-fluid modelling of two-phase systems. However, obvious thermal non-equilibrium exists in the post-dryout flow. This makes the scaling for post-dryout heat transfer challenging. As suggested by Groeneveld et al. (1997), the thermodynamic similarity in post-dryout heat transfer can be achieved when equilibrium qualities in both model and prototype facilities are the same at any axial location (L_T/D_T) along with the length. Thus, Groeneveld utilized the Subcooling number π_7 and the Boiling number Bo to keep the thermodynamic similarity. In post-dryout heat transfer, especially under intermediate-to-high pressure and mass flux conditions, the equilibrium quality can be considered as the actual quality. Under low pressure and mass flux conditions, non-equilibrium effects become significant. However, based on some analytical derivations of the relationship between x_a and x_e with some reasonable assumptions which are summarized in Eq. (2.18) and Eq. (2.14), the actual quality x_a is related to the equilibrium quality x_e and some other dimensionless numbers, and the Boiling number Bo is the only one dimensionless number involving heat flux. Therefore, the Boiling number Bo would be used in the current work. As for geometric similarity, equivalent π_8 is a must satisfying requirement. Furthermore, dimensionless number π_{13} represents the ratio of the kinetic energy of the flow to the latent heat. π_{13} can be neglected since this number is very small in typical post-dryout conditions.

Strictly speaking, fluid-to-fluid modelling of post-dryout heat transfer should keep the inlet Subcooling number equal in both model and prototype facilities since the inlet flow conditions can influence the droplets' generation upstream of dryout. However, this kind of scaling from case to case is quite expensive due to that the inlet conditions can vary by using different scaling method, it is not suitable to massively evaluate different scaling methods through this way. In the current work, scaling is performed from point to point between the water based Becker and the R-134a based KIT experiments, and variables are derived by the local flow conditions. The geometric similarity is kept by using identical tubes as suggested by Groeneveld et al. (1997) to eliminate the geometric effect. The thermodynamic similarity is kept by using equivalent equilibrium quality x_e and boiling number Bo. As for the hydrodynamic similarity, the pressure is controlled by using density ratio π_9, and a dimensionless number $\Psi(G)$ involving mass flux can be derived by applying the compensated distortion technique with using the other considered dimensionless numbers, including π_3, π_4, π_5, and π_{11}. Thus, the scaling method can be written as below,

$$\frac{q_w'' D_T}{k_v\left(T_w - T_s\right)} = \mathrm{F}\left(\Psi(G), \frac{q_w''}{G i_{v-d}}, x_e, \frac{\rho_d}{\rho_v}\right) \tag{5.4}$$

where, 5 different forms of $\Psi(G)$ including $\pi_3\pi_4^n$, $\pi_3\pi_5^n$, $\pi_3\pi_{11}^n$, $\pi_4\pi_5^n$, and $\pi_4\pi_{11}^n$, are investigated in the current work to obtain the best fitted constant exponent n for each form.

5.3. Scaling methods optimization procedure

To obtain the best-fitted scaling method, an optimization procedure is used as shown in Figure 5.1. Scaling is performed from point to point by using the method in Eq. 5.4 with different forms of $\Psi(G)$. Details are illustrated as follows,

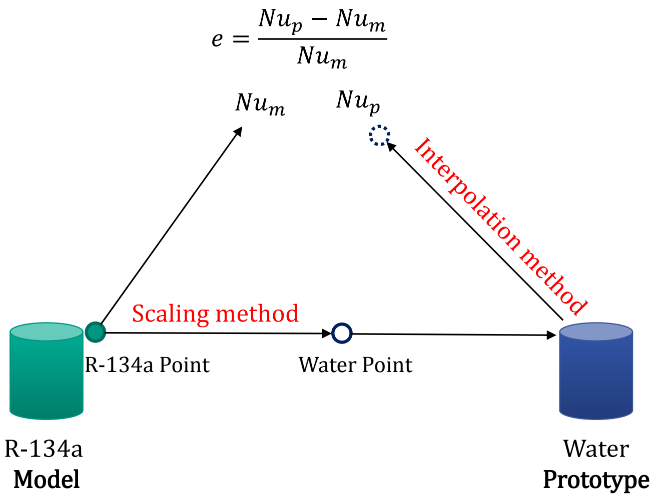

Figure 5.1.: Scaling methods optimization procedure.

First, the Model databank comes from the R-134a based KIT experiment (Köckert et al., 2018). Each data point is obtained in the fully developed post-dryout region with a selection criterion of dryout void fraction $\alpha_{do} > 0.8$. The Prototype databank comes from the water based Becker experiment (Becker et al., 1983). Each data point is also obtained in the fully developed post-dryout region with a selection criterion of dryout void fraction $\alpha_{do} > 0.8$. Then, the parameters of the selected data points are listed in Table 5.1.

Table 5.1.: Information of databank used in optimizing scaling method.

Databank	D_T $[mm]$	Parameters				Points number
		Pressure $[MPa]$	Mass flux $[kg/(m^2 s)]$	Heat flux $[kW/m^2]$	Quality $[-]$	
KIT	10	1.1, 1.6, 2.8	300-1500	30-140	0.28-1.76	1820
Becker	10, 14.9	3-16	500-3100	147-1295	0.3-1.35	2930

Secondly, 5 different forms of $\Psi(G)$, including $\pi_3\pi_4^n$, $\pi_3\pi_5^n$, $\pi_3\pi_{11}^n$, $\pi_4\pi_5^n$, and $\pi_4\pi_{11}^n$, are used to scale the mass flux separately. For each form of $\Psi(G)$, the constant exponent n is tested from -2 to 2 with an interval of 0.1. For each constant exponent n, the equation (5.4) can be fixed as one scaling method. For each scaling method, every data point in the Model databank is scaled through this method to water conditions. The Nu_m is the dependent Pi term π_1 of the data point in the Model databank. Since the water data point obtained through the scaling method cannot be well matched in the Prototype databank, an interpolation method should be used to determine its actual dependent Pi term π_1, which is named Nu_p.

Lastly, an error e is defined as $e = (Nu_p - Nu_m)/Nu_m$, representing the accuracy of the scaling. The average e and RMS e of all the data points can be used to evaluate the applied scaling method, under the circumstance of that the interpolation method can provide an accurate value of Nu_p.

5.4. Interpolation method

To massively evaluate the fluid-to-fluid scaling methods, an interpolation method is required to make the optimization procedure possible. The sparsity of the databank and performance of the interpolation method determine the quality of the evaluation of the scaling methods. In the current work, the interpolation is performed with Becker databank, in which the flow parameters (e.g. mass flux, heat flux, pressure) intervals are not small. Thus, an effective interpolation method is required to give an accurate prediction of Nu_p.

Badea et al. (2018) developed a procedure to assess the intrinsic consistency of the experimental information (values of Nusselt number at the bulk Nu_{vb}) contained in the databank for supercritical water in circular tubes. The procedure was based on the assumption that the ratio of Nusselt number value at point i to the value calculated by the local optimal correlation is equal to that ratio which is obtained from its neighboring data point j. The relation can be described as below,

$$\frac{Nu_i}{Nu_{i,oc}} = \frac{Nu_j}{Nu_{j,oc}} \tag{5.5}$$

where, Nu_i and Nu_j are the values of Nusselt number at point i and j, respectively. $Nu_{i,oc}$ and $Nu_{j,oc}$ are the values of Nusselt number at point i and j, which are calculated by the local optimal correlation, respectively.

Based on this assumption, the interpolation method used for post-dryout heat transfer databank is developed with following procedures,

- **(a) determination of neighboring data points**

  The data points in post-dryout heat transfer can be considered as neighboring points if differences of all the parameters are within a small range receptively. In the current work, the tube diameter D_T and the local flow parameters including pressure P, mass flux G, wall heat flux $q_w^{''}$, and equilibrium quality x_e are used to define a data point. Therefore, for data point i, the criterion to determine its neighboring data points is proposed as below,

  $$\begin{aligned} |D_{T,i} - D_{T,j}| &\leq C \bullet 6 \quad [mm] \\ |P_i - P_j| &\leq C \bullet 0.5 \quad [MPa] \\ |G_i - G_j| &\leq C \bullet 250 \quad [kg/(m^2 s)] \\ \left|q_{w,i}^{''} - q_{w,j}^{''}\right| &\leq C \bullet 100 \quad [kW/m^2] \\ |x_{e,i} - x_{e,j}| &\leq C \bullet 0.05 \quad [-] \end{aligned}$$

  For this interpretation method, if a data point is closer to the data point of interest, the assumption in Eq. (5.5) is more likely to be correct. However, if only one data point is selected to speculate the actual Nu_i of the data point of interest, the systematic error that caused by this assumption can not be compensated. Thus, a coefficient C is applied, decreasing from 1 to 0 until around n neighboring points are found. In the current work, the number n is chosen equal to 4.

- **(b) calculating Nusselt number**

  While the neighboring points are found, two post-dryout heat transfer models including the proposed model and the LCS can be used to calculate the predicted $Nu_{j,oc}$ of each neighboring point respectively. The prediction error by model is defined as below,

  $$e_j = \frac{Nu_{j,oc} - Nu_j}{Nu_j}; \quad j = 1, 2, 3, 4, \cdots n \tag{5.6}$$

  where, n is the number of found neighboring data points. Compared the two RMS errors which were individually calculated by the proposed model and the LCS, the model that has smaller RMS error is considered as the local optimal correlation.

  Finally, a mean value of Nusselt number $\overline{Nu_i}$ can be obtained as following,

  $$\overline{Nu_i} = \frac{\sum_{j=1}^{n} Nu_j \frac{Nu_{i,oc}}{Nu_{j,oc}}}{n} \tag{5.7}$$

  The mean value $\overline{Nu_i}$ is considered as the actual Nusselt number of the interested point i.

To assess this interpolation method, each data point in the Prototype databank is selected and calculated by applying this interpolation method on the remaining data points. A sensitivity study is implemented on the influence of the utilized number of neighboring data points n on the accuracy of the interpolation method. As shown in Figure 5.2, the assessment results are plotted against the number of neighboring points n. The value of n varies from 1 to 14, the average error remains close to 0, and the RMS error is slightly increasing but is less than 5%. Finally, n is chosen equal to 4 in the current work. The assessment shows that the average error is -0.149%, and the RMS error is 3.786%. As shown in Figure 5.3, the accuracy of most of the data points are within a range of ±3%.

Though this assessment only guarantees the accuracy of the interpolation method that was used in the flow conditions of the Prototype databank, it can generally reflect the reliability while the method is applied within the whole range of the flow conditions. With increasing the density of the points in the databank, this assessment would be more credible to testify the accuracy of the interpolation method in the optimization procedure.

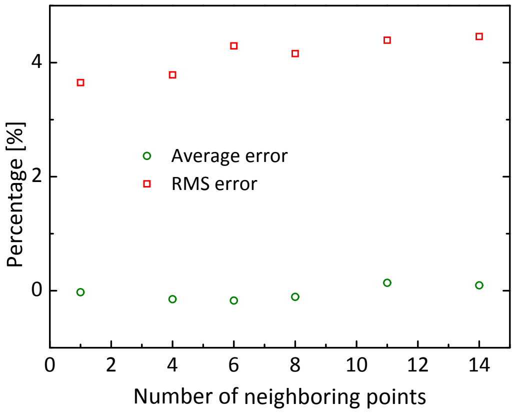

Figure 5.2.: Assessment results versus the number of neighboring points n.

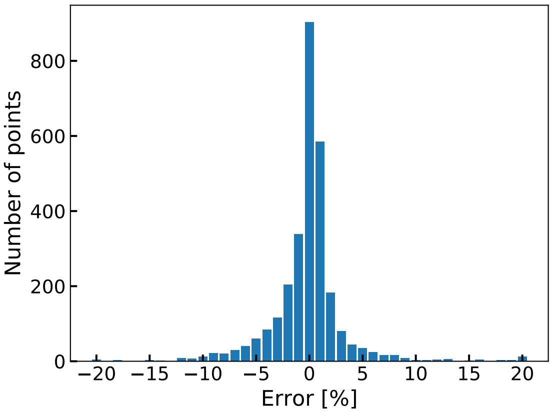

Figure 5.3.: Error distribution of the assessment with n is 4.

5.5. Scaling methods optimization results

As described in section 5.3, the scaling methods optimization procedure is performed from point to point by using the method in Eq. 5.4 with 5 different forms of $\Psi(G)$. The optimizing matrix is shown in Table 5.2.

Table 5.2.: Information of the scaling methods optimizing matrix.

Name	$\Psi(G)$
SM1	$\left(\frac{GD_T}{\mu_v}\right)\left(\frac{G^2D_T}{\rho_d\sigma}\right)^n$
SM2	$\left(\frac{GD_T}{\mu_v}\right)\left(\frac{\mu_vC_{p,v}}{k_v}\right)^n$
SM3	$\left(\frac{GD_T}{\mu_v}\right)\left(\frac{\mu_d}{\mu_v}\right)^n$
SM4	$\left(\frac{G^2D_T}{\rho_d\sigma}\right)\left(\frac{\mu_vC_{p,v}}{k_v}\right)^n$
SM5	$\left(\frac{G^2D_T}{\rho_d\sigma}\right)\left(\frac{\mu_d}{\mu_v}\right)^n$

For each form of the scaling methods, the constant exponent n is tested from -2 to 2 with an interval of 0.1. Optimization results are shown in Figure 5.4, where the error is defined as $e = (Nu_p - Nu_m)/Nu_m$. For form SM1, the RMS error varies very fast while n is close to the value of -0.5, which would vanish the mass flux G in the dimensionless number $\Psi(G)$. The best-fitted value of n can be selected as 0.4, where the RMS error is nearly the smallest, and the value is not sensitive when n is around 0.4. For form SM2,

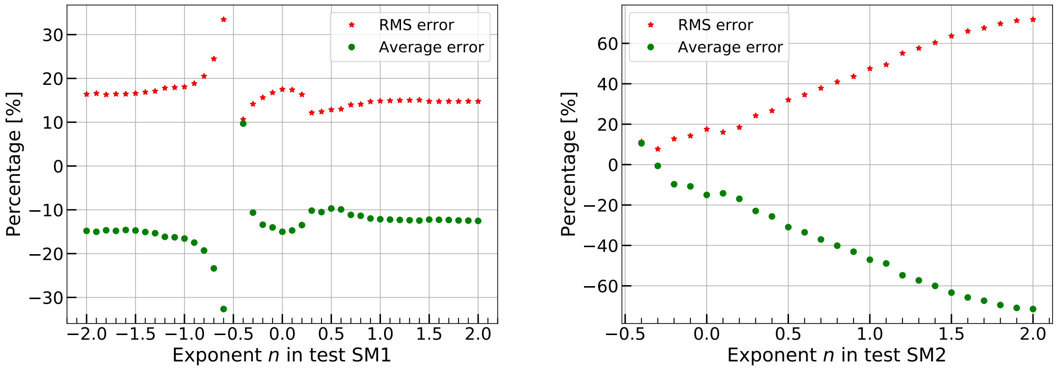

(a) SM1 (b) SM2

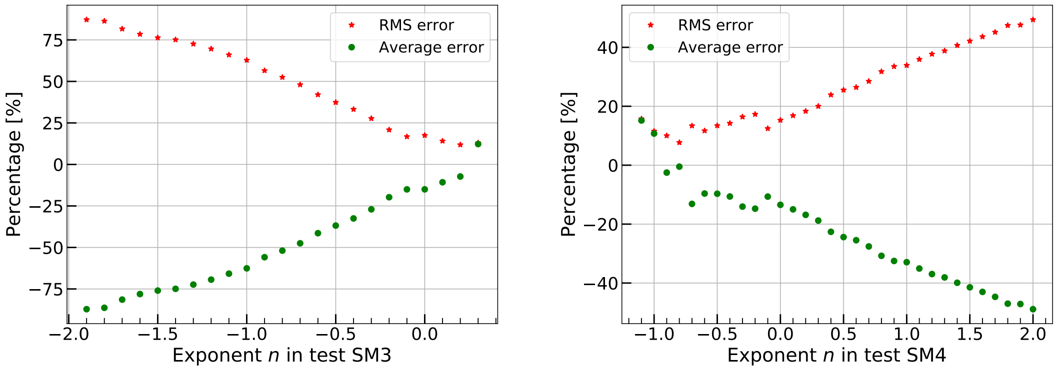

(c) SM3 (d) SM4

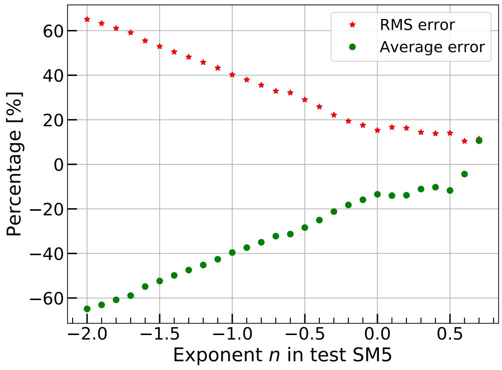

(e) SM5

Figure 5.4.: Optimization results of each form of the scaling methods.

after each data point in the Model databank scaled by the scaling method with n less than -0.4, no neighboring data points can be found in the Prototype databank. The best-fitted value of n for SM2 can be selected as -0.3. For form SM3, while n is more than 0.3, no neighboring data points can be found. The best fitted n for SM3 can be selected as 0.2. For form SM4, while n is less than -1.1, no neighboring data points can be found. The best fitted n for SM4 can be selected as -0.8. For form SM5, while n is greater than 0.7, no neighboring data points can be found. The best fitted n for SM5 can be selected as 0.6. The average and RMS errors of each form of the scaling methods with fitted values of n are listed in Table 5.3. If merely based on the RMS errors, the optimized SM2 and

SM4 perform the best, SM1 performs the worst.

Table 5.3.: Results of the average and RMS errors of each form of the scaling methods with fitted n.

Name	$\Psi(G)$	Fitted n	Average error	RMS error
SM1	$\left(\frac{GD_T}{\mu_v}\right)\left(\frac{G^2D_T}{\rho_d\sigma}\right)^n$	0.4	-0.105	0.124
SM2	$\left(\frac{GD_T}{\mu_v}\right)\left(\frac{\mu_v C_{p,v}}{k_v}\right)^n$	-0.3	-0.006	0.077
SM3	$\left(\frac{GD_T}{\mu_v}\right)\left(\frac{\mu_d}{\mu_v}\right)^n$	0.2	-0.073	0.118
SM4	$\left(\frac{G^2D_T}{\rho_d\sigma}\right)\left(\frac{\mu_v C_{p,v}}{k_v}\right)^n$	-0.8	-0.005	0.077
SM5	$\left(\frac{G^2D_T}{\rho_d\sigma}\right)\left(\frac{\mu_d}{\mu_v}\right)^n$	0.6	-0.044	0.104

Table 5.4.: Scaling ratios R_S of heat flux, mass flux, and pressure for each form of the scaling methods.

Name	Heat flux R_S	Mass flux R_S	Pressure R_S
SM1	0.072	0.682	0.16
SM2	0.060	0.566	0.16
SM3	0.058	0.553	0.16
SM4	0.060	0.567	0.16
SM5	0.056	0.532	0.16

A flow condition in Prototype is chosen as pressure $P = 7MPa$, mass flux $G = 2600kg/(m^2s)$, heat flux $q_w^{''} = 1500\ kW/m^2$, and diameter $D_T = 12.6\ mm$ to investigate the scaling ratio R_S of each form of the scaling methods. R_S is defined as below,

$$R_S = \frac{value\ in\ \textbf{Model}}{value\ in\ \textbf{Prototype}} \tag{5.8}$$

Results are listed in Table 5.4, the optimized SM5 scaling method has the best scaling ratio, which can reduce the cost and technical difficulties of implementing the post-dryout experiments.

5.6. Assessment of each form of the optimized scaling methods

Table 5.5.: Parameters of tests for assessment of the optimized scaling methods.

Test Id	Databank	Tube diameter $[mm]$	Pressure $[MPa]$	Mass flux $[kg/(m^2s)]$	Heat flux $[kW/m^2]$
Case1	Bennett et al. (1968)	12.6	7.0	2600	1500
Case2	Bennett et al. (1968)	12.6	7.0	2000	1100
Case3	Bennett et al. (1968)	12.6	7.0	1950	1500
Case4	Bennett et al. (1968)	12.6	7.0	394	545
Case5	Bennett et al. (1968)	12.6	7.0	1360	970
Case6	Bennett et al. (1968)	12.6	7.0	650	582
Case7	Era et al. (1966)	6.0	7.0	2200	1100
Case8	Era et al. (1966)	6.0	7.0	1100	500

Assessments of each form of the optimized scaling methods are performed point-to-point from Prototype data to Model data. Figure 5.5 and Figure 5.6 show the assessments results

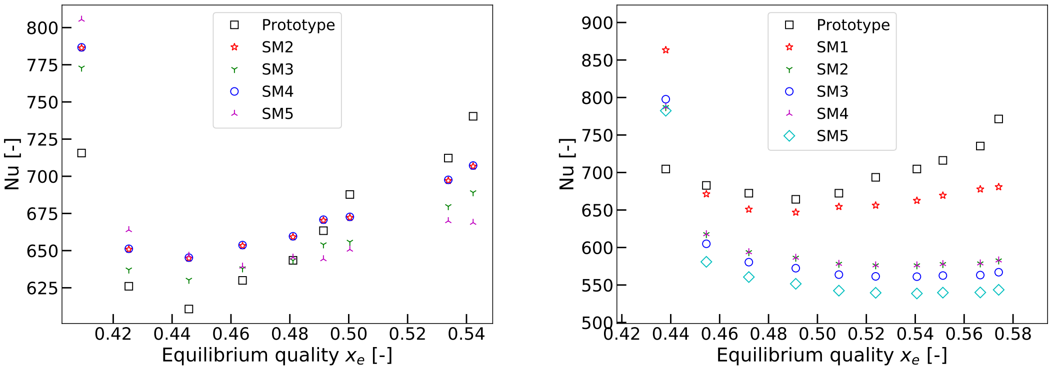

(a) Case1 (b) Case2

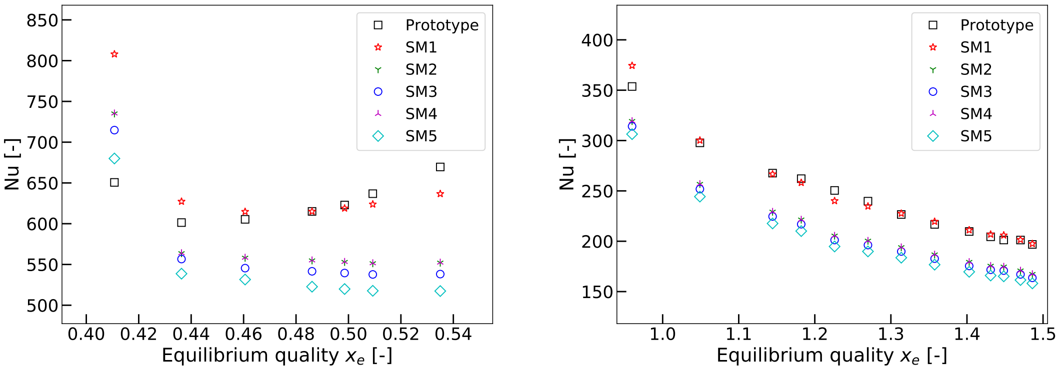

(c) Case3 (d) Case4

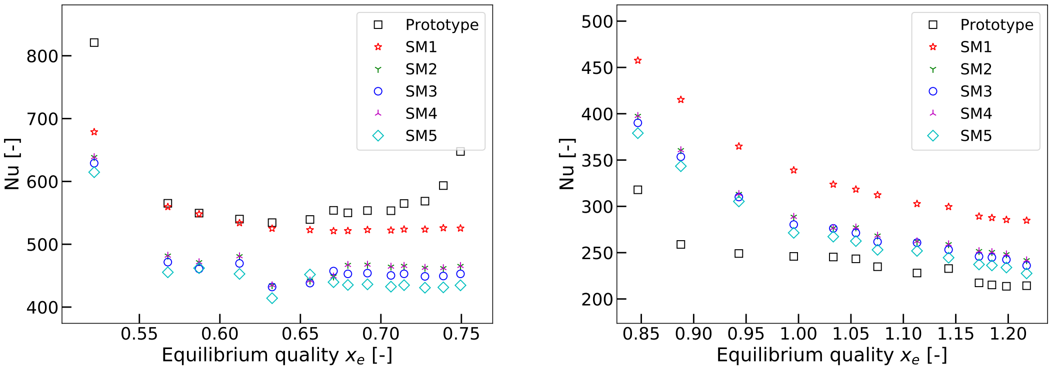

(e) Case5 (f) Case6

Figure 5.5.: Assessments of the optimized scaling methods with Prototype data from Bennett et al. (1968).

by using 6 cases from Bennett et al. (1968) and 2 cases from Era et al. (1966), respectively. The cases are scaled by each scaling method point-to-point to R-134a conditions, and Nusselt number in Model Nu_m is obtained by using the proposed interpolation method with the KIT databank. Information of each case are listed in Table 5.5.

In Case1 as shown in Figure 5.5(a), there are no neighboring points found in the KIT databank for the scaling by using method SM1. Results show the optimized methods SM2 and SM4 perform the best in this case, and their predictions are almost the same.

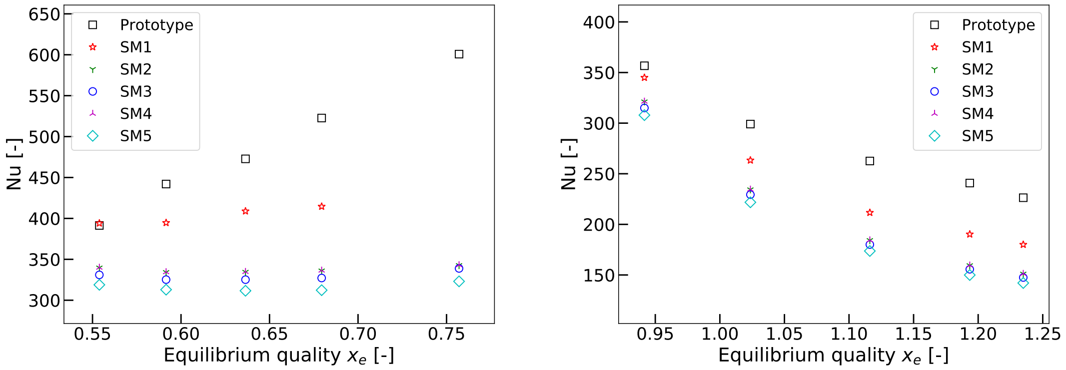

(a) Case7 (b) Case8

Figure 5.6.: Assessments of the optimized scaling methods with Prototype data from Era et al. (1966).

For Case2, Case3, Case4, and Case5, method SM1 performs the best and has excellent agreement with the Prototype data. For Case6, methods SM2, SM3, SM4, and SM5 predict very similar results, and SM1 performs obviously worse than the others. For Case7 and Case8, method SM1 predicts better than the others, and assessments in these two cases show worse accuracy of the scaling methods than the 6 cases from Bennett et al. (1968).

To sum up, though very limited cases are used to assess the optimized scaling methods, the results show that the optimized methods SM2 and SM4 always give very similar predictions. In most cases, SM1 can give better agreement with Prototype data than the other scaling methods, but in some particular cases, it also can give worse predictions than the other methods. All methods give worse predictions for Era et al. (1966) than for Bennett et al. (1968) under similar flow conditions. This could be due to the tube diameter in Era et al. (1966) experiment is small, the scaling method or the interpolation method is not effective while the diameter is far from that of the databank, which in this assessment tests is 10 mm for the KIT databank.

5.7. Conclusion

In this chapter, fluid-to-fluid modelling of post-dryout heat transfer between R-134a and water is studied. Scaling methods are developed based on dimensional analyses by using Buckingham Pi-theorem. The work starts from deriving dimensionless numbers, selecting dimensionless numbers by their significance to post-dryout heat transfer, and then 5 different forms of scaling methods are evaluated through an optimization procedure, in which a proposed interpolation method is used. The interpolation method is necessary for such massive scaling between two databanks and assessed by verifying the data in the Prototype databank itself. Finally, for each form of the scaling methods, a fitted dimensionless number $\Psi(G)$ involving mass flux can be obtained. For each form of the scaling methods with fitted $\Psi(G)$, assessments are implemented point-to-point from Prototype data to Model data. Prototype data makes use of 6 cases from Bennett et al. (1968) and 2 cases from Era et al. (1966). Model data makes use of KIT databank from Köckert et al. (2018).

Merely from the obtained results in the current work, the optimized SM1 can be selected as the best scaling method, which in final form can be expressed as,

$$\frac{q_w'' D_T}{k_v\left(T_w - T_s\right)} = \mathrm{F}\left(\left(\frac{GD_T}{\mu_v}\right)\cdot\left(\frac{G^2 D_T}{\rho_d \sigma}\right)^{0.4}, \frac{q_w''}{Gi_{v-d}}, x_e, \frac{\rho_d}{\rho_v}\right) \tag{5.9}$$

All the properties are evaluated at saturation temperature.

Moreover, this scaling method is not verified under a wide range of flow conditions since sometimes no neighboring data points can be found by using this scaling method. The accuracy of the interpolation method while in the use of optimizing the scaling methods is also not directly assessed. Besides, as indicated at the beginning, the near-wall fluid properties cannot be taken into consideration in the scaling method since the heat flux controlled system is focused. This could probably limit the optimized method SM1 into a small application range, where the wall superheat cannot be too high. Thus, the performance of scaling method SM1 is not guaranteed so far until further work can be implemented through the same optimization procedure but with using data points that are generated in two identical tubes and a wide range of flow conditions for both R-134a and water.

6. Summary and outlook

Due to the complex phenomena, experimental studies on post-dryout heat transfer and its predicting method development have been conducted for over sixty years. The developed models for post-dryout heat transfer range from simple equilibrium correlations to complex multidimensional mechanistic models. Each kind of approach presents merits and limitations in the modelling of post-dryout heat transfer. In the current work, a general theoretical model, as well as scaling methods for full-range post-dryout heat transfer in vertical tubes, is developed and assessed. The most important original works and conclusions are summarized below:

original works

- Definition of terms *developing post-dryout region* and *fully developed post-dryout region* is proposed to distinguish these two regions. Moreover, the determination equation for the developing region length L_{dev} is developed, as shown in Eq. (3.5).
- In the proposed model, for considering the impacts of the droplets' concentration distribution over the cross-section on the interfacial heat transfer between vapor and droplets, the flow region is divided into a film region and a core region, which are characterized by the film and core vapor temperatures T_{vf}, T_{vc}, respectively.
- For fluid-to-fluid modelling of post-dryout heat transfer, a new interpolation method is developed to make it possible to evaluate fluid-to-fluid scaling methods by using Model and Prototype databank. After assessed by some tests, the scaling method for fluid-to-fluid modelling of post-dryout heat transfer is proposed as in Eq. (5.9).

conclusions

- The proposed model is vastly assessed and mainly by comparing to four existing post-dryout heat transfer models including GRO, CSO, LCS, and ATHLET, and three experiments including two uniform axial heat flux Becker and KIT experiments and one non-uniform axial heat flux BeckerII experiment. The proposed model generally underestimates the Becker experimental HTC by 13.82% with an RMS error of 20.05%, overestimates the KIT experimental HTC by 6.86% with an RMS error of 10.32%, and underestimates the BeckerII experimental HTC by 6.74% with an RMS error of 17.65%, in the fully developed post-dryout region. Thus the proposed model can be used for various fluids, wide ranges of flow conditions, and uniform and non-uniform axial heat flux conditions. The accuracy of predicting the developing region length is assessed by comparison with 187 points from Becker, 125 points from KIT, 30 points from the literature listed in Table B, and 734 points from BeckerII. The results indicate that the proposed model can provide good predictions.

- Performances of the proposed model under different conditions of pressures, flow qualities, non-equilibrium degrees, and tube diameters are also evaluated. The proposed model can generally well predict the wall superheat profiles but sometimes overestimates or underestimates for some certain flow conditions and type of fluid. The reason is due to the usage of the modified Forslund correlation for convective heat transfer between wall and vapor. Though the correlation generally can provide good prediction in different fluids and wide ranges of flow conditions, it does not include the impacts on the convective heat transfer between wall and vapor, which is due to the presence of evaporating droplets.
- The contribution of direct contact heat transfer between wall and droplets is analyzed, and this part of heat transfer is found to be more significant in the developing post-dryout region than it in the fully developed region. Besides, the direct contact heat transfer contributes much more significantly under high pressures than at low pressures. It can be concluded that the direct contact heat transfer between wall and droplets could be neglected in most of the conditions with low pressures.
- For all conditions of 5 different axial wall heat flux profiles including inlet peak, middle peak, outlet peak, narrow middle peak and narrow inlet peak, the wall superheat is found increasing very slowly in the developing region while the pressure is high and wall superheat is low. The proposed model can obviously overestimate the wall superheat for such cases. It is explained that the wall surface can be wetted in such conditions and the wet contact heat transfer between wall and droplets contributes more, or the proposed model underestimates the wall-droplets contact heat transfer for such conditions, or both the former two reasons.
- Fluid-to-fluid modelling of post-dryout heat transfer between R-134a and water is studied. The developed scaling methods optimization procedure, including the proposed interpolation method, is effective. The fitted scaling method SM1 is eventually proposed in Eq. (5.9) with assessments by a few tests. However, this scaling method is not assessed under a wide range of flow conditions. Especially, the performance of the proposed scaling method SM1 is not guaranteed under the conditions where the wall superheat is high. Moreover, the accuracy of the interpolation method, while in the use of optimizing scaling methods, is not assessed directly.

Though some achievements have been made in the present work on the aspects of both the theoretical modelling and the fluid-to-fluid modelling for post-dryout heat transfer, some deficiencies remain still and can be expected in the future work:

- Convective heat transfer correlation between wall and vapor with consideration of impacts due to the presence of droplets can be developed for various fluids. The developed weighting factor K_2 in Eq. (3.42) can be improved, especially on the aspects of considering influence from the type of fluid and the tube diameter.
- The scaling method can be verified and improved through the same optimization procedure but with using data points generated in two identical tubes and a wide range of flow conditions for both R-134a and water. Another approach for scaling can be carried out, in which the wall temperature is considered as a controlled variable since properties variation over the cross-section of the flow influences post-dryout heat transfer greatly.
- The proposed model can be improved for conditions where wet contact between wall and droplets is present due to the low wall superheat.

A. List of previous non-equilibrium models and correlations

The following are summarized non-equilibrium models and correlations in the past for post-dryout heat transfer, including works from Forslund and Rohsenow (1968), Groeneveld and Delorme (1976), Chen et al. (1979), Saha (1980), Webb and Chen (1982), Moose and Ganić (1982), Yoder and Rohsenow (1983), Chung and Olafsson (1984), Nishikawa et al. (1986), Varone and Rohsenow (1986), Rohsenow (1988), Varone (1990), Jeong and No (1996), Andreani and Yadigaroglu (1997), Shah and Siddiqui (2000), Guo and Mishima (2002), Keizo et al. (2005), Meholic (2011), Torfeh and Kouhikamali (2015), Li and Anglart (2016), and Cheng et al. (2018).

Table A.1.: Review of previous theoretical models without equilibrium correlations.

Theoretical Models and Correlations for PDO in Vertical Tube (exclude the equlibrium correlations)

x: didn't consider
o: considered

*Scheme of Heat Transfer : Ⅰ: wall to vapor
Ⅱ: Ⅰ + vapor to droplets
Ⅲ: Ⅰ +Ⅱ+ wall to droplets

Characteristics Authors	Year	1. Dimensions (1D; 2D; 3D)	2. Flow Structure (h- homogeneous; dv- separate)	3. Scheme of Heat Transfer*	4. Thermal Radiation	5. Droplet Hydrodynamics			
						deposition of droplets	axial size distribution	radial distribution	impacts on vapor
Forslund and Rohsenow	1968	1D	dv	Ⅲ	x	o	o	x	x
Groeneveld and Delorme	1976	1D	h	Ⅰ	x	x	x	x	x
Kendall and Rohsenow	1978	2D	dv	Ⅲ	x	o	o	o	x
Chen et al.	1979	1D	dv	Ⅱ	x	x	x	x	x
Saha	1980	1D	dv	Ⅱ	x	x	o	x	x
Webb and Chen	1982	2D vapor + 1D drop	dv	Ⅲ	o	x	o	x	o
Moose and Ganić	1982	1D	dv	Ⅲ	x	o	o	x	x
Yoder and Rohsenow	1983	1D	dv	Ⅱ	x	x	o	x	x
Chung and Olafsson	1984	2D vapor + 1D drop	dv	Ⅲ	o	x	o	x	o
Nishikawa et al.	1983	1D	dv	Ⅱ	x	x	o	x	x
Varone and Rohsenow	1986	1D	dv	Ⅲ	x	o	o	x	o
Varone	1990	1D	dv	Ⅲ	x	o	o	x	o
Jeong and No	1996	1D	dv	Ⅱ	x	x	o	x	x
Andreani and Yadigaroglu	1997	2D vapor + 3D drop	dv	Ⅲ	o	o	o	o	o
Shah and Siddiqui	2000	1D	dv	Ⅲ	x	o	x	x	x
Guo and Mishima	2002	1D	dv	Ⅲ	o	o	o	o	x
Keizo et al.	2005	2D vapor + 3D drop	dv	Ⅲ	o	o	o	o	o
Meholic	2011	2D	dv	Ⅲ	o	o	o	x	o
Torfeh and Kouhikamali	2015	3D	dv	Ⅱ	x	x	o	o	o
Li and Anglart	2016	3D	dv	Ⅲ	x	o	o	o	o
Cheng et al.	2018	1D	dv	Ⅲ	x	o	o	x	x

B. List of data from literature for prediction of L_{dev}

A list of data comes from literature Bennett et al. (1968), Era et al. (1966), Cumo et al. (1974), Groeneveld (1972), and Nishikawa et al. (1983). Parameters of these data and the prediction results by the proposed model are listed in Table B.1.

Table B.1.: Parameters of data and prediction results of L_{dev}.

Data	P $[MPa]$	D_T $[mm]$	G $[kg/(m^2s)]$	q_w'' $[kW/m^2]$	Measured L_{dev} $[-]$	Predicted L_{dev} $[-]$	error
Bennett, water	7.0	12.6	2600.0	1500.0	0.045	0.057	0.27
Bennett, water	7.0	12.6	2200.0	1500.0	0.07	0.067	-0.039
Bennett, water	7.0	12.6	2000.0	1100.0	0.058	0.056	-0.017
Bennett, water	7.0	12.6	1950.0	1500.0	0.04	0.074	0.848
Bennett, water	7.0	12.6	394.0	545.0	0.145	0.142	-0.025
Bennett, water	7.0	12.6	1360.0	970.0	0.12	0.072	-0.397
Bennett, water	7.0	12.6	3800.0	1700.0	0.047	0.046	-0.02
Bennett, water	7.0	12.6	650.0	852.0	0.138	0.13	-0.059
Bennett, water	7.0	12.6	1020.0	925.0	0.095	0.09	-0.05
Bennett, water	7.0	12.6	1950.0	1500.0	0.048	0.074	0.54
Bennett, water	7.0	12.6	2600.0	1600.0	0.038	0.061	0.566

Bennett, water	7.0	12.6	2600.0	1200.0	0.034	0.048	0.431
Era, water	7.0	6.0	2200.0	925.0	0.08	0.048	-0.388
Era, water	7.0	6.0	2200.0	850.0	0.05	0.046	-0.079
Era, water	7.0	6.0	2200.0	720.0	0.08	0.04	-0.488
Era, water	7.0	6.0	2200.0	630.0	0.08	0.037	-0.532
Era, water	7.0	6.0	2200.0	1500.0	0.1	0.071	-0.286
Era, water	7.0	6.0	2200.0	1300.0	0.08	0.063	-0.205
Era, water	7.0	6.0	2200.0	1100.0	0.08	0.055	-0.303
Era, water	7.0	6.0	2200.0	1000.0	0.08	0.051	-0.351
Era, water	7.0	6.0	2200.0	500.0	0.08	0.032	-0.595
Era, water	7.0	6.0	3000.0	730.0	0.05	0.032	-0.341
Era, water	7.0	6.0	1100.0	500.0	0.06	0.054	-0.086
Cumo, R-12	2.0	4.75	1200.0	100.0	0.1	0.094	-0.053
Cumo, R-12	2.0	4.75	840.0	104.0	0.2	0.139	-0.302
GRO, R-12	1.1	7.8	660.0	124.0	0.107	0.128	0.195
GRO, R-12	1.1	7.8	2032.0	132.0	0.031	0.045	0.425
GRO, R-12	1.1	7.8	2713.0	290.0	0.06	0.068	0.137
Nishikawa, R-22	3.4	9.0	400.0	20.0	0.109	0.091	-0.167
Nishikawa, R-22	3.4	9.0	1000.0	40.0	0.089	0.071	-0.208

Bibliography

C Adamsson and H Anglart. Influence of axial power distribution on dryout: Film-flow models and experiments. *Nuclear Engineering and Design*, 240(6):1495–1505, 2010.

SY Ahmad. Axial distribution of bulk temperature and void fraction in a heated channel with inlet subcooling. *Journal of Heat Transfer*, 92(4):595–609, 1970.

SY Ahmad. Fluid to fluid modeling of critical heat flux: a compensated distortion model. *International Journal of Heat and Mass Transfer*, 16(3):641–662, 1973.

M Andreani and G Yadigaroglu. Dispersed flow film boiling: an investigation of the possibility to improve the models implemented in the nrc computer codes for the reflooding phase of the loca. Technical Report NUREG/IA-0042, PSI, 1989.

M Andreani and G Yadigaroglu. A 3-d eulerian-lagrangian model of dispersed flow film boiling including a mechanistic description of the droplet spectrum evolution-i. the thermal-hydraulic model. *International journal of heat and mass transfer*, 40(8):1753–1772, 1997.

IG Anghel, H Anglart, and S Hedberg. Experimental investigation of post-dryout heat transfer in annuli with flow obstacles. *Nuclear Engineering and Design*, 246:82–90, 2012.

A Annunziato, M Cumo, and G Pallazzi. Post dry-out heat transfer in uncovered core accidents. In *Thermal hydraulics of nuclear reactors.* international topical meeting on nuclear reactor thermal hydraulics (ANS); Santa Barbara, CA (USA), 1983.

H Austregesilo, C Bals, A Hora, G Lerchl, P Romstedt, P Schöffel, D Von der Cron, and F Weyermann. Athlet mod 3.0 cycle a: Models and methods. Technical Report GRS-P-1 Vol. 3, Gesellschaft für Anlagen- und Reaktorsicherheit (GRS), 2012.

AF Badea, M Zhao, X Cheng, F Feuerstein, and XJ Liu. Consistency considerations on a large databank and wide range heat transfer prediction for supercritical water in circular tubes. *Nuclear Engineering and Design*, 335:178–185, 2018.

KJ Baumeister, TD Hamill, GJ Schoessow, and FL Schwartz. Film boiling heat transfer to water drops on a flat plate. Technical Report NASA TMX-52103, National Aeronautics and Space Administration · Washington, D.C., 1965.

KM Becker, CH Ling, S Hedberg, and G Strand. An experimental investigation of post dryout heat transfer. Technical Report KTH-NEL-33, Royal Inst. of Tech., 1983.

KM Becker, A Enerholm, L Sardh, W Köhler, W Kastner, and W Krätzer. Heat transfer in an evaporator tube with circumferentially non-uniform heating. *International journal of multiphase flow*, 14(5):575–586, 1988.

KM Becker, P Askeljung, S Hedberg, B Soderquist, and U Kahlbom. An experimental investigation of the influence of axial heat flux distributions on post dryout heat transfer for flow of water in vertical tubes. *Department of Nuclear Reactor Engineering, Royal Institute of Technology Report KTH-NEL-54, Stockholm, Sweden*, 1992.

AW Bennett, GF Hewitt, HA Kearsey, and RKF Keeys. Heat transfer to steam–water mixtures flowing in uniformly heated tubes in which the critical heat flux has been exceeded. Technical Report REP/AERE-R-5373, Atomic Energy Research Establishment, Harwell, Eng., 1968.

E Buckingham. On physically similar systems; illustrations of the use of dimensional equations. *Physical review*, 4(4):345, 1914.

AD Burns, T Frank, I Hamill, JM Shi, et al. The favre averaged drag model for turbulent dispersion in eulerian multi-phase flows. In *5th international conference on multiphase flow, ICMF*, volume 4, pages 1–17, 2004.

JC Chen. Correlation for boiling heat transfer to saturated fluids in convective flow. *Industrial and engineering chemistry process design and development*, 5(3):322–329, 1966.

JC Chen. Some phenomenological questions in post-critical-flux heat transfer. In *Advances in Two-Phase Flow and Heat Transfer*, pages 239–254. Springer, 1983.

JC Chen. A short review of dispersed flow heat transfer in post-dryout boiling. *Nuclear Engineering and Design*, 95:375–383, 1986.

JC Chen, FT Ozkaynak, and RK Sundaram. Vapor heat transfer in post-chf region including the effect of thermodynamic non-equilibrium. *Nuclear Engineering and Design*, 51(2):143–155, 1979.

X Cheng, F Feuerstein, D Klingel, and DL Yu. Mechanistic prediction of post dryout heat transfer and rewetting. *Kerntechnik*, 83(3):203–207, 2018.

JH Chun, WJ Lee, C Park, and UC Lee. Development of the critical film thickness correlation for an advanced annular film mechanistic dryout model applicable to mars code. *Nuclear engineering and design*, 223(3):315–328, 2003.

JN Chung and SI Olafsson. Two-phase droplet flow convective and radiative heat transfer. *International journal of heat and mass transfer*, 27(6):901–910, 1984.

AF Cokmez-Tuzla, K Tuzla, and JC Chen. Experimental assessment of liquid-wall contacts in post-chf convective boiling. *Nuclear engineering and design*, 139(1):97–103, 1993.

M Cumo, GE Farello, G Ferrari, and G Palazzi. On two-phase highly dispersed flows. *Journal of Heat Transfer*, 96(4):496–503, 1974.

RS Dougall. *Film boiling on the inside of vertical tubes with upward flow of the fluid at low qualities*. PhD thesis, Massachusetts Institute of Technology, 1963.

A Era, GP Gaspari, A Hassid, A Milani, and R Zavattarelli. Heat transfer data in the liquid deficient region for steam-water mixtures at 70 kg/cm^2 flowing in tubular and annular conduits. Technical Report No. 11, Centro Informazioni Studi Esperienze, Italy, 1966.

DG Evans, SW Webb, and JC Chen. Measurements of axially varying non-equilibrium in post critical-heat-flux boiling in a vertical tube. Technical Report NUREG/CR-3363, Lehigh Univ., USA. Inst. of Thermo-Fluid Engineering and Science, 1983.

RP Forslund and WM Rohsenow. Thermal non-equilibrium in dispersed flow film boiling in a vertical tube. Technical Report 75312-44, Cambridge, Mass.: MIT Dept. of Mechanical Engineering, 1966.

RP Forslund and WM Rohsenow. Dispersed flow film boiling. *Journal of Heat Transfer*, 90(4):399–407, 1968.

EN Ganić and WM Rohsenow. Dispersed flow heat transfer. *International Journal of Heat and Mass Transfer*, 20(8):855–866, 1977.

EN Ganić and WM Rohsenow. On the mechanism of liquid drop deposition in two-phase dispersed flow. *Journal of Heat Transfer*, 101(2):288–294, 1979.

V Gnielinski. New equations for heat and mass transfer in turbulent pipe and channel flow. *Int. Chem. Eng.*, 16(2):359–368, 1976.

RC Gottula, RA Nelson, JC Chen, S Neti, and RK Sundaram. Forced-convective nonequilibrium post-chf heat-transfer experiments in a vertical tube. Technical Report CONF-830301-16, EG and G Idaho, Inc., Idaho Falls (USA); Lehigh Univ., Bethlehem, PA (USA). Inst. of Thermo-Fluid Engineering and Science; Yankee Atomic Electric Co., Framingham, MA (USA), 1983.

RC Gottula, KG Condie, RK Sundaram, S Neti, JC Chen, and RA Nelson. Forced convective, nonequilibrium, post-chf heat transfer experiment data and correlation comparison. Technical Report NUREG/CR-3193, NASA, United States, 1985.

DC Groeneveld. *The thermal behaviour of a heated surface at and beyond dryout.* PhD thesis, University of Western Ontario, 1972.

DC Groeneveld. Post-dryout heat transfer at reactor operating conditions. Technical Report AECL-4513, Atomic Energy of Canada Ltd., 1973.

DC Groeneveld. Post-dryout heat transfer: physical mechanisms and a survey of prediction methods. *Nuclear Engineering and Design*, 32(3):283–294, 1975.

DC Groeneveld and GGJ Delorme. Prediction of thermal non-equilibrium in the post-dryout regime. *Nuclear Engineering and Design*, 36(1):17–26, 1976.

DC Groeneveld and EO Moeck. An investigation of heat transfer in the liquid deficient regime. Technical Report AECL-3281(Rev.), Atomic Energy of Canada Ltd., Chalk River (Ontario). Chalk River Nuclear Labs, 1969.

DC Groeneveld, S Doeffler, RM Tain, N Hammouda, and SC Cheng. Fluid-to-fluid modelling of the critical heat flux and post-dryout heat transfer. In *Proceedings of the Experimental Heat Transfer, Fluid Mechanics and Thermodynamics*, pages 859–866, 1997.

DC Groeneveld, LKH Leung, YJ Guo, SC Cheng, et al. A look-up table for fully developed film-boiling heat transfer. *Nuclear Engineering and Design*, 225(1):83–97, 2003.

Y Guo and LKH Leung. Developing film boiling heat transfer in tubes. In *The 11th International Topic Meeting on Nuclear Thermal-Hydraulics (NURETH11), Avignon, France*, 2005.

Y Guo and K Mishima. A non-equilibrium mechanistic heat transfer model for post-dryout dispersed flow regime. *Experimental thermal and fluid science*, 26(6-7):861–869, 2002.

G Hadaller and S Banerjee. Heat transfer to superheated steam in round tubes. Technical Report WDI-147, AECL, 1969.

Y Hagiwara, K Suzuki, and T Sato. An experimental investigation on liquid droplets diffusion in annular-mist flow. In *Multiphase Transport: Fundamentals, Reactor Safety, Applications*, pages 111–131, 1980.

N Hammouda, DC Groeneveld, and SC Cheng. An experimental study of subcooled film boiling of refrigerants in vertical up-flow. *International journal of heat and mass transfer*, 39(18):3799–3812, 1996.

JB Heineman. An experimental investigation of heat transfer to superheated steam in round and rectangular channels. Technical Report ANL-6213, Argonne National Lab, 1960.

G Hetsroni. Particles-turbulence interaction. *International Journal of Multiphase Flow*, 15(5):735–746, 1989.

EF Hicken. Important thermohydraulic aspects during refilling and reflooding of an uncovered lwr core. In *Safety of Thermal Water Reactors*, pages 23–36. Springer, 1985.

WS Hill and WM Rohsenow. Dryout droplet distribution and dispersed flow film boiling. Technical Report 85694-105, Cambridge, Mass.: Heat Transfer Laboratory, Dept. of Mechanical Engineering, Massachusetts Institute of Technology, 1982.

GA Hughmark. Mass and heat transfer from rigid spheres. *AIChE Journal*, 13(6):1219–1221, 1967.

LM Hull. *Thermal boundary layer development in dispersed flow film boiling.* PhD thesis, Massachusetts Institute of Technology, 1982.

SJ Hynek. *Forced-convection, dispersed-flow film boiling.* PhD thesis, Massachusetts Institute of Technology, 1969.

HY Jeong and HC No. Modelling for post-dryout heat transfer and droplet sizes at low pressure and low flow conditions. *International communications in heat and mass transfer*, 23(6):767–778, 1996.

OC Jones. *Nuclear reactor safety heat transfer.* Hemisphere Publishing Corporation, Washington, DC, 1981.

OC Jones and N Zuber. Post-chf heat transfer: a non-equilibrium, relaxation model. Technical Report CONF-770802-6, Brookhaven National Lab., 1977.

I Kataoka, M Ishii, and K Mishima. Generation and size distribution of droplet in annular two-phase flow. *Journal of Fluids Engineering*, 105(2):230–238, 1983.

M Kawaji. *Transient non-equilibrium two-phase flow: reflooding of a vertical flow channel.* PhD thesis, University of California, Berkeley, 1984.

RKF Keeys, JC Ralph, and DN Roberts. Post-burnout heat transfer in high pressure steam–water mixtures in a tube with cosine heat flux distribution. In *Proceedings of the International Symposium on Two-Phase Systems*, pages 99–118. Elsevier, 1972.

M Keizo, K Isao, and M Kaichiro. Post-dryout heat transfer analysis model with droplet lagrangian simulation. In *13th international conference on nuclear engineering*, Beijing (China), 2005.

M Keizo, K Isao, and M Kaichiro. Post-dryout heat transfer analysis model with droplet lagrangian simulation. *JSME International Journal Series B Fluids and Thermal Engineering*, 49(2):377–383, 2006.

GE Kendall and WM Rohsenow. Heat transfer to impacting drops and post critical heat flux dispersed flow. Technical Report MIT-56987-100, Cambridge, Mass.: Heat Transfer Laboratory, Dept. of Mechanical Engineering., 1978.

L Köckert, F Feuerstein, DL Yu, D Klingel, and X Cheng. Experimental study of post-dryout heat transfer and rewetting in a r- 134a cooled vertical tube at comparable water cooled reactor pressure conditions. In *The 12th International Topical Meeting on Reactor Thermal-Hydraulics, Operation, and Safety (NUTHOS-12)*, Qingdao (China), 2018.

W Köhler and D Hein. Influence of the wetting state of a heated surface on heat transfer and pressure loss in an evaporator tube. Technical Report NUREG/IA-0003, Nuclear Regulatory Commission, Washington, DC (USA). Office of Nuclear Regulatory Research; Kraftwerk Union AG, Erlangen (Germany, FR), 1986.

H Kumamaru, Y Koizumi, and K Tasaka. Investigation of pre-and post-dryout heat transfer of steam-water two-phase flow in a rod bundle. *Nuclear Engineering and Design*, 102(1):71–84, 1987.

HL Langhaar. *Dimensional analysis and theory of models.* Wiley, New York, 1951.

WF Laverty and WM Rohsenow. Film boiling of saturated liquid flowing upward through a heated tube: high vapor quality range. Technical Report 9857-32, Cambridge, Mass.: MIT Dept. of Mechanical Engineering, 1964.

K Lee and DJ Ryley. The evaporation of water droplets in superheated steam. *Journal of Heat Transfer*, 90(4):445–451, 1968.

R Lee and K Almenas. Droplet deposition above a quench front during reflood. *Trans. Am. Nucl. Soc.*, 43(CONF-821103), 1982.

SK Lee and SH Chang. Experimental study of post-dryout with r-134a upward flow in smooth tube and rifled tubes. *International Journal of Heat and Mass Transfer*, 51 (11-12):3153–3163, 2008.

D Legendre and J Magnaudet. The lift force on a spherical bubble in a viscous linear shear flow. *Journal of Fluid Mechanics*, 368:81–126, 1998.

LKH Leung, N Hammouda, and DC Groeneveld. Development of a look-up table for film-boiling heat transfer covering wide range of flow conditions. In *International conference on simulation methods in nuclear engineering*, Montreal, PQ (Canada), 1996.

LKH Leung, N Hammouda, and DC Groeneveld. A look-up table for film-boiling heat-transfer coefficients in tubes with vertical upward flow. In *Eighth international topical meeting on nuclear reactor thermal-hydraulics*, Kyoto (Japan), 1997.

HP Li and H Anglart. Cfd model of diabatic annular two-phase flow using the eulerian–lagrangian approach. *Annals of Nuclear Energy*, 77:415–424, 2015.

HP Li and H Anglart. Prediction of dryout and post-dryout heat transfer using a two-phase cfd model. *International Journal of Heat and Mass Transfer*, 99:839–850, 2016.

KJ Liesch, G Raemhild, and K Hofmann. Zur Bestimmung des Wärmüberganges und der kritischen Heizflächenbelastung im Hinblick auf besondere Verhältnisse in den Kühlkanälen eines DWR bei schweren Kühlmittelverlustunfällen. Technical Report MRR 150, Laboratorium für Reaktorregelung und Anlagensicherung, 1975.

BYH Liu and TA Ilori. Aerosol deposition in turbulent pipe flow. *Environmental Science and Technology*, 8(4):351–356, 1974.

MJ Loftus, LE Hochreiter, CE Conway, CE Dodge, A Tong, ER Rosal, MM Valkovic, and S Wong. Pwr flecht seaset unblocked bundle, forced and gravity reflood task data report. volume 1. Technical Report NUREG/CR-2256, Westinghouse Electric Corp., Pittsburgh, PA (USA). Nuclear Energy Systems Div., 1981.

WH McAdams. *Heat Transmission.* McGraw-Hill Book Company, New York, 1954.

JB McLaughlin. The lift on a small sphere in wall-bounded linear shear flows. *Journal of Fluid Mechanics*, 246:249–265, 1993.

N Meamer. On fluid-to-fluid modeling of film boiling heat transfer using dimensional analysis. *International Journal of multiphase flow*, 37(2):229–234, 2011.

MJ Meholic. *The development of a non-equilibrium dispersed flow film boiling heat transfer modeling package.* PhD thesis, The Pennsylvania State University, 2011.

RA Moose and EN Ganić. On the calculation of wall temperatures in the post dryout heat transfer region. *International Journal of Multiphase Flow*, 8(5):525–542, 1982.

RE Mueller. Film boiling heat transfer measurements in a tubular test section. Technical Report EURAEC-1871, General Electric Co., San Jose, Calif. Atomic Power Equipment Dept., 1967.

M Nemitallah and N Meamer. Fluid to fluid modeling for post dry out using dimensional analysis and energy scaling. In *Applied Mechanics and Materials*, volume 302, pages 42–48. Trans Tech Publ, 2013.

NH Nguyen and SK Moon. An improved heat transfer correlation for developing post-dryout region in vertical tubes. *Nuclear Engineering and Technology*, 47(4):407–415, 2015.

S Nijhawan, JC Chen, RK Sundaram, and EJ London. Measurement of vapor superheat in post-critical-heat-flux boiling. *Journal of Heat Transfer*, 102(3):465–470, 1980.

K Nishikawa, S Yoshida, H Mori, and H Takamatsu. An experiment on the heat transfer characteristics in the post-burnout region at high subcritical pressures. *Nuclear Engineering and Design*, 74(2):233–239, 1983.

K Nishikawa, S Yoshida, H Mori, and H Takamatsu. Post-dryout heat transfer to freon in a vertical tube at high subcritical pressures. *International journal of heat and mass transfer*, 29(8):1245–1251, 1986.

EE Paladino and CR Maliska. Virtual mass in accelerated bubbly flows. In *Proceedings of 4th European Themal Sciences, 29th-31st March, National Exhibition Centre, Birmingham, UK*, 2004.

WE Ranz, WR Marshall, et al. Evaporation from drops. *Chem. Eng. Prog*, 48(3):141–146, 1952.

WM Rohsenow. Post dryout heat transfer prediction method. *International communications in heat and mass transfer*, 15(4):559–569, 1988.

P Saha. A nonequilibrium heat transfer model for dispersed droplet post-dryout regime. *International Journal of Heat and Mass Transfer*, 23(4):483–492, 1980.

MM Shah and MA Siddiqui. A general correlation for heat transfer during dispersed-flow film boiling in tubes. *Heat transfer engineering*, 21(4):18–32, 2000.

JX Shi, BZ Sun, GL Zhang, FY Song, and LB Yang. Prediction of dryout and post-dryout wall temperature at different operating parameters for once-through steam generators. *International Journal of Heat and Mass Transfer*, 103:66–76, 2016.

A Sozer, TM Anklam, and HL Dodds. Convection-radiation heat transfer to steam in rod bundle geometry. *Nuclear technology*, 67(3):452–462, 1984.

KI Sugioka and S Komori. Drag and lift forces acting on a spherical water droplet in homogeneous linear shear air flow. *Journal of Fluid Mechanics*, 570:155–175, 2007.

KH Sun, JM Gonzalez-Santalo, and CL Tien. Calculations of combined radiation and convection heat transfer in rod bundles under emergency cooling conditions. *Journal of Heat Transfer*, 98(3):414–420, 1976.

WX Tian, SZ Qiu, and DN Jia. Investigations on post-dryout heat transfer in bilaterally heated annular channels. *Annals of Nuclear Energy*, 33(2):189–197, 2006.

S Torfeh and R Kouhikamali. Numerical investigation of mist flow regime in a vertical tube. *International Journal of Thermal Sciences*, 95:1–8, 2015.

C Unal, K Tuzla, O Badr, S Neti, and JC Chen. Parametric trends for post-chf heat transfer in rod bundles. *Journal of heat transfer*, 110(3):721–727, 1988.

AF Varone. *The influence of the dispersed phase on the convective heat transfer in dispersed flow film boiling*. PhD thesis, Massachusetts Institute of Technology, 1990.

AF Varone and WM Rohsenow. Post dryout heat transfer prediction. *Nuclear Engineering and Design*, 95:315–327, 1986.

I Vojtek. Auswertung der 25-Stabbündel-Versuche mit dem Rechenprogramm BRUDIVA. Technical Report GRS-A-208, Gesellschaft für Anlagen- und Reaktorsicherheit (GRS), 1978.

SW Webb and JC Chen. A numerical model for turbulent non-equilibrium dispersed flow heat transfer. *International Journal of Heat and Mass Transfer*, 25(3):325–335, 1982.

J Yang, DC Groeneveld, LKH Leung, SC Cheng, and MA Nakla. An experimental and analytical study of the effect of axial power profile on chf. *Nuclear engineering and design*, 236(13):1384–1395, 2006.

GL Yoder and WM Rohsenow. A solution for dispersed flow heat transfer using equilibrium fluid conditions. *Journal of Heat Transfer*, 105(1):10–17, 1983.

WM Yoder, GL; Rohsenow. Dispersed flow film boiling. Technical Report 85694-103, Massachusetts Institute of Technology. Heat Transfer Laboratory., 1980.

MC Yuen and LW Chen. Heat-transfer measurements of evaporating liquid droplets. *International Journal of Heat and Mass Transfer*, 21(5):537–542, 1978.

List of Publications

During Ph.D.

Yu, Dali, & Cheng, X. (2018). Verification of Proposed Post-Dryout Heat Transfer Model. 49th Annual Meeting on Nuclear Technology (AMNT 2018), Berlin, May 29-30.

Yu, Dali, Feuerstein, F., Köckert, L., & Cheng, X. (2018). Analysis and modeling of post-dryout heat transfer in upward vertical flow. Annals of Nuclear Energy, 115, 186-194.

Cheng, X., Feuerstein, F., Klingel, D., & **Yu, Dali** (2018). Mechanistic prediction of post dryout heat transfer and rewetting. Kerntechnik, 83(3), 203-207.